

8-2017

# Metal Oxide Semiconductor / Graphene Heterojunction Based Sensors

Md Maksudul Hossain  
*Clemson University*

Follow this and additional works at: [https://tigerprints.clemson.edu/all\\_theses](https://tigerprints.clemson.edu/all_theses)

---

## Recommended Citation

Hossain, Md Maksudul, "Metal Oxide Semiconductor / Graphene Heterojunction Based Sensors" (2017). *All Theses*. 2754.  
[https://tigerprints.clemson.edu/all\\_theses/2754](https://tigerprints.clemson.edu/all_theses/2754)

This Thesis is brought to you for free and open access by the Theses at TigerPrints. It has been accepted for inclusion in All Theses by an authorized administrator of TigerPrints. For more information, please contact [kokeefe@clemson.edu](mailto:kokeefe@clemson.edu).

METAL OXIDE SEMICONDUCTOR / GRAPHENE HETEROJUNCTION BASED  
SENSORS

---

A Thesis  
Presented to  
the Graduate School of  
Clemson University

---

In Partial Fulfillment  
of the Requirements for the Degree  
Master of Science  
Electrical Engineering

---

by  
Md Maksudul Hossain  
August 2017

---

Accepted by:  
Dr. Goutam Koley, Committee Chair  
Dr. William Rod Harrell  
Dr. Rajendra Singh

## ABSTRACT

Graphene, a two-dimensional material with very high carrier mobility, has drawn much attention for sensing chemical species. It is atomically thin hexagonal arrangement of carbon where each atom is attached to 3 neighboring carbon atoms. The presence of  $\pi^*$  and  $\pi$  bonds can be attributed for it many remarkable properties. Some of these properties are high mobility, modulation of carrier concentration and Fermi level by electrical, optical, and chemical means, low  $1/f$  and thermal noise, and very high surface to volume ratio to name a few making graphene a potential candidate for sensing material. However, to utilize these amazing properties for practical applications a reliable synthesis of high quality, large area graphene is needed. Chemical Vapor Deposition (CVD) based synthesis offers reliable, scalable, and inexpensive method to make low defect, continuous, large area, and thinner graphene with the ability to transfer graphene on any desirable substrate. In this work, high quality single layer graphene has been synthesized by CVD for sensing applications. The growth process was optimized to produce good quality monolayer graphene as characterized by Raman spectroscopy.  $\text{CH}_4$  has been used as precursor gas for the growth at  $1035^\circ\text{C}$ . Since graphene work function can be varied electrically or chemically, the Schottky Barrier Height (SBH) at Graphene/Semiconductor interface also varies accordingly affecting the carrier transport across the barrier. In this work, we used transition metal oxide (e.g.  $\text{WO}_3$ ,  $\text{In}_2\text{O}_3$ , and  $\text{ZnO}$ ) along with graphene to study the behavior of graphene/metal oxide heterojunction in sensing  $\text{NO}_2$  and  $\text{NH}_3$  because both of these metal oxides and graphene are

individually very sensitive to  $\text{NO}_2$  and  $\text{NH}_3$ . Our motivation was to see if the sensitivity and response time improves in case we use them together.

## ACKNOWLEDGEMENTS

I would first like to sincerely thank Dr. Goutam Koley, who gave me the opportunity to pursue my Masters of Science under his guidance. I feel very auspicious to work for a professor who cares so much for his students. His motivational techniques and knowledge of a wide variety of topics have allowed me to branch out of my traditional electrical engineering background and involve more into multidisciplinary researches. His passionate researches have sparked a new interest in learning, which I plan to continue as I pursue my PhD. I am also indebted to my thesis committee members Dr. William Rod Harrell and Dr. Rajendra Singh. Their in-depth teaching of semiconductor device and IC fabrication helped me a lot to delve into my research topic more. I would also like to thank Dr. Terry Tritt for his elaborate teaching of Solid State Devices Physics which I found of great help in understanding temperature effects on transport mechanism. I was fortunate enough to have worked with some excellent co-workers throughout my time at Clemson University. Ifat Jahangir, who showed me the ins and outs of the VOC sensors, was an excellent guide all through. John Hardaway and Jonathan Barreto, who worked with me for the bulk of the summer of 2016, were vital assets for automation of the CVD growth.

## TABLE OF CONTENTS

	Page
ABSTRACT.....	ii
ACKNOWLEDGEMENTS .....	iv
TABLE OF CONTENTS.....	v
LIST OF TABLES .....	vii
LIST OF FIGURES .....	ix
CHAPTER	
I. INTRODUCTION.....	1
1.1 Overview of graphene properties.....	1
1.2 Graphene application and trends.....	12
1.3 Overview of metal oxide semiconductors as sensors .....	13
1.4 Objective .....	14
1.5 Layout of the Thesis.....	15
II. LITERATURE REVIEW AND BACKGROUND .....	17
2.1 Graphene growth.....	17
2.2 Raman spectroscopy .....	35
III. MATERIALS AND EXPERIMENTAL PROCEDURES .....	42
3.1 CVD Furnace Components .....	42
3.2 CVD growth of graphene .....	43
3.3 Preparation of transition metal oxide film .....	53
3.4 Graphene characterization .....	53

## Table of Contents (Continued)

	Page
3.5 Sensing.....	55
IV. RESULTS AND DISCUSSION .....	58
4.1 Characterization of as-grown graphene .....	58
4.2 Graphene Semiconductor Schottky Junctions .....	68
4.3 Determination of Electrical Parameters in In <sub>2</sub> O <sub>3</sub> /Graphene heterojunction .....	77
4.4 Variation of n, $\phi_B$ with Temperature.....	87
4.5 Determination of SBH in WO <sub>3</sub> /Graphene heterojunction: .....	88
4.6 Sensing response of In <sub>2</sub> O <sub>3</sub> and WO <sub>3</sub> to NO <sub>2</sub> and NH <sub>3</sub> with and without Graphene.....	90
V. CONCLUSIONS .....	107
4.1 Summary .....	107
4.2 Challenges and recommendation for future research.....	107
APPENDICES .....	109
A. MATLAB Codes .....	110
B. Different design schemes for the device .....	118
REFERENCES .....	119

## LIST OF TABLES

Table	Page
2.1 Advantages and challenges of CVD grown graphene .....	31
2.2 Comparison of all four graphene growing techniques .....	34
3.1 Basic steps of cleaning copper substrate explained .....	44
4.1 Hall measurement of graphene transferred on SiO <sub>2</sub> /Si .....	61
4.2 Statistical data of hall mobility of different samples at different locations.....	62
4.3 Ideality factor, reverse saturation current and SBH.....	81
4.4 Ideality factor, reverse saturation current and SBH from Arrhenius plot.....	82
4.5 Comparisons of different methods .....	84
4.6 Parameter extraction from LSE method .....	85
4.7 Comparison of the electrical parameters for all five methods .....	87
4.8 Parameter extraction for graphene/WO <sub>3</sub> Schottky junction at the temperature of 300K.....	90
4.9 Comparison of Thermionic emission, Cheung's and Least Square Error (LSE) method.....	90
4.10 Time constant variation with annealing temperature for WO <sub>3</sub> .....	98
4.11 Comparison of different metal oxide properties .....	101
4.12 NO <sub>2</sub> Response time with and without Graphene for different samples (WO <sub>3</sub> , In <sub>2</sub> O <sub>3</sub> , ZnO) .....	102
4.13 Sensitivity comparison with and without graphene .....	105



## List of Tables (Continued)

Table	Page
4.14 $\text{NH}_3$ Response time with and without Graphene with different samples ( $\text{WO}_3$ , $\text{In}_2\text{O}_3$ ).....	105
4.15    Sensitivity comparison with and without graphene .....	106

## LIST OF FIGURES

Figure	Page
1.1 Honeycomb structure of graphene .....	2
1.2 Honeycomb lattice, resulting from interpenetrating triangular lattices. The nearest distance is $a=142$ pm and the lattice constant is $\sqrt{3}a=246$ pm .....	3
1.3 Hexagonal Brillouin zone of honeycomb lattice, resulting from interpenetrating triangular lattices. Reciprocal lattice vectors are $b_1, b_2$ and the essential Dirac points are K, K' .....	4
1.4 Energy bands of graphene adapted from as given by Wallace (1947). The Dirac-like features are the linear energy dispersions, present near the neutral K, K'. One is expanded into the right panel of the figure. (Wolfram mathematica) .....	5
1.5 (a) Band structure of pristine graphene (b) p-type graphene (c) n-type graphene .....	7
1.6 Transfer curve of Graphene FET .....	8
1.7 Overview of applications of graphene. ....	13
2.1 Different synthesis techniques of Graphene .....	17
2.2 Scotch tape method .....	18
2.3 Micromechanically exfoliated graphene. Optical images of (a) thin graphite and (b) few-layer graphene (FLG) and single-layer graphene (lighter purple contrast) on a 300 nm SiO <sub>2</sub> layer. Yellow-like color indicates thicker samples (100s of nm) while bluish and lighter contrast samples .....	19
2.4 Liquid-phase exfoliation process of graphite in the absence (top-right) and presence (bottom-right) of surfactant molecules .....	20
2.5 Formation process of epitaxial graphene via sublimation of Si from the SiC surface. ....	21

## List of Figures (Continued)

Figure		Page
2.6	Proposed reactions during the isocyanate treatment of GO where organic isocyanides react with the hydroxyl (left oval) of graphene oxide sheets to form carbamate and amide functionalities.....	24
2.7	Graphene oxide and reduced graphene oxide preparation .....	25
2.8	Solubility curve for Carbon in a transition metal.....	26
2.9	Temperature vs. time diagram of APCVD showing different steps (1) annealing the catalyst metal foil, (2) exposure to CH <sub>4</sub> and (3) Cooling .....	28
2.10	Optical images of (a) Ni foil annealed (b) Graphene transferred on SiO <sub>2</sub> /Si (c) Dark features indicates presence of Graphite and FLG .....	28
2.11	Stages involved in CVD synthesis of graphene .....	30
2.12	Raman spectra of SLG with 532 nm Laser excitation .....	36
2.13	Optical image of Graphene/SiO <sub>2</sub> .....	37
2.14	(Top) Graphical representations of examples of phonon scattering processes responsible for the significant graphene Raman peaks. The D (intervalley phonon and defect scattering) and D' (intravalley phonon and defect scattering) peaks appear in disordered graphene. The 2D peak involves double phonon scattering. ....	41
3.1	Substrate (Cu foil) Cleaning Steps.....	44
3.2	Steps of CVD graphene growth on copper substrate .....	46
3.3	Temperature profile for CVD growth of graphene .....	47
3.4	Nucleation and subsequent phases of graphene growth on copper.....	47
3.5	Quartz plates on which the Cu/Ni foil is kept to allow graphene to grow .....	49

## List of Figures (Continued)

Figure	Page
3.6 (a) CVD system (b) Mass Flow Controller for different gas (c) Pump with inlet and outlet filters.....	50
3.7 Graphene transfer steps on SiO <sub>2</sub> /Si Substrate.....	52
3.8 (a) Dimension 3100 Atomic force microscopy, (b) Scanning going on .....	54
3.9 (a) Hall measurement Unit (b) PCB for sample mounting (c) Permanent Magnet (0.55 T) .....	55
3.10 (a) Agilent 34970A Data Acquisition (b) B2902A Precision Source/Measure Unit (SMU) .....	56
3.11 (a) MKS Instruments 1179A Analog MFC (b) GE-50A series web controlled Digital MFC .....	56
3.12 Experimental set up for gas sensing.....	57
4.1 Optical images of (a) Pure copper foil (b) Annealed copper at 1000 <sup>0</sup> C (c) Graphene on Copper, dashed line shows the graphene boundary.....	59
4.2 Steps growing the transferring of as grown graphene on copper to SiO <sub>2</sub> /Si substrate .....	60
4.3 (a,b) Optical images of Graphene transferred on SiO <sub>2</sub> /Si Hall mobility, the dashed line shows the boundary of graphene. ....	60
4.4 Hall mobility of different location of same sample (a) sample # 190 (b) sample # 191.....	62
4.5 Hall data from different growth .....	63
4.6 (top left) Height profile (top right) Phase imaging (middle) Cross-section along the line indicated of graphene transferred on SiO <sub>2</sub> /Si (bottom) 3D topography of graphene on SiO <sub>2</sub> /Si showing possible acetone residue and wrinkles.....	65

## List of Figures (Continued)

Figure	Page
4.7 Raman spectra of (a) graphene transferred on SiO <sub>2</sub> /Si substrate (b) WO <sub>3</sub> on a Al <sub>2</sub> O <sub>3</sub> ceramic substrate.....	66
4.8 Raman Spectroscopy of different samples.....	67
4.9 G-band position indicating number of layers.....	68
4.10 Metal Semiconductor Schottky junction formation (a,b) energy band diagram before contact (c) schematic showing depletion region after charge transferring taking place (d,e) Schottky junction formation in n and p-type semiconductor.....	70
4.11 Principal transport processes across an M/S Schottky junction: TE = thermionic emission, TFE = thermionic field emission, FE = field emission .....	73
4.12 (a) Device structure of In <sub>2</sub> O <sub>3</sub> /Graphene Heterojunction diode (b) I-V characteristics of Graphene/In <sub>2</sub> O <sub>3</sub> Schottky junction at the temperature of 301K (Inset shows the optical image of fabricated device).....	78
4.13 Schematic of Schottky formation mechanism in In <sub>2</sub> O <sub>3</sub> (and WO <sub>3</sub> )/Graphene Junction .....	79
4.14 (a) I-V characteristics (semi log scale) (b) lnI-V plot (c) Linear Curve Fit of Graphene/In <sub>2</sub> O <sub>3</sub> Schottky junction at the temperature of 301K .....	80
4.15 log(I <sub>0</sub> /T <sup>2</sup> ) vs 1000/T plot to extract Richardson constant .....	81
4.16 (a) dV/d(lnI) vs. I and (b) Cheung's functions, H(I) vs. I plot of our In <sub>2</sub> O <sub>3</sub> /Graphene Schottky diode at the temperature of 301 K.....	84
4.17 The Arrhenius plots for the barrier height extractions using TFE method (a) The barrier height of graphene/In <sub>2</sub> O <sub>3</sub> junction is 847 meV. (b) The average barrier height of graphene/In <sub>2</sub> O <sub>3</sub> junction is 848 meV by sweeping the applied bias.....	86

## List of Figures (Continued)

Figure	Page
4.18 (a) Variation of $n$ , $\phi_B$ with Temperature (b) Linear fit for temperature coefficient .....	88
4.19 (a) Device structure of $\text{WO}_3$ /Graphene Schottky diode (b) I-V characteristics of Graphene/ $\text{WO}_3$ Schottky junction at the temperature of 301K .....	88
4.20 (a) I-V (semi log) characteristics (b) $\ln I$ -V plot (c) Linear curve fit of the Graphene/ $\text{WO}_3$ Schottky junction at the temperature of 301K .....	89
4.21 Carrier transport through the graphene-semiconductor Schottky barrier .....	91
4.22 Sensing mechanisms in transition metal oxide .....	93
4.23 (a) transient response of $\text{WO}_3$ annealed at (a) 350°C, (b) 400°C, (c) 450°C and (d) 550°C to $\text{NO}_2$ (5 ppm) .....	95
4.24 (Top) MATLAB fitting for the sensing response at 350°C annealing temperature, fitted time constant (bottom left) rise (bottom right) fall varies with annealing temperature due to re-crystallization .....	97
4.25 Annealing temperature dependence of (a) Hall mobility (b) Carrier concentration (c) Resistivity and (d) Response and recovery time .....	99
4.26 Transient response of different metal oxide semiconductor without graphene (a) ZnO (b) $\text{WO}_3$ (c) $\text{In}_2\text{O}_3$ to 5ppm, 150 sccm of $\text{NO}_2$ .....	100
4.27 Sensing response of different metal oxide semiconductor with graphene (a) ZnO (b) $\text{WO}_3$ (c) $\text{In}_2\text{O}_3$ in exposure of 5ppm, 150 sccm of $\text{NO}_2$ .....	100
4.28 Sensitivity of $\text{WO}_3$ (a) without graphene (b) with graphene to $\text{NO}_2$ exposure (150sccm, 5 ppm) .....	102

## List of Figures (Continued)

Figure		Page
4.29	The response for graphene on SiO <sub>2</sub> /Si for NH <sub>3</sub> indicating p-type graphene .....	103
4.30	Sensing response of different metal oxide semiconductor with graphene (a) ZnO (b) WO <sub>3</sub> (c) In <sub>2</sub> O <sub>3</sub> in exposure of 5ppm 150 sccm NO <sub>2</sub> .....	104
4.31	Effect of operating temperature on NO <sub>2</sub> response of ZnO sensors at 5 ppm of NO <sub>2</sub> gas. ....	106

## CHAPTER I

### INTRODUCTION

#### 1.1 Overview of Graphene properties

Graphene is a one atom thick  $sp^2$  bonded carbon with a honeycomb lattice structure (Novoselov and Geim, 2007). The single layers can be separated from graphite, and grown by Chemical Vapor Deposition (CVD) method. It's highly elastic. It has also high electrical and thermal conductivity. Graphene is a semimetal with zero band gaps. The Fermi level is at the touching point of valence and conduction band in pristine graphene. However, the Fermi level can be tuned to make it n-type or p-type, by chemical doping, or by applying a bias. The touching point is known as Dirac point and the dispersion relationship near this point is linear unlike parabolic in conventional semiconductor (Soldano et al., 2010). As the atomic positions are symmetric, the energy surface is cone shaped rather than parabolic which is the main reason of the extraordinary electron properties. Absence of direct backscattering of electrons due to its lattice symmetry enhances the electrical mobility and conductivity (Novoselov et al., 2005). The main uniqueness of graphene is that it is fully functional and continuous resulting in exceedingly high electrical conductivity which is vital in application. The tunability of the Fermi level can be utilized in device applications (Wehling et al., 2008). Graphene is a conductor based on strong  $sp^2$  trigonal bonds between carbon atoms. The four valence electrons of carbon are fully engaged in graphene structure: 3 of these covalently bond the triangular lattice, the remaining one is in a  $2p_z$  state, makes the conduction possible.



The full covalent bonding leaves graphene as chemically inert and very strong and the single free  $p_z$  electron gives enormously high electrical conductivity.

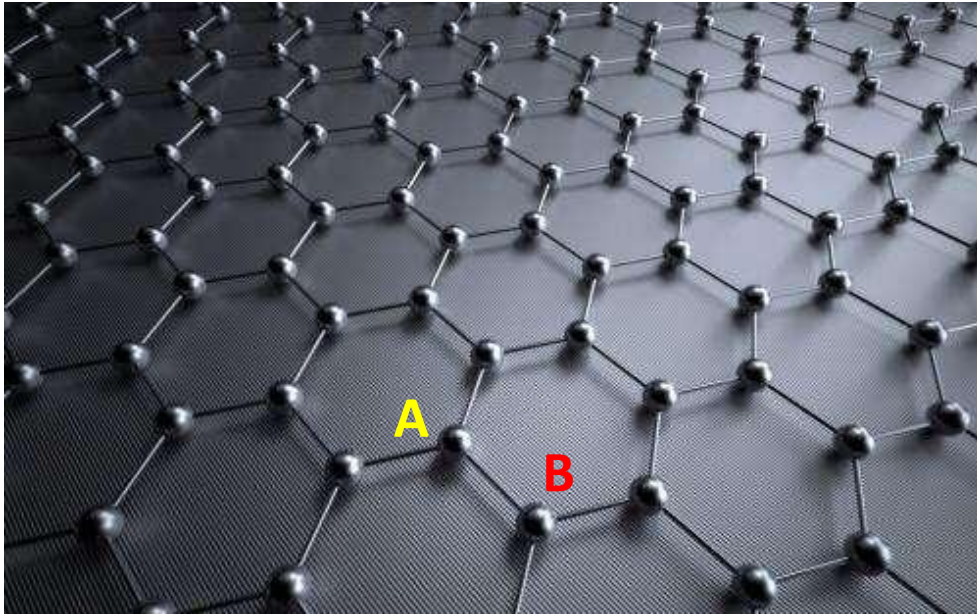


Figure 1.1. Honeycomb structure of graphene

Another property of graphene is its vast surface area,  $2,600 \text{ m}^2/\text{g}$ . The surface to volume ratio is maximal because graphene is one atom thick and so graphene is all surface. So, it is true that graphene is inert, however if one looks more closely, physisorbed and chemisorbed atoms and molecules are common and change the electrical conductivity of graphene. Molecules can also increase the conductivity by adding carriers to graphene, but the mobility is always reduced. The dangling bonds and surface sensitivity of graphene is the basis for its use as a sensor (Schedin et al., 2007).

### 1.1.1 Basic Lattice and Electronic Structure

The lattice is shown in Fig. 1.1, although A and B indicate identical carbon atoms but located on the two interpenetrating triangular lattices that make up the honeycomb lattice.

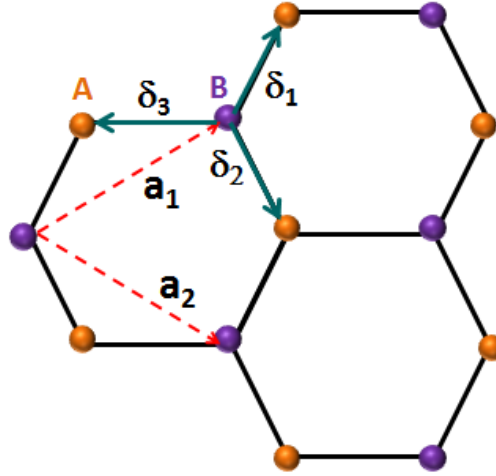


Figure 1.2. Honeycomb lattice, resulting from interpenetrating triangular lattices. The nearest distance is  $a=142$  pm and the lattice constant is  $\sqrt{3}a=246$  pm

In this figure,  $\vec{a}_1$  and  $\vec{a}_2$  are the basis vectors that generate the lattice, while  $\vec{\delta}_1, \vec{\delta}_2, \vec{\delta}_3$  are the nearest neighbor translations. In more detail, we have basis vectors  $\vec{a}_1 = (\sqrt{3}, 0)$ ,  $\vec{a}_2 = (0, 1)$ , and the sub lattices are connected by  $\vec{\delta}_1 = (\frac{\sqrt{3}}{2}, \frac{1}{2})$ ,  $\vec{\delta}_2 = (-\frac{\sqrt{3}}{2}, \frac{1}{2})$ ,  $\vec{\delta}_3 = (-\sqrt{3}, 0)$ , in terms of the nearest neighbor distance,  $a = 142$  pm. The bonding in this structure is of the planar covalent  $sp^2$  type based on the  $n = 2$  electrons of the carbon atom (Soldano et al., 2010). An important feature of this structure is that the

nearest neighbor atoms are on different sub lattices, denoted with purple and orange color. The corresponding Brillouin zone is depicted in Fig. 1.3.

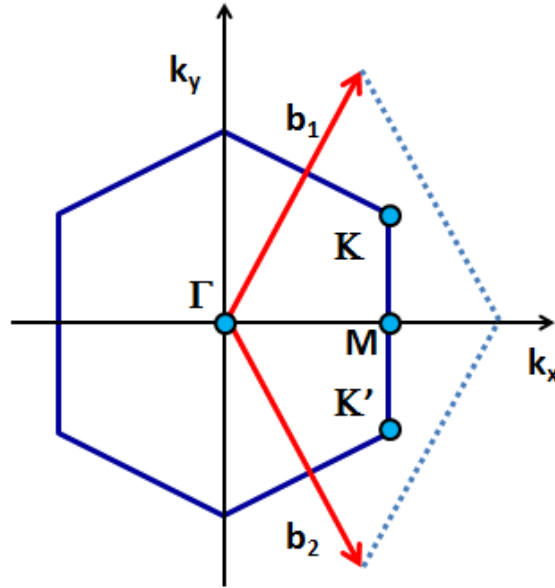


Figure 1.3. Hexagonal Brillouin zone of honeycomb lattice, resulting from interpenetrating triangular lattices. Reciprocal lattice vectors are  $b_1, b_2$  and the essential Dirac points are K, K'.

Viewing Fig. 1.2, with nearest-neighbor distance  $a = 142$  pm, the lattice constant is  $3^{1/2}a$ , and the zone boundary M (half the reciprocal lattice vectors  $b_1, b_2$ ), is  $2\pi/3a$ . The coordinates of the corner point K are  $(2\pi/3a, \pi/3\sqrt{3}a)$  so that the distance from the origin to point K is  $4\pi/(3\sqrt{3}a)$ . Since the conduction and valence bands touch at K, we have  $k_F = |K|$  and the Fermi wavelength  $k_F = 2\pi/k_F = 3\sqrt{3}a/2 = 369$  pm. The electron bands that arise in this lattice were first calculated by Wallace in 1947, who realized that the bands of the single plane that he calculated were a good approximation to the bands of graphite,

since the planes are so weakly coupled and so widely spaced, by 0.34 nm. A modern representation of that band structure is shown in Fig. 1.4. The upper and lower bands are derived from the  $2p_z$  orbital of carbon. The conical crossings at K and  $K_0$  (Wallace 1947) are the result of the two-sub lattice symmetry.

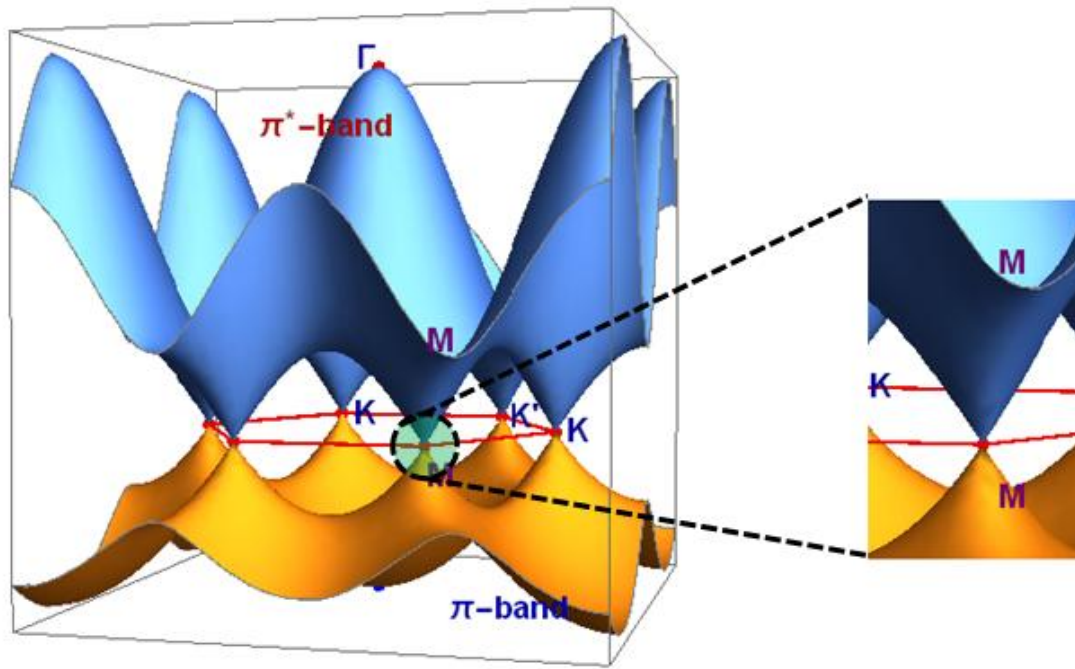


Figure 1.4. Energy bands of graphene adapted from as given by Wallace (1947). The Dirac-like features are the linear energy dispersions, present near the neutral K, K'. One is expanded into the right panel of the figure. (Wolfram mathematica)

This simple model allows for an analytical solution of the energy bands:

$$\text{---} \quad (1.1)$$

In pristine undoped graphene, the conduction and valence bands touch at the K and K' points. Expanding equation (1.1) near K (K') yields a linear dispersion:

$$E^{\pm}(k) = \pm \hbar v_F |k| \quad (1.2)$$

and  $v_F$  is the electronic group velocity given by:

$$v_F = \sqrt{3} \gamma_0 a / 2 \hbar \quad (1.3)$$

Equation (1.2) is a good approximation as long as the energy does not deviate too far from  $E_F$ , or conversely that the momentum does not deviate too far from the K (K') point. This condition is satisfied in most current graphene devices. Because of its linear bands, the effective mass of electrons and holes in graphene is defined as:

$$m^* = \frac{\hbar^2 k}{\frac{dE}{dk}} \bigg|_{E=E_F} \quad (1.4)$$

Instead of

$$m^* = \frac{\hbar^2 k}{\frac{d^2 E(k)}{dk^2}} \bigg|_{E=E_F} \quad (1.5)$$

## 1.1.2 Electronic Transport and Field Effect Behavior of Graphene

### 1.1.2.1 Ambipolar Field Effect in Graphene

Electric field applied normal to graphene plane can induce charge carriers, electrons or holes. The Fermi level ( $E_F$ ) can move up in conduction band inducing electrons, and can move down in valence band inducing holes depending upon the direction of the field. This results in ambipolar nature of graphene channel (Rumyantsev et al., 2010; Wu et al., 2008)

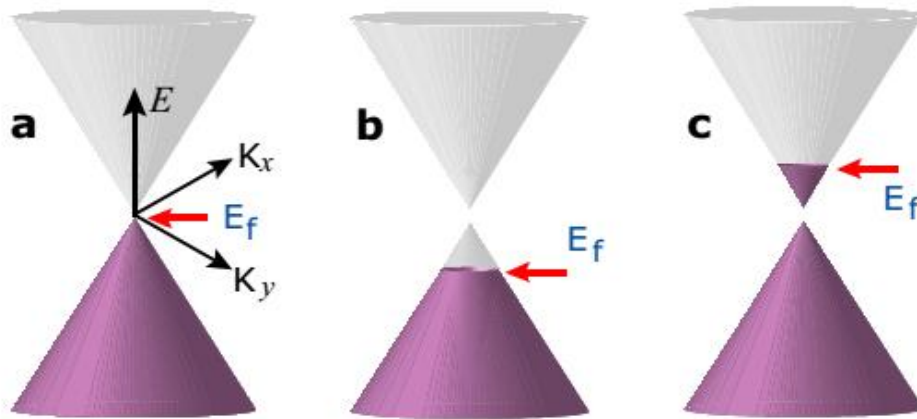


Figure 1.5. (a) Band structure of pristine graphene (b) p-type graphene (c) n-type graphene

However, these new electrons (or holes) can come from many sources: electrostatic tuning charged impurity atoms, adsorbents etc. This condition of excess carriers, which corresponds to the Fermi level being away from the Dirac point, is called

doping. Although we conventionally talk about doping as introduction of donor/acceptor atoms in semiconductors in graphene, however, doping is commonly referred to in a broader context (Wu et al., 2008). Apart from electrostatic tuning, doping normally refers to with some kind of disorder in the system. This disorder often is responsible for doping in the conventional sense, i.e. accepting or donating electrons. But in the case of electrostatic tuning the contacts facilitate the injection of electrons or holes in the graphene sheet. For example the back-gated graphene Field Effect Transistor in Fig. 1.6

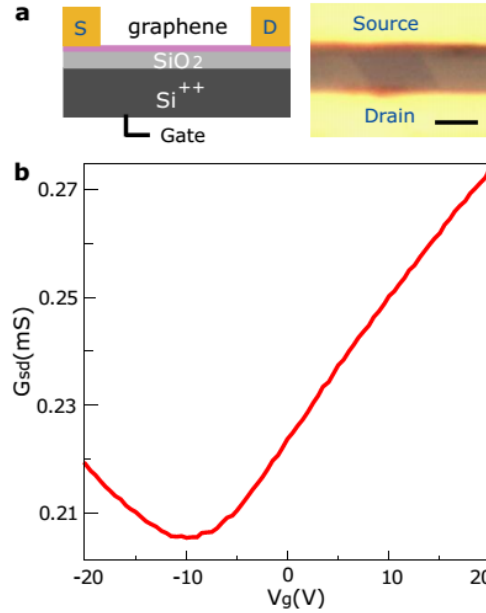


Figure 1.6. Transfer curve of Graphene FET

The drain voltage ( $V_d$ ) is typically in the tens of millivolts, which in turn gives a current of couple of microamperes during transport. Let's assume  $V_d=0$ , and the gate voltage,  $V_g$  is 10 V. Consequently, the contacts, which are connected to the voltage source, are negatively charged and the gate is positively charged, i.e. like a parallel plate

capacitor. Since graphene is conductive under all conditions (i.e. no band gap) it acts like a metal and it also gets negatively charged by accepting the excess electrons from the contacts, which in turn get replenished by the voltage source. Therefore, the contacts and graphene combined act as the negative plate of a parallel plate capacitor, with the gate acting as a positive plate. In absence of externally applied electric field the  $E_F$  and DOE should ideally be zero in graphene.

However in graphene channel there is always finite charge present due to either thermal generation or induction due to impurities at graphene and substrate interface even no electric field is applied. Therefore the threshold voltage beyond which graphene based FETs can turn on or off does not really exist. The minimum to maximum current ratio in graphene based FETs remains in the range to 5-10 and that's why they are unsuitable for switching application despite having high mobility values (Rumyantsev et al., 2010)

#### **1.1.2.1 Mobility**

The main scattering mechanism in graphene is Coulomb scattering, short-range scattering, phonon scattering by graphene phonons, substrate surface polar phonon scattering, midgap states and roughness mainly because of defects such as point defects, line defects, single and double vacancies and cracks in graphene (Hwang and Sarma, 2008). So the mobility is strongly dependent on the quality of graphene and corresponding substrates. For instance at room temperature surface polar phonons and



defects are two major scattering mechanism for graphene on SiO<sub>2</sub>, whereas at lower temperature phonons become important. The typical mobility values of good quality graphene on SiO<sub>2</sub> ranges from 10000 to 15000 cm<sup>2</sup>V<sup>-1</sup>s<sup>-1</sup>. If we could remove the substrates or use graphene free from trapped charges, it would show improved mobility. The reported mobility in suspended graphene has been as high as 200,000 cm<sup>2</sup>V<sup>-1</sup>s<sup>-1</sup> for charge density below 5×10<sup>9</sup>cm<sup>-2</sup> at a low temperature of 5K (Bolotin et al., 2008). At room temperature the supported graphene on SiO<sub>2</sub> will have an upper limit of 40000 cm<sup>2</sup>V<sup>-1</sup>s<sup>-1</sup> on mobility due to scattering by optical phonon of the substrate.

### **1.1.3 Mechanical Property**

One of graphene's amazing properties is its intrinsic strength. Graphene is the strongest material ever discovered because of the strength of its 142 pm-long carbon bonds, with an ultimate tensile strength of 130 GPa, compared to 0.4GPa for A36 structural steel (Bonaccorso et al., 2010). Graphene is not only very strong but also very light (0.77mg m<sup>-2</sup>). Graphene also contains highly elastic properties, being able to retain its initial state after strain being released. Atomic Force Microscopic (AFM) tests showed that graphene sheets (with thicknesses of between 2 and 8 nm) had spring constants in the region of 1-5 N/m and a Young's modulus of 0.5 TPa (Lee et al., 2012). Again, these excellent figures are based on theoretical prospects using graphene that is unflawed containing no imperfections. As production techniques are improving a lot, ultimately reducing costs and complexity, we can improve the properties day by day.

#### **1.1.4 Optical Properties**

Graphene absorbs 2.3% of white light which is also an interesting property even though it is only 1 atom thick (Bonaccorso et al., 2010). This is due to its electronic properties; the electrons acting like mass less charge carriers with very high mobility. If another layer of graphene is added, it increases the amount of absorption by approximately the same value. In multilayer graphene the individual layers do not interact with each other optically since they behave as 2-dimensional electron gas (2DEG) (Huang et al., 2011). Therefore the absorbance of multilayer graphene is approximately proportional to number of layers. The absorbance of graphene remains almost constant in the range of 2- 3% from ultraviolet (UV) to infrared (IR) region compared to other transparent materials. Due to these impressive characteristics, it has been observed that once optical intensity reaches a certain threshold (known as the saturation fluence) saturable absorption takes place (very high intensity light causes a reduction in absorption). This plays an important role in case of the mode-locking of fiber lasers. Due to graphene's properties of wavelength-insensitive ultrafast saturable absorption, full-band mode locking has been achieved using an Er-doped dissipative soliton fiber laser capable of obtaining wavelength tuning as large as 30 nm.

#### **1.1.5 Chemical Sensing Abilities of Graphene**

A chemical sensor has to differentiate various chemicals under moderate conditions with detection sensitivities up to very low limit (ppm or ppb). The large surface area of graphene imparts sufficient sensitivity to detect even a single molecule

(Huang et al., 2011). The two-dimensional structure also permits a rapid response, allowing graphene to detect electron donor or acceptor gas molecules adsorbed onto its surface, a characteristic which makes it suitable for using as a chemical sensor. Adsorbed gas molecules change the local carrier concentration in graphene, causing changes in the resistance or the capacitance. Furthermore, graphene has high electrical conductivity and a  $sp^2$ -bonded hexagonal structure with almost no defects. Graphene has low thermal noise due to fluctuations, and the thermal motions of charges make it an excellent gas sensor material with high stability. These characteristics can initialize chemical sensing, which involves heating, annealing, and recycling.

## **1.2 Graphene Applications and Trends**

The combination of various amazing properties of the graphene enables its application in Sensor viz. Electrochemical Sensor, Gas Sensors, Biosensors; Hydrogen Storage Devices, Battery, Super-Capacitor/Ultra-Capacitors, Transparent Electrodes; Flexible Electronics, Touch Screen, Solar cells, Organic Photovoltaic Cells, Fuel Cells, Microbial Biofuel Cells, Enzymatic Biofuel Cells, Organic Light-Emitting Diodes; Spintronics, Integrated Circuits, Transistors, Ballistic Transistors, Radio Frequency Applications, Nano Antennas, Composite Materials, Liquid Crystal Displays, Quantum Dots, Frequency Multiplier, Optical Modulator, Infrared Light Detection, Graphene Photo detectors, Purification of Water etc. This list has been ever expanding as new applications are emerging by choosing, mixing and matching the properties of graphene alone or with combination with other materials (Iyechika, 2010). Figure 1.7 shows major

applications of graphene which have already been demonstrated utilizing different properties of graphene.

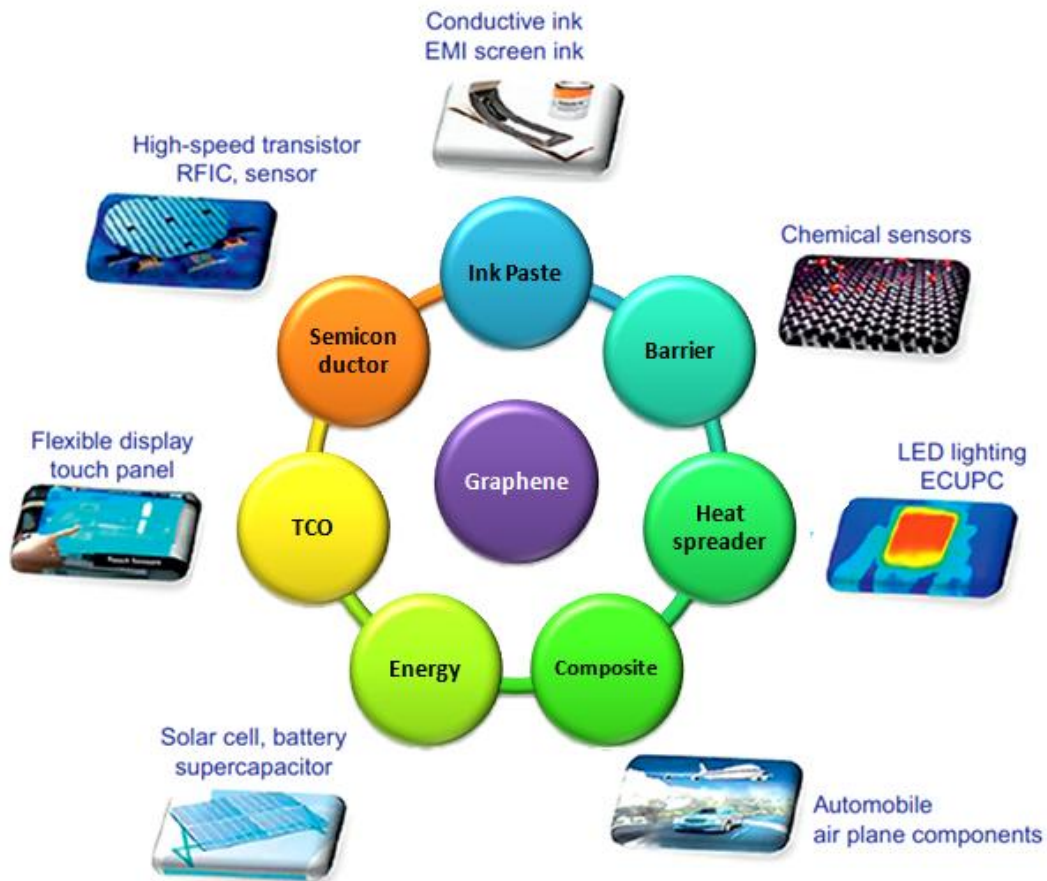


Figure 1.7. Overview of applications of graphene.

### 1.3 Overview of metal oxide semiconductors as sensors

#### 1.3.1 Motivation

The issue of air quality is still a major concern in many countries. A clean air supply is essential to our health and the environment. Therefore air pollution

determination is getting a lot of attention recently. Nitrogen dioxide (NO<sub>2</sub>) is an industrial pollutant which has adverse effect on human life and environment. The European Commission air quality standards suggest the NO<sub>2</sub> concentration should not exceed the limit of 40 µg/m<sup>3</sup> at averaging period of one year. Therefore, it is imperative to develop a highly sensitive and cost effective NO<sub>2</sub> sensor capable of detecting low concentrations of NO<sub>2</sub> gases. High performance gas sensors with high sensitivity, selectivity and lower response time are also needed to improve the levels of gas detection. Metal oxide gas sensors have been widely used in portable gas detection systems because of their advantages such as low cost, easy production, compact size and simple measuring electronics. Gas sensors based on nanomaterials are very potential to improve gas sensing properties in sensitivity, selectivity and response speed. The principle of operation of metal oxide sensors is based on the change in conductance of the oxide on interaction with a gas and the change is usually proportional to the concentration of the gas.

#### **1.4 Objective**

The following are the objectives of this study:

- (I) Growing large area, single layer, high mobility graphene by CVD technique.
- (II) Extracting electrical parameters of metal oxide/graphene Schottky junction from forward current-voltage (I-V) characteristics curves

(III) Investigate the sensing effects of  $\text{NO}_2$  and  $\text{NH}_3$  on transition metal oxide ( $\text{WO}_3$ ,  $\text{ZnO}$  and  $\text{In}_2\text{O}_3$ ) with and without graphene.

Growing device quality, high mobility, large area graphene still remains a challenge for mass production. Two approaches appear promising, namely epitaxial and chemical vapor deposition (CVD) based graphene growth. The later growth technique constitute the scope of this thesis and is discussed in chapter 2, which also focuses on Raman spectroscopy as the principle characterization technique of graphene to determine its quality and number of layers and even to determine if the grown material is graphene or not. Additionally, the current–voltage (I-V) characteristics will be measured for metal oxide semiconductor/Graphene Schottky barrier diode at different temperatures. From the forward bias region of the I-V curve the electrical parameters will be derived in different methods. The methods will also consider the series resistance to incorporate more non ideal behavior in the model. The parameters' dependence on temperature will be studied. This body of work will also focus on the sensing behavior of metal oxide semiconductors viz.  $\text{In}_2\text{O}_3$ ,  $\text{WO}_3$  and  $\text{ZnO}$  with  $\text{NO}_2$  and  $\text{NH}_3$  with and without graphene and their sensing time, sensitivity will also be compared. The findings of the above studies are presented as follows:

## **1.5 Layout of the Thesis**

**In chapter 1**, a rationale for the study of graphene/metal oxide heterojunction is given.

**In chapter 2**, literature related to graphene structures, properties, applications, growth are reviewed. Effect of  $\text{NO}_2$  and  $\text{NH}_3$  on metal oxides is also reviewed in this chapter.

**In chapter 3**, methodologies regarding growth and characterization of CVD graphene as well as fabrication of graphene/metal oxide heterojunction devices are presented.

**In chapter 4**, extraction of electrical parameters from I-V characteristics and sensing of the heterojunction are discussed. NO<sub>2</sub> and NH<sub>3</sub> sensing behaviors of the metal oxide with and without Graphene is presented.

**In chapter 5**, Summary and future aspects of the research are presented.

## CHAPTER 2

### LITERATURE REVIEW AND BACKGROUND

#### 2.1 GRAPHENE GROWTH

There are various methods to grow graphene. Each technique comes with its own set of challenges. Roughly there are four well-recognized methods. These methods include micromechanical cleavage, epitaxial growth, Chemical Vapor Deposition (CVD) growth and Reducing Graphene Oxide (RGO). Epitaxial and CVD growth methods have earned reputation for generating large area, good quality graphene. RGO is also capable of large area graphene however the crystalline quality of graphene remains comparatively poor. These growth techniques are surveyed briefly to put CVD based growth in perspective.

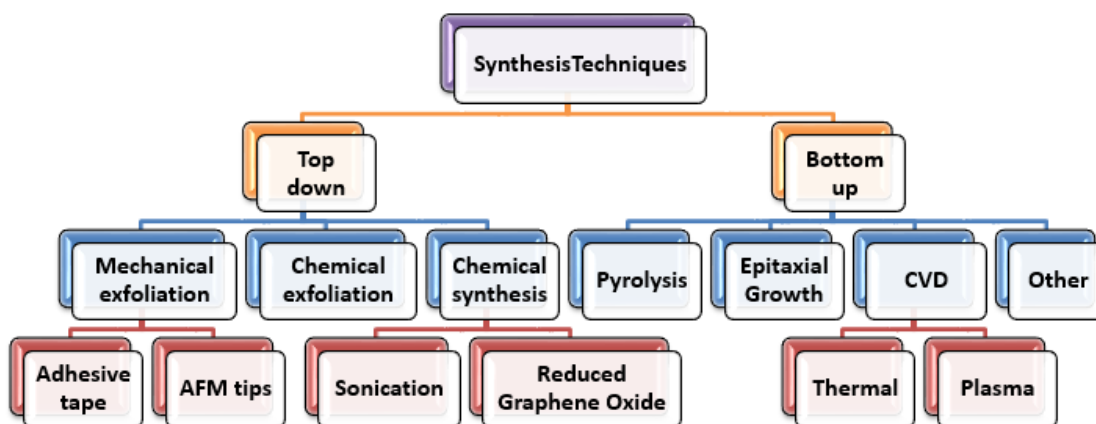


Figure 2.1. Different Synthesis Techniques of Graphene

##### 2.1.1 Micromechanical Cleavage and Ultra sonication



The first method is to use a lead pencil to deposit a thick layer of graphite onto a paper. Then ordinary sticky tape is used to peel off a layer of graphite from the paper. Next another piece of sticky tape is used to remove a layer of graphite from the first sticky tape. Then, third piece of unused sticky tape is used to remove a layer from the second piece of sticky tape, and so on. Eventually, the graphite layers will get thinner and thinner, and will result in with graphene, which is single-layer graphite in the rigorous sense, or bi-layer or few-layer graphite (which acts almost like graphene in certain uses). Although this way of making graphene is only for a proof-of-concept, the sticky tape method works (Martinez et al., 2011).

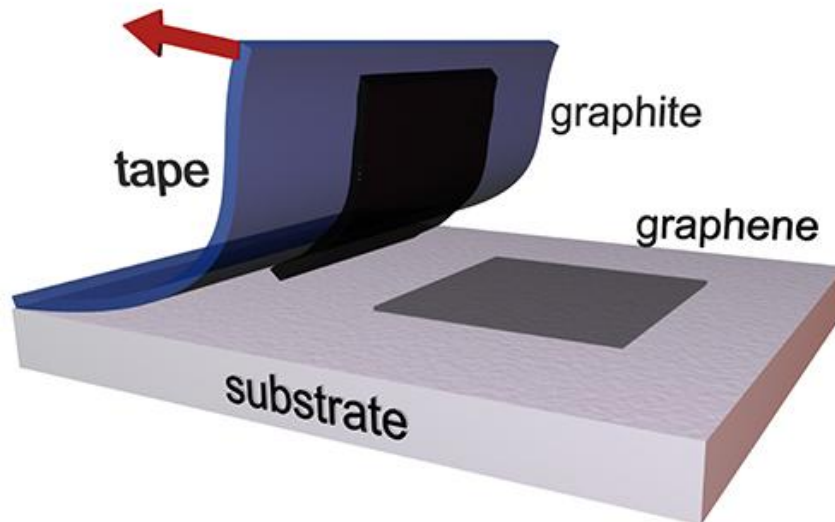


Figure 2.2. Scotch tape method

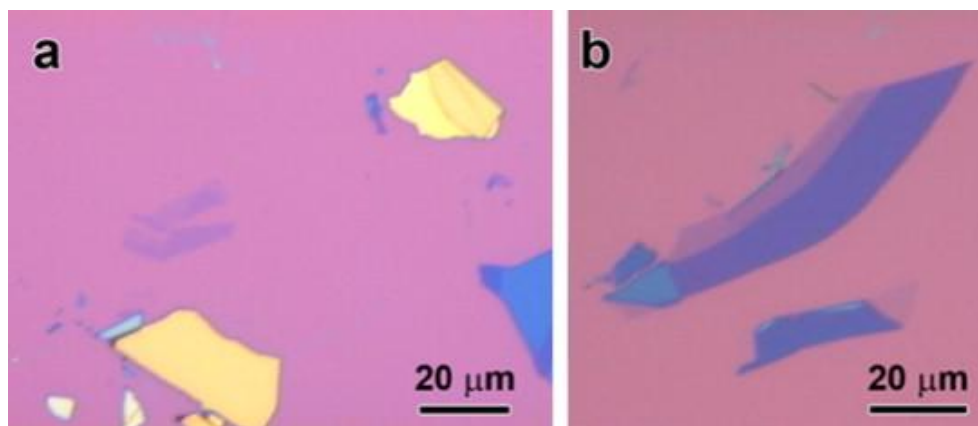


Figure 2.3. Micromechanically exfoliated graphene. Optical images of (a) thin graphene and (b) few-layer graphene (FLG) and single-layer graphene (lighter purple contrast) on a 300 nm SiO<sub>2</sub> layer. Yellow-like color indicates thicker samples (100 s of nm) while bluish and lighter contrast samples.

### 2.1.2 Sonication assisted liquid-phase exfoliation (LPE)

Graphite can be exfoliated in liquid environments by using ultrasound to separate individual layers. The liquid-phase exfoliation (LPE) (Fig. 2.4) process normally involves three steps:

- (1) Dispersion of graphite in a solvent
- (2) Exfoliation
- (3) Purification.

Graphene flakes can be obtained by surfactant free exfoliation of graphite through wet dispersion and ultra-sonication in organic solvents. Shear forces and cavitations

induce exfoliation during ultra-sonication. After exfoliation, the solvent–graphene interaction needs to balance the Van Der Waals forces. Solvents minimize the interfacial tension between the liquid and graphene flakes (Ciesielski and Samorì, 2014; Hernandez et al., 2008).

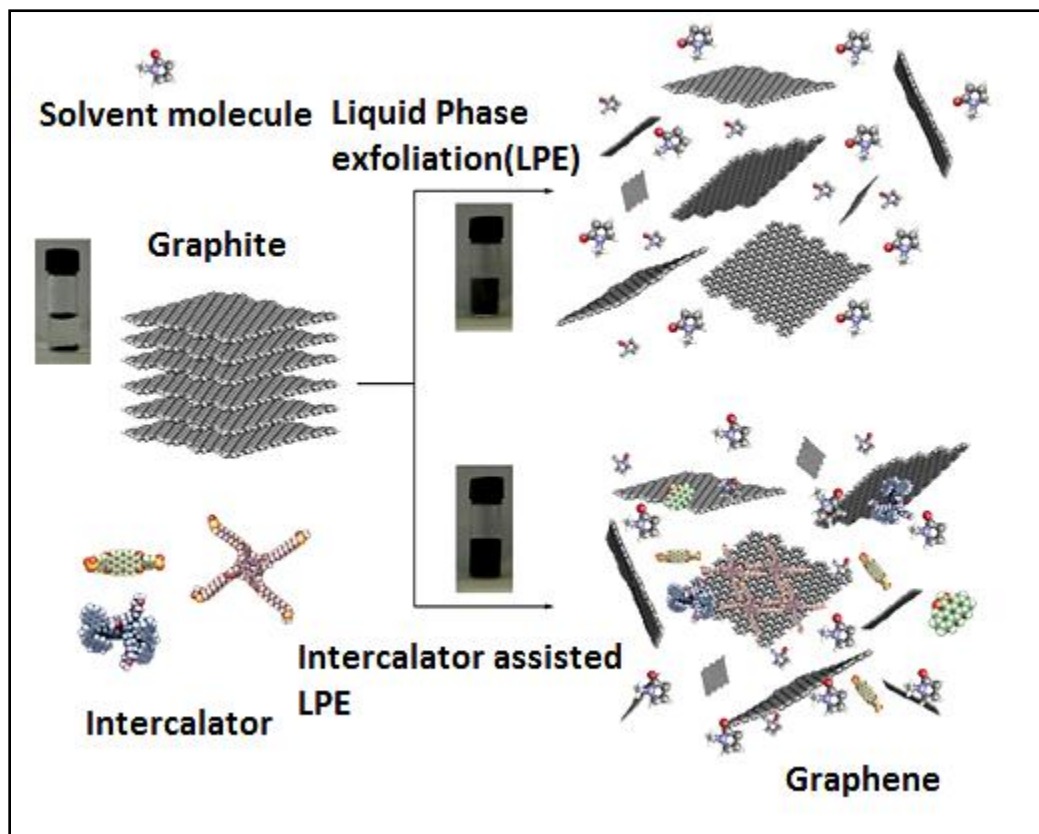


Figure 2.4. Liquid-phase exfoliation process of graphite in the absence (top-right) and presence (bottom-right) of surfactant molecules.

### 2.1.3 Epitaxial Growth

Epitaxial growth means growth of a crystalline layer on a crystalline substrate which follows the structure of the substrate. The deposited layer is called the epitaxial

layer. It is a impending method to produce a large area, uniform thickness and high quality graphene (Berger et al., 2004). The method is based on annealing the SiC crystal at high temperature; primarily Si leaves the SiC crystal, leaving a carbon-rich surface behind during sample annealing. As Si has a higher vapor pressure than C in the SiC substrate, the Si atoms therefore desorb first from the sample surface during the annealing process, leaving the C atoms behind, and allow a carbon-rich surface to emerge until the final graphene is formed (Gao et al., 2011). The high temperature enables ordered and clean graphene. In this method SiC is heated in the temperature range of 1200 °C – 1600°C in ultra-high vacuum (UHV) of  $1 \times 10^{-10}$  Torr for several minutes. At this high temperature Si leaves the SiC. The remaining C rich surface then rearranges on the hexagonal lattice of SiC to generate few layers graphene (De Heer et al., 2011; Hass et al., 2008; Hu et al., 2012).

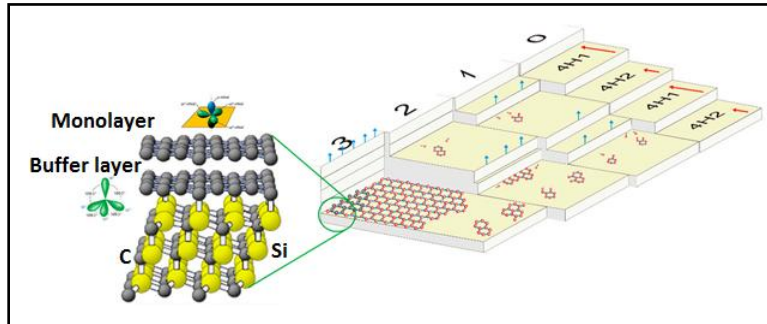


Figure 2.5. Formation process of epitaxial graphene via sublimation of Si from the SiC surface.

One of the advantages of this technique is that it does not need the transfer of the graphene layer to another substrate. So we can make electronic devices to be fabricated directly on SiC. However, it has its drawbacks too. This can be expensive due to the high cost of SiC substrates, and also it does not readily allow the usage of a back gate for realizing transistors, or sensors requiring back-gate modulation.

#### **2.1.4 Reduced Graphene Oxide (RGO)**

The oxidation method followed by exfoliation of graphite methods can produce large quantities of graphene oxide (GO). However it is typically defective and demands additional treatments to reduce it to reduced graphene oxide (RGO) (Zhu et al., 2010). After the attachment of the oxygen-containing functional groups during the oxidation process increases the distance between graphitic layer which weakens the Van Der Waals forces and accelerates exfoliation. Several washing steps are needed before the exfoliation in order to remove oxidizing agents and other impurities from graphite oxide. Washing the graphite oxide by filtration, centrifugation is a really clumsy. Filtration processes are extremely time-consuming since exfoliated graphite oxide particles quickly clog the filter pores. Moreover, high-speed centrifuge systems are less common in industrial applications due to their limited capacities and high costs (Compton and Nguyen, 2010). On the other hand, the dispersibility of GO increases by the progression of washing steps. Regardless of the oxidation process, reduction adds yet another step to the synthesis procedure, prolonging the overall production time.

Chemical reduction of GO is one of the conventional procedures to prepare graphene in large quantities. GO is usually synthesized through the oxidation of graphite using oxidizing agents including concentrated sulfuric acid, nitric acid and potassium permanganate. Another approach to the production of graphene is sonication and reduction of GO. Large excess of  $\text{NaBH}_4$  have been used as a reducing agent. GO was formed by the chemical reaction between organic isocyanates and the hydroxyl is shown in Fig. 2.6.

Electrochemical reduction is another means to synthesize graphene in large scale. The graphite oxide solution can then be sonicated in order to form GO Nano platelets. The oxygen groups can then be removed by using a hydrazine reducing agent, but the reduction process was found to be incomplete, leaving some oxygen remaining. GO is useful because its individual layers are hydrophilic, in contrast to graphite. GO is suspended in water by sonication then deposited on to surfaces by spin coating or filtration to make single or double-layer graphene oxide. Graphene films are then made by reducing the graphene oxide either thermally or chemically a simple thermal reduction method to produce RGO. (Compton and Nguyen, 2010, 2010; Robinson et al., 2008)

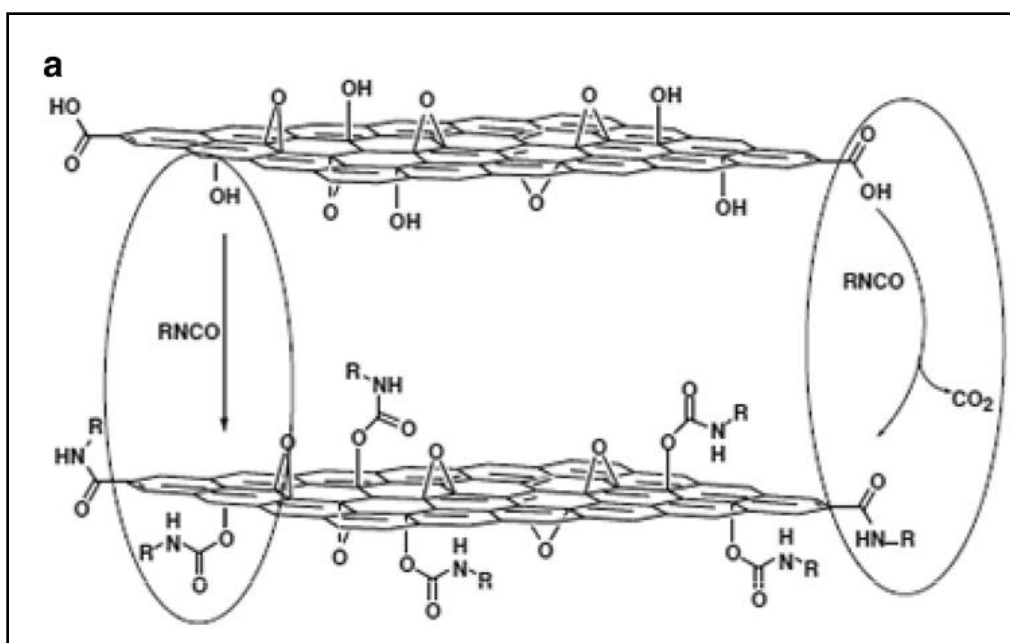


Figure 2.6. Proposed reactions during the isocyanate treatment of GO where organic isocyanides react with the hydroxyl (left oval) of graphene oxide sheets to form carbamate and amide functionalities.

Although it's a good method for large scale production which can be utilized in energy storage applications where large quantity is exclusively necessary rather than high quality. As there are several solvents, oxidizing, reducing agents involved, defects are almost inevitable. Another challenge involved is controllability. There is little to tune viz. thickness, number of layers, uniformity etc.

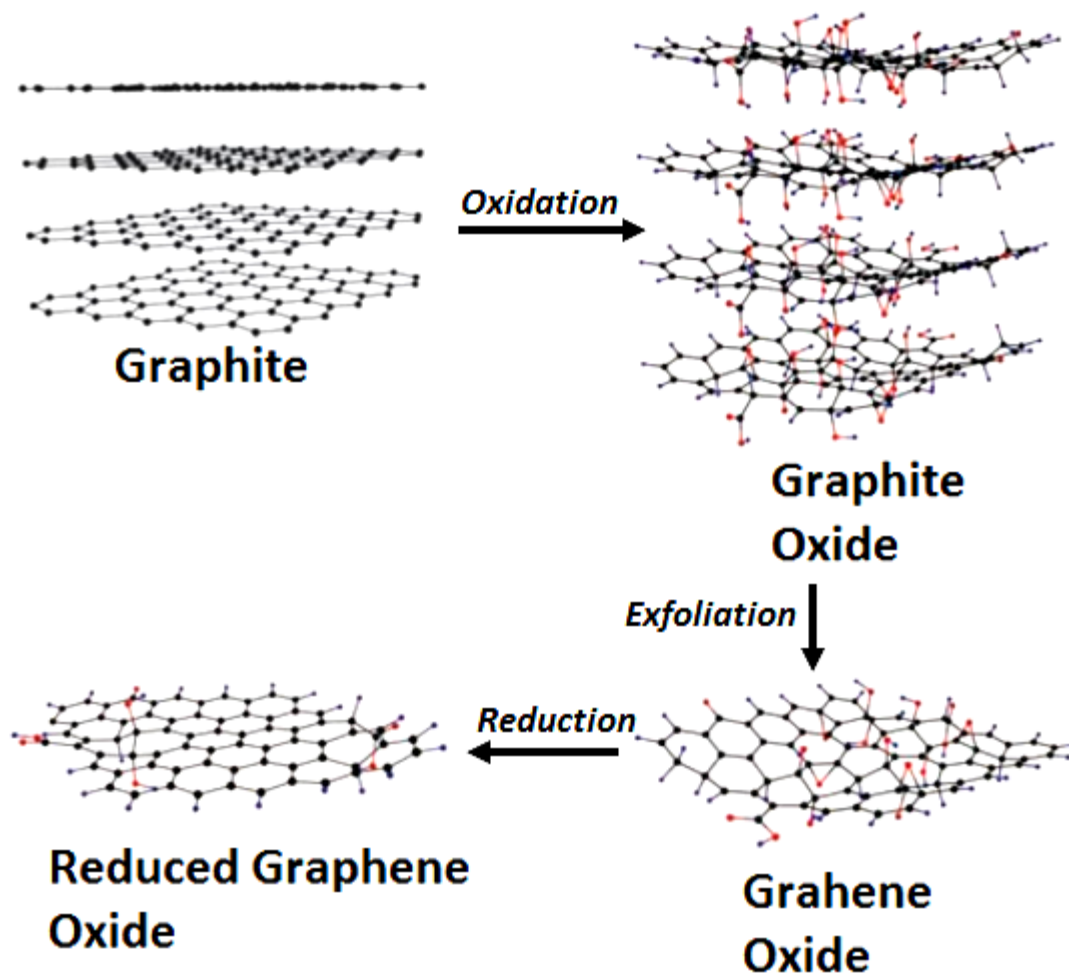


Figure 2.7. Graphene oxide and reduced graphene oxide preparation

### 2.1.5 CVD Growth

Segregation of carbon impurities to interfaces or free surfaces of a metal in the solid phase was observed in the 1960s. This segregation is determined by super saturation of carbon impurities in the material. Assuming an ideal solution, the carbon solubility in a transition metal can be expressed as:



$$\ln X_C = \frac{\Delta G}{kT} \quad (2.1)$$

Where  $X_C$  is the carbon concentration,  $T$  is the system temperature,  $k$  is the Boltzmann constant and  $\Delta G$  is the difference in chemical potential between a pure solvent and the solvent with diluted carbon impurities. This relation defines the maximum carbon content at a given temperature beyond which a second phase is developed under thermodynamic equilibrium (Fig. 2.8). In the case of carbon diluted in a transition metal, super saturation leads to carbon segregation and the nucleation of a graphitic phase.

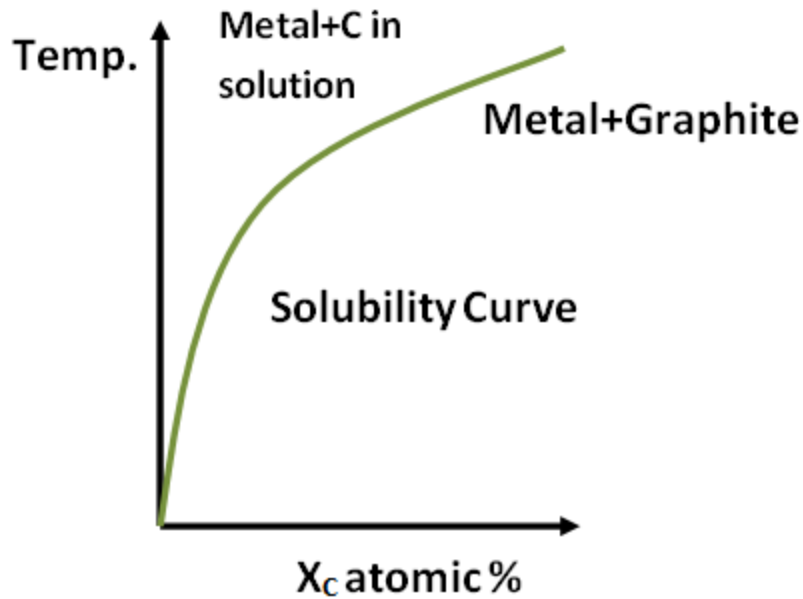


Figure 2.8. Solubility curve for Carbon in a transition metal.

Polycrystalline metallic thin films can also be used to fabricate graphene films in ambient pressure CVD (APCVD) via a carbon segregation mechanism. The use of

metallic thin films (200–500 nm) is advantageous since they are readily obtained and they are of lower cost than single-crystalline substrates. The use of thin films also facilitates the transfer of the graphene to different substrates. The thin films are deposited by e-beam evaporation or by sputtering on oxidized silicon substrates with 100 nm (or 300 nm) of silicon dioxide (Hu et al., 2012; Muñoz and Gómez-Aleixandre, 2013; Suk et al., 2011). Typically, CVD processes for graphene growth by carbon segregation involve three stages (Fig. 2.9):

#### **2.1.5.1 Stages of CVD growth**

**1. Annealing of the metal film:** In this stage the catalyst film is annealed at temperatures between 900C and 1,000C in order to induce its recrystallization. Increased grain size can help in avoiding excess nucleation sites for amorphous carbon or multilayer graphene. Moreover, by annealing the thin film, it is possible to induce a preferential texture of the film in the case of some metals (e.g. towards the (111) orientation for FCC metals). This is desired, for example, in the case of Ni (111) due to its lattice matching with graphene. The annealing treatment is typically done under gas mixtures of Ar and H<sub>2</sub>.

**2. Exposure to CH<sub>4</sub>:** After the annealing, the surface is exposed to diluted CH<sub>4</sub> gas. The hydrocarbon gas can also be introduced with a mixture of Ar and H<sub>2</sub>. The temperature during this part of the process can be the same or different from the annealing temperature. It is expected that methane is decomposed catalytically on the

surface of the metal to produce carbon atoms on its surface. The following reaction is used to describe the decomposition:

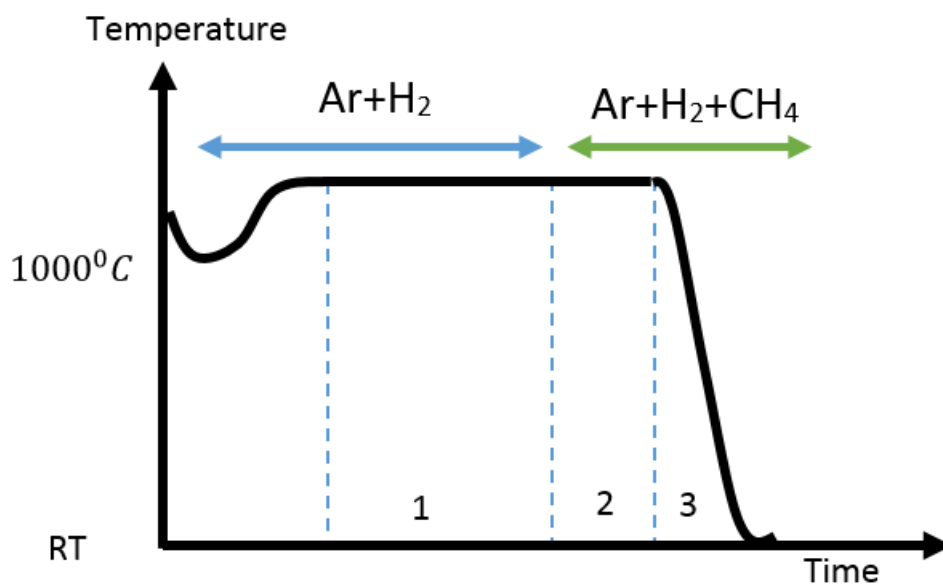


Figure 2.9. Temperature vs. time diagram of APCVD showing different steps (1) annealing the catalyst metal foil, (2) exposure CH<sub>4</sub> and (3) Cooling

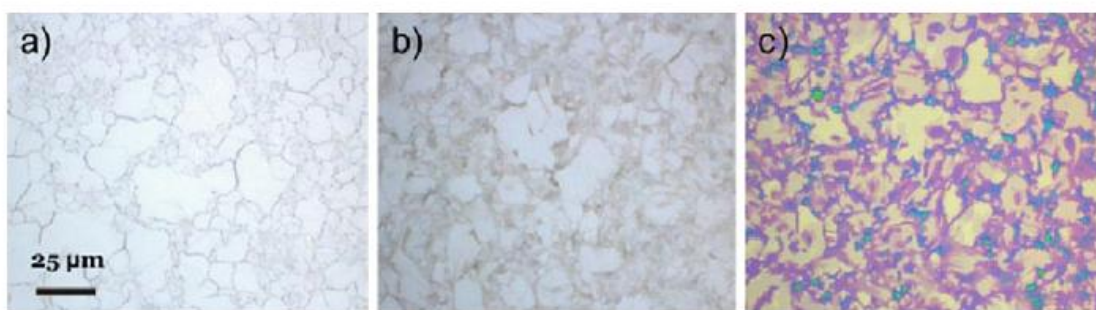
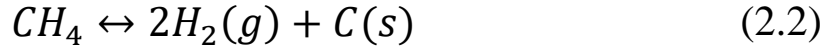


Figure 2.10. Optical images of (a) Ni foil annealed (b) Graphene transferred on SiO<sub>2</sub>/Si (c) dark features indicates presence of Graphite and FLG



However, such decomposition may involve transitional steps involving other hydrocarbons such as ethylene ( $C_2H_4$ ) and acetylene ( $C_2H_2$ ). Since this process occurs at temperatures around 900–1000°C, it is expected that diffusion of C to the bulk of the film occurs for metals with high carbon solubility at that temperature, e.g. Ni (1% at.).

Figure 2.10 (a) compares a pure Ni film which was annealed, a Ni film after the three process steps described above and the graphene film transferred onto a  $SiO_2/Si$  substrate. The dark features in Fig. 2.10 (b) suggest the presence of FLG and graphite. Their nucleation distribution depends on the grain size of the initial Ni film. The clear regions contain SLG or BLG and these tend to be away from the grain boundaries of the Ni film. They can only be detected optically once the graphene film has been isolated from the Ni and transferred to a  $SiO_2-Si$  substrate. By manipulating the Ni grain size, it is possible to change the morphology and optical properties of the grown graphene films.

**3. Cooling of the metallic film:** Cooling the sample promotes the separation of C stored inside the film. The carbon isolated to the surface initiates the growth of SLG and FLG. The cooling rates typically used are between 4 and 100°C/min.

#### 2.1.5.2 Growth on Copper Foil

Copper is a better choice for thinner graphene growth compared to Nickel since C is less soluble in it. When copper foil is exposed to  $CH_4$  gas (e.g. >1000°C) the carbon starts depositing on copper surface due to dehydrogenation. After adsorption the crystal

size starts growing after nucleation. It has been proved that C is less soluble in copper and to prove that  $C^{12}$  and  $C^{13}$  isotopes were used. After flowing  $C^{13}$  isotope, the adsorption, dehydrogenation occurred and the nucleus size starts growing in size. Then  $C^{12}$  isotope is released and it's been seen that the black  $C^{12}$  isotopes are coalescing around the edges of the previously formed crystal, not randomly nucleating and making the film thicker. It proves that no C atoms are dissolved into the bulk, rather nucleating across the surface (Li et al., 2009). Thus copper foil is better choice for thinner graphene and it doesn't depend much on the cooling rate as well as  $CH_4$  flow rate.

The CVD synthesis steps is summarized in fig. 2.11

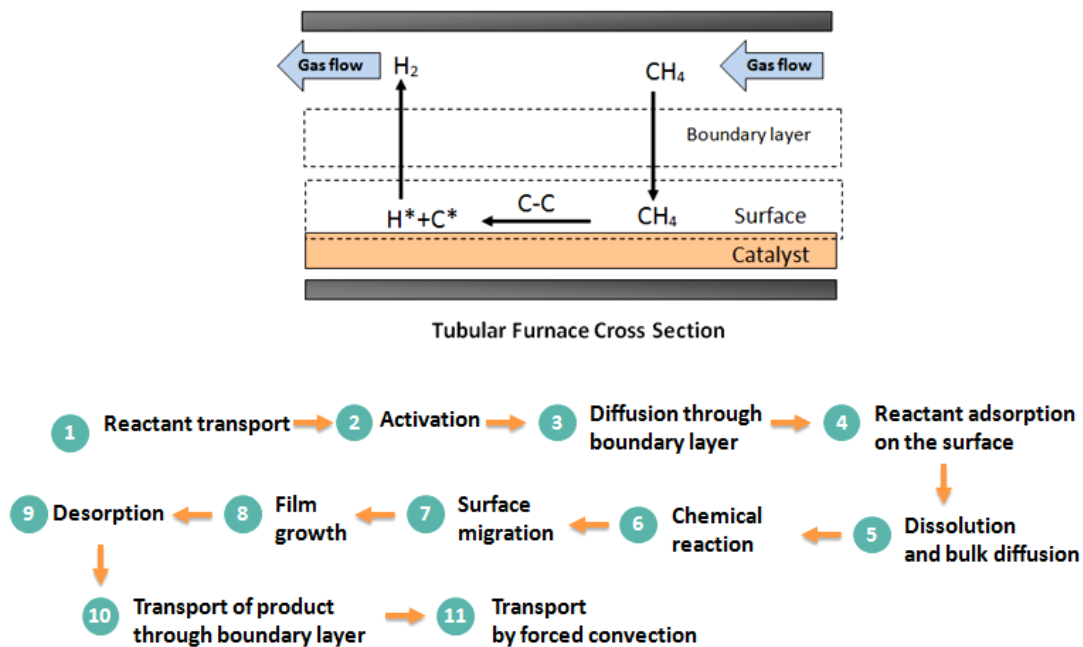


Figure 2.11. Stages involved in CVD synthesis of graphene

### 2.1.5.3 Advantages and challenges of Graphene CVD

There are number of advantages and also associated challenges in CVD growth technique (Muñoz and Gómez-Aleixandre, 2013). They are stated in Table 2.1

Table 2.1 Advantages and challenges of CVD grown graphene

<b>Advantages</b>	<b>challenges</b>
1. Relatively low operating temperature (i.e., ~1300 K or lower, which is significantly lower than the temperature required for SiC sublimation, i.e., 1900–2300K)	1. High concentrated grain boundaries.
2. High quality single-layer (SLG) or a few-layer (FLG) graphene which is readily synthesizable because of catalyst-assisted defect healing.	2. Controlling the number of graphene layers is another challenge since properties of graphene have a strong dependence on the number of layers, hence.
3. Very large area graphene	3. Graphene CVD growth can be achieved by using many different carbon precursor, among them CH <sub>4</sub> is mostly used and shows great advantages on single-

	<p>layer graphene growth. The differences between carbon precursors are not well addressed. As the feedstock decomposition occurs on the catalyst surface, the difference must be associated with the type of catalyst surface.</p>
<p>4. Easily transferrable onto other substrates for further processing or device fabrication.</p>	<p>4. Selection and design of proper catalysts as different catalysts and the catalyst surface types, affect graphene growth behavior greatly. Obtaining one catalyst leading to a high quality, large area SLG is greatly desired.</p>

<p>5. There are many tunable parameters, such as type of catalyst, pressure and type of precursor and carrier gases, temperatures and so on. With these parameters, we can easily develop many more different recipes. So, CVD synthesized graphene quality can be improved further.</p>	<p>5. Proper graphene growth conditions.</p> <p>For each combination of precursors and catalyst, varying the temperature, the partial pressures of precursors and hydrogen in the carrier gas will greatly influence the graphene growth. So, to determine the optimum condition for each combination of feedstock and catalyst is a big challenge because there are probably several hundred different combinations.</p> <p>6. Graphene CVD growth is broadly named as the epitaxial process.</p> <p>Graphene normally interacts with the catalyst surface that has the weaker Van der Waals interaction. However, experimental observations show that there are normally one or a few preferred orientations for the graphene grown on each type of catalyst surface. So, what</p>
--	--



	is the mechanism of graphene orientation determination during growth is another big challenge.
--	--

#### 2.1.5.4 Comparison of all methods

All the methods come with their own sets of advantages and challenges. They are given in the following table 2.2

Table 2.2 Comparison of all four graphene growing techniques

Methods	Advantages	Challenges
<b>Exfoliation</b>	Structural and electronic quality, good for ‘proof-of-concept’ devices	Low yield, controllability
<b>Epitaxial</b>	Uniform, wafer scale, high quality due to commercial SiC process parameters	Transferability, lattice mismatch, lack of back gate
<b>RGO</b>	Good for energy storage device where large scale but not high quality is needed	Defects, controllability

<b>CVD</b>	Lower operating temperature than SiC, high quality , large area SLG, transferability	Controlling number of layer, optimum growth condition, high grain boundaries
------------	--	--

## 2.2 Raman spectroscopy

Raman spectroscopy is a characterization tool that is based on the vibration of the molecules. It is highly dependent on the geometrical structure of the molecules. Even a little difference in geometry might cause a significant change in the output spectrum. Thus it has become indispensable in characterizing CNT, graphite, Bucky ball, graphene etc. which are allotropes of C only differing in relative carbon atom positions and atomic bond (Dresselhaus et al., 2010).

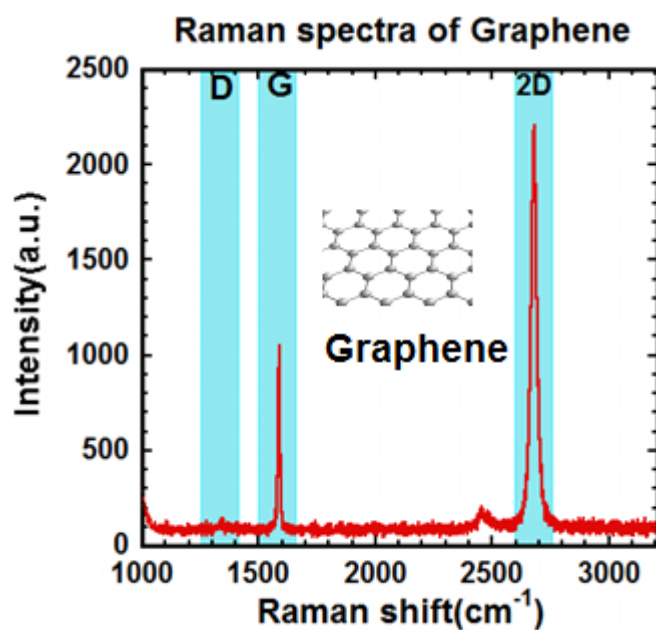


Figure 2.12. Raman spectra of SLG with 532nm Laser excitation

The above is the Raman spectrum of graphene. From the figure we can see three prominent peaks namely G, 2D and also sometimes D peak which is only present if there is defect in graphene (Malard et al., 2009).

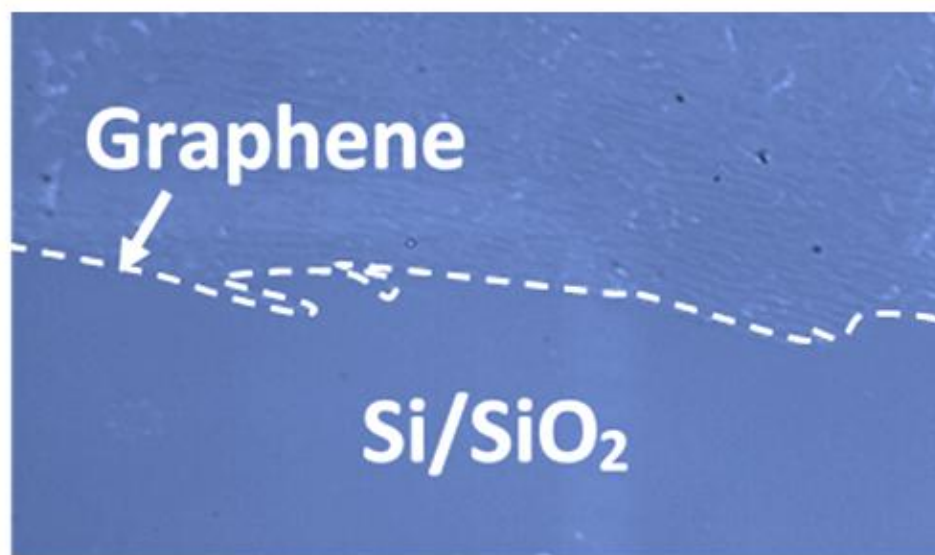


Figure 2.13. Optical image of Graphene/SiO<sub>2</sub>

Raman spectroscopy uses a monochromatic source of laser which interacts with the different vibration modes of the molecules either shifting the laser energy up (anti-stokes) or down (stokes) due to inelastic scattering mechanisms. And by investigating the shift defects, number of layers, thickness, doping, strain, thermal conductivity, disorder, edge and grain boundaries can be detected.

In the Raman spectroscopy there are mainly two peaks: (1) G-band and (2) D-band. G ( $1580\text{ cm}^{-1}$ ) is the primary in-plane vibration mode while 2D ( $2690\text{ cm}^{-1}$ ) is the overtone of another in-plane vibration mode namely D ( $1350\text{ cm}^{-1}$ ). The G-band is very responsive to strain in  $\text{sp}^2$  system, and so it can be utilized to probe alteration on the flat surface of graphene.

All  $sp^2$  bonded Carbon exhibit another strong peak in the range of  $2500\text{-}288\text{ cm}^{-1}$  range. This is another signature of graphitic material. It is called 2D band which arises from a second order 2 phonon process. 2D band is useful for finding the number of layer of graphene because in the multi-layer graphene, the shape of 2D band is different from that in the single-layer graphene. The 2D band in the single-layer graphene is much more strong than the 2D band in multi-layer graphene (Cançado et al., 2011).

As the number of graphene AB Bernal stacking increases there is a change of forces acting in between which causes the D band to be wider, shorter and distorted comprising of different Gaussian fits. Thus, for AB-stacked graphene, the number of layers can be derived from the ratio of peak intensities,  $I_{2D}/I_G$ , as well as the position and shape of these peaks. The first order D-peak cannot be seen in pure crystalline graphene because of the symmetry. The reason for the manifestation of D-peak is excitation of carriers scattered by a phonon and a second scattering from the defect sites. With increasing number of defects, three separate disorder peaks arrive: D ( $1350\text{ cm}^{-1}$ ), which scatters from intervalley transition (K to K'), D' ( $1620\text{ cm}^{-1}$ ) that results from intravalley scattering; and D+G ( $2940\text{ cm}^{-1}$ ), a combination scattering peak (Ferrari and Basko, 2013).

Using  $I_D/I_G$  ratio, we can find the level of defects. There are two regions: (1) Low defect density region where the ratio will increase as the higher defects causes more elastic scattering (2) high defect density where the ratio starts to decrease as in this region an increasing defect density will make the structure more amorphous which attenuates

all Raman peaks. These regions are due to the two areas possessing two particular defect sites: (1) an area with radius  $r_s$  which has structural disorder and impacts the D peak weakly (2) an area with radius  $r_a$  ( $r_a > r_s$ ) which is close to the defect site to be activated and increase the D peak. If the average distance between defects,  $L_D > 2r_a$ , graphene is considered to be nanocrystalline graphite. These two regions are defined by the following formula:

$$\frac{I_D}{I_G} = C_a \frac{r_a^2 - r_s^2}{r_a^2 - 2r_s^2} \left[ \exp\left(-\frac{\pi r_s^2}{L_D^2}\right) - \exp\left(-\frac{\pi(r_a^2 - r_s^2)}{L_D^2}\right) \right] \quad (2.3)$$

$$+ C_a \left[ 1 - \exp\left(-\frac{\pi r_s^2}{L_D^2}\right) \right]$$

$C_a$  and  $C_s$  describe the strength of the contribution from respective regions to the D-peak. The ratio  $I_D/I_G$  and  $L_D$  can be approximated by two empirical formulas for the two separate regions: for low defect density region:

$$\frac{I_D}{I_G} = \frac{C(\lambda)}{L_D^2} \quad (2.4)$$

$\lambda$  is the excitation wavelength of the laser and for  $C(\lambda) = 102nm^2$  for  $\lambda = 514nm$  .

And for edge defects rather than point defects the formula is like the following:

$$\frac{I_D}{I_G} = \frac{C'(\lambda)}{L_D} \quad (2.5)$$

Where  $C'(\lambda) = (2.4 \times 10^{-10} nm^{-3})\lambda^4$

For the high defect density region (almost full breakdown of lattice symmetry), the formula is:

$$\frac{I_D}{I_G} = D(\lambda) \times L_D^2 \quad (2.6)$$

Where  $D(\lambda)$  can be found by imposing continuity between the two regimes.

In order for a D peak to occur, a charge carrier must be excited and inelastically scattered by a phonon, then a second elastic scattering by a defect or zone boundary must occur to result in recombination. The second order overtone, 2D, is always allowed because the second scattering (either on the initially scattered electron/hole or its complementary hole/electron) in the process is also an inelastic scattering from a second phonon [ Fig. 2.14]

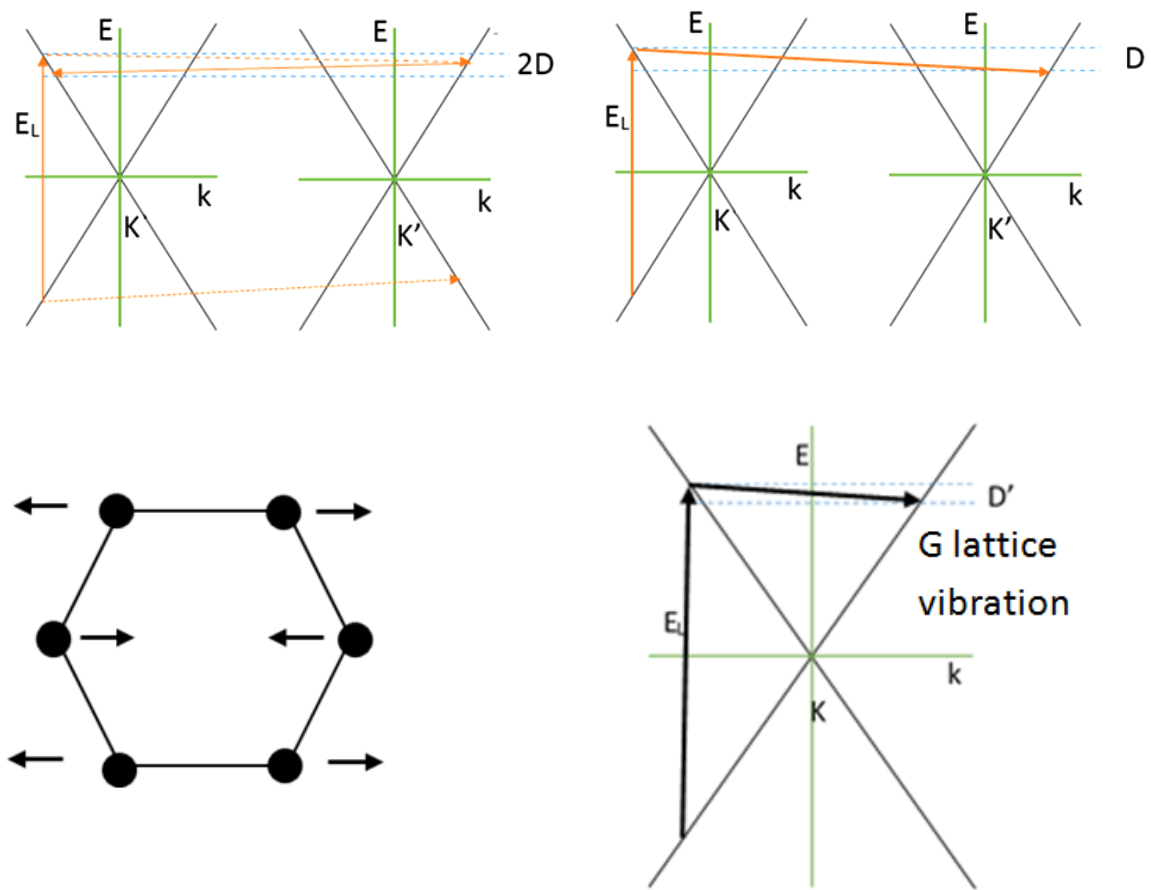


Figure 2.14. (Top) Graphical representations of examples of phonon scattering processes responsible for the significant graphene Raman peaks. The D (intervalley phonon and defect scattering) and D' (intravalley phonon and defect scattering) peaks appear in disordered graphene. The 2D peak involves double phonon scattering.



## CHAPTER 3

### MATERIALS AND EXPERIMENTAL PROCEDURES

#### **3.1 CVD Furnace Components**

CVD involves several components and steps. It needs a source of Carbon e.g. in our case it is methane gas. There should be a catalyst which will work as the substrate and reduce the requirement of heat needed. In our growth copper foil works as the catalyst substrate. There are several physical conditions such as pressure, temperature and carrier gas play a big role in production of graphene. Our carrier gas was Argon and Hydrogen. They accelerate the surface reaction rate. The chamber material is also of great importance. Ours is a quartz tube because of its inert nature as well as high melting point.

##### **3.1.1 CVD Furnace**

MTI 1200°C Split Tube Furnace with quartz tube (60mm diameter) was used. Quartz is the best choice because of its very high melting point and chemical inertness. In other words, quartz does not interfere with any physical or chemical reactions whatever the condition is.

##### **3.1.2 Mass Flow Controller (MFC)**

MKS Instruments 1179A Mass-Flo General Purpose Mass Flow Controller (Model # 1179A00413CS1BV) with range 1000 sccm was used. It was controlled by MKS 247 4-channel readout control box for setting gas flow rates.

### **3.2. CVD growth of graphene**

There are many types of CVD mechanism viz. APCVD, LPCVD, and UHVCVD depending on the pressure involved. Ours is somewhat Low Pressure CVD (LPCVD) because of its low base pressure (sub-atmospheric) and growth pressure. The details are as follows:

#### **3.2.1 Substrate cleaning**

The Cu foil was sonicated for 2 minutes with Acetone to remove any organic particles, followed by washing with Isopropanol (IPA). After that nitric acid (diluted to 20-30%) was used for 10-60 seconds for flattening Cu and oxidizing. After drying with N<sub>2</sub> (or air) gun, it was sonicated for 10 minutes with acetic acid to remove the existing oxides like CuO and Cu<sub>2</sub>O. After cleaning all chemical particles with IPA it was dried with N<sub>2</sub> gun again. The steps are given in fig. 3.1 and the steps are explained in table 3.1

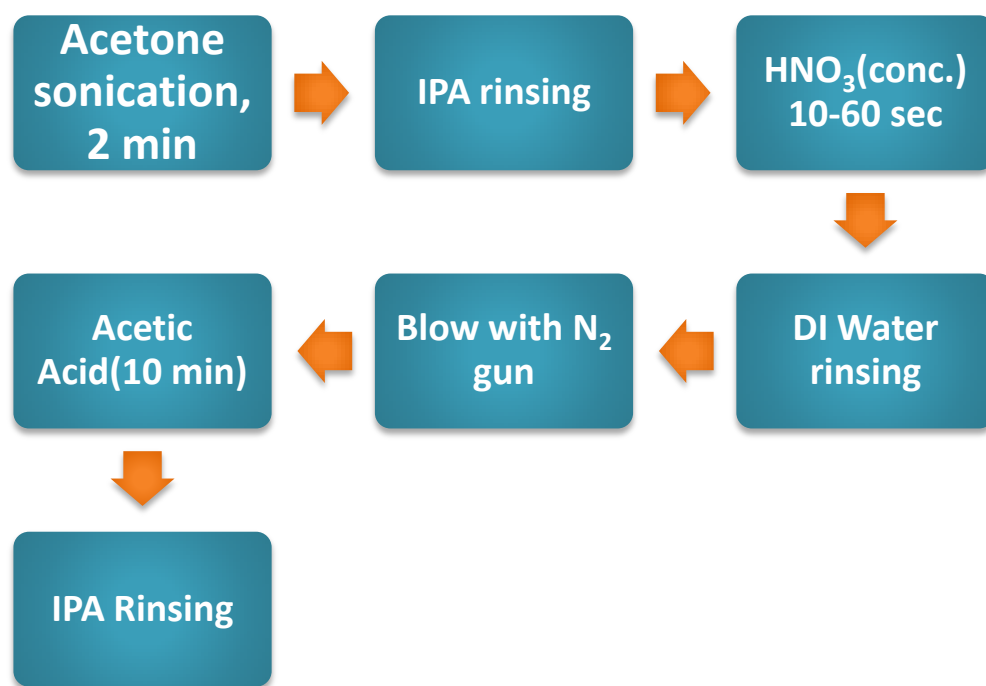


Figure 3.1. Substrate (Cu foil) Cleaning Steps

Table 3.1 Basic steps of cleaning copper substrate explained

	Process	Purpose
<b>Clean Cu foil</b>	Acetone,sonication,2 min	Removes organic particles  by dissolving grease like contaminants but evaporates quickly re- depositing them again.
	IPA rinsing	Removes acetone residue particles dissolving

		acetone and contaminant residue but doesn't evaporate so fast.
	HNO <sub>3</sub> (conc.) 10-60 sec	Flatten the foil and oxidize any unwanted reagents.
	DI Water rinsing	Remove HNO <sub>3</sub>
	Blow with N <sub>2</sub> (or air) gun	Dry Cu foil
	Acetic Acid, sonicate 10 min	Remove oxide such as CuO and Cu <sub>2</sub> O
	IPA rinsing	Remove chemical particles
	Blow with N <sub>2</sub> (or air) gun	Dry Cu foil
<b>Make mark on Cu foil</b>	Make a mark with scissors	Scissors should be cleaned first

### 3.2.2 Growth steps

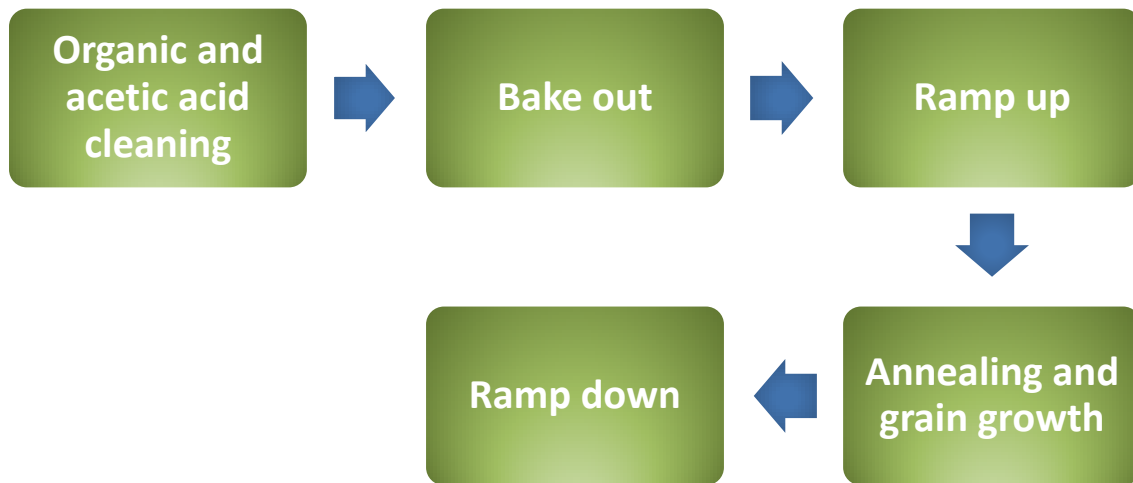


Figure 3.2. Steps of CVD graphene growth on copper substrate

Ours is a semi-automated system for CVD growth with LabVIEW software. At first we evacuated the quartz chamber and reached 0.5 Torr after starting the pump. Then opening the outer flanges, we inserted the copper foil on to top of a square quartz plate in Ar atmosphere. The temperature was ramped up from 250<sup>0</sup>C to 1000<sup>0</sup>C and annealed in H<sub>2</sub> atmosphere for around 2 hours to enlarge the size of the crystalline quality. The actual growth was done at 1035<sup>0</sup>C and CH<sub>4</sub> was flown at this stage. After 20 minutes of growth the heater was turned off to cool down naturally until the set temperature differs the actual value by 100<sup>0</sup>C. Then we opened the lid of the furnace to expedite the cooling process. The optimized parameters are shown in fig. 3.3.

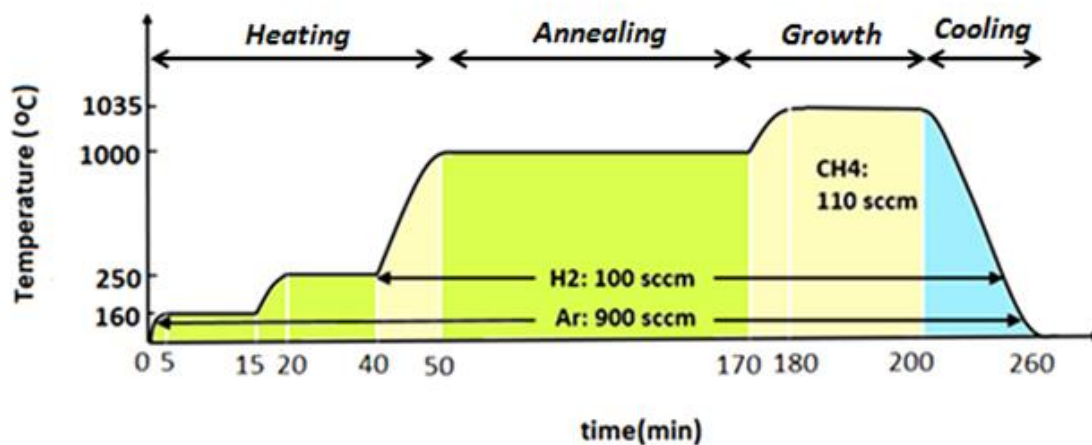


Figure 3.3. Temperature profile for CVD growth of graphene

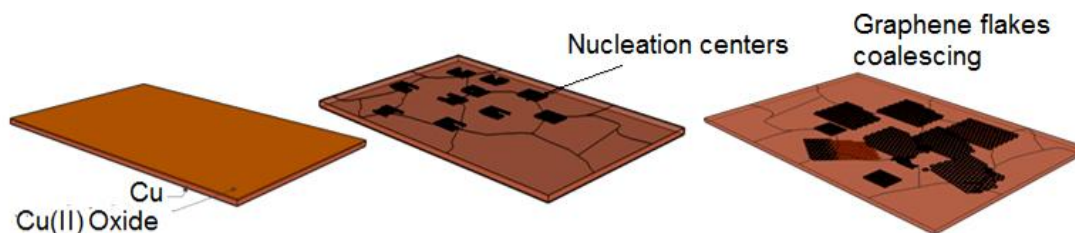


Figure 3.4. Nucleation and subsequent phases of graphene growth on copper

### 3.2.3 Procedure

A CVD reactor which involved a 1200°C split tube furnace with quartz tube (60mm diameter) and a rotary vane pump was built. The precursor gas was CH<sub>4</sub> and carrier gases were Ar and H<sub>2</sub> which were controlled by mass flow controllers (MFC). 25 μm thick Cu films (**99.999%, Alfa Aesar**) was used as a substrate and catalyst for CVD growth of graphene. Raman characterization (discussed later) confirmed the growth of

monolayer (SLG) to few-layer (FLG) graphene film. The setup consists of the three gas cylinders, namely CH<sub>4</sub>, H<sub>2</sub> and Ar each of which were connected to the corresponding MFC through manual ball valves and ¼” stainless steel tubing. The stainless steel tubing serves to provide higher conductance path and better leak characteristics as compared to polyethylene tubing. The MFCs were MKS Type 1179A each calibrated for the gas being used. Ar flowrate was set to 1000 sccm range for flowing larger amount of Ar and a carrier and diluent gas. H<sub>2</sub> and CH<sub>4</sub> MFC set point were 200 and 50 sccm for keeping CH<sub>4</sub> to H<sub>2</sub> ratio low during the growth. The output from MFCs is joined together using a Swagelok Union Cross. One end of the cross is connected to the ¼” quartz delivery tube by a flexible teflon hose. The reaction chamber consists of 60 mm outer diameter, 55 mm inner diameter and 1 m long quartz tube. It is also fitted with Alumina Foam heat block of 52 mm diameter at both the ends. The enclosure is formed by stainless steel flanges. The substrate is mounted on a flat quartz plate (1.5 in x 1.5 in x 1/8 in thick). The other end of the chamber has one outlet connected to stainless steel tubing with a teflon tube. A Bourdon tube pressure gauge and a Pirani gauge (901P Micro Pirani/Piezo Loadlock Vacuum Transducer) are attached downstream to this stainless tubing to monitor the pressure of the system. This tubing then connects to the inlet of a Dual Stage Rotary Vane Mechanical Vacuum Pump from Ideal Vacuum (Alcatel 2021 2021SD Pascal SD) with a capability of 10 mTorr ultimate pressure. Alongside the pump there was an Oil Mist Eliminator (Model: Pfeiffer ONF 10-12, ONF 25 S for Duo 10M, DN/ISO/KF 25 Outlet Flange) which can reduce part of the vacuum pump's exhausted oil fumes and organic chemical and an inlet trap (Foreline Trap for Inlet KF25 Rotary Vane Vacuum

Pumps up to 18 CFM) which serves to prevent contaminants from entering the pump inlet and protects the system from pump fluid or particulate migration. This trap extends the life of the pump, cuts maintenance costs and helps prevent system downtime. However the base system pressure remains in the range of 500 mTorr. The outlet of the pump is connected to room exhaust line through a manual valve which keep the CVD system isolated from exhaust and saves from occasional oil leak of other pumps which are also connected to exhaust. The quartz tube reactor is housed inside a horizontal single zone split tube furnace from MTI. This furnace is capable of operating at 1200 °C for prolonged hours and takes about 48 min (at 25°C/min heating rate) to reach that temperature. The temperature is controlled by Temperature Control System for Controlling MTI Furnaces with Computer - EQ-MTS02.

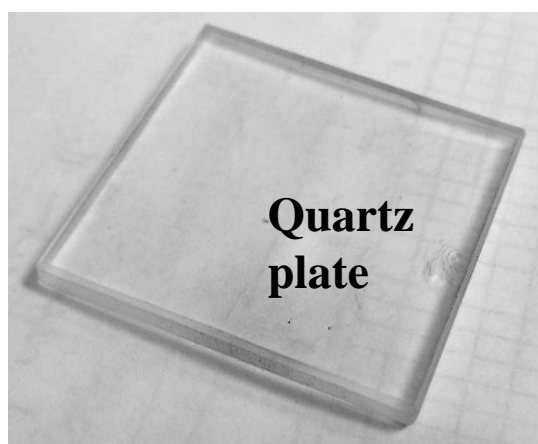


Figure 3.5. Quartz plates on which the copper/Ni foil is kept to allow graphene to grow



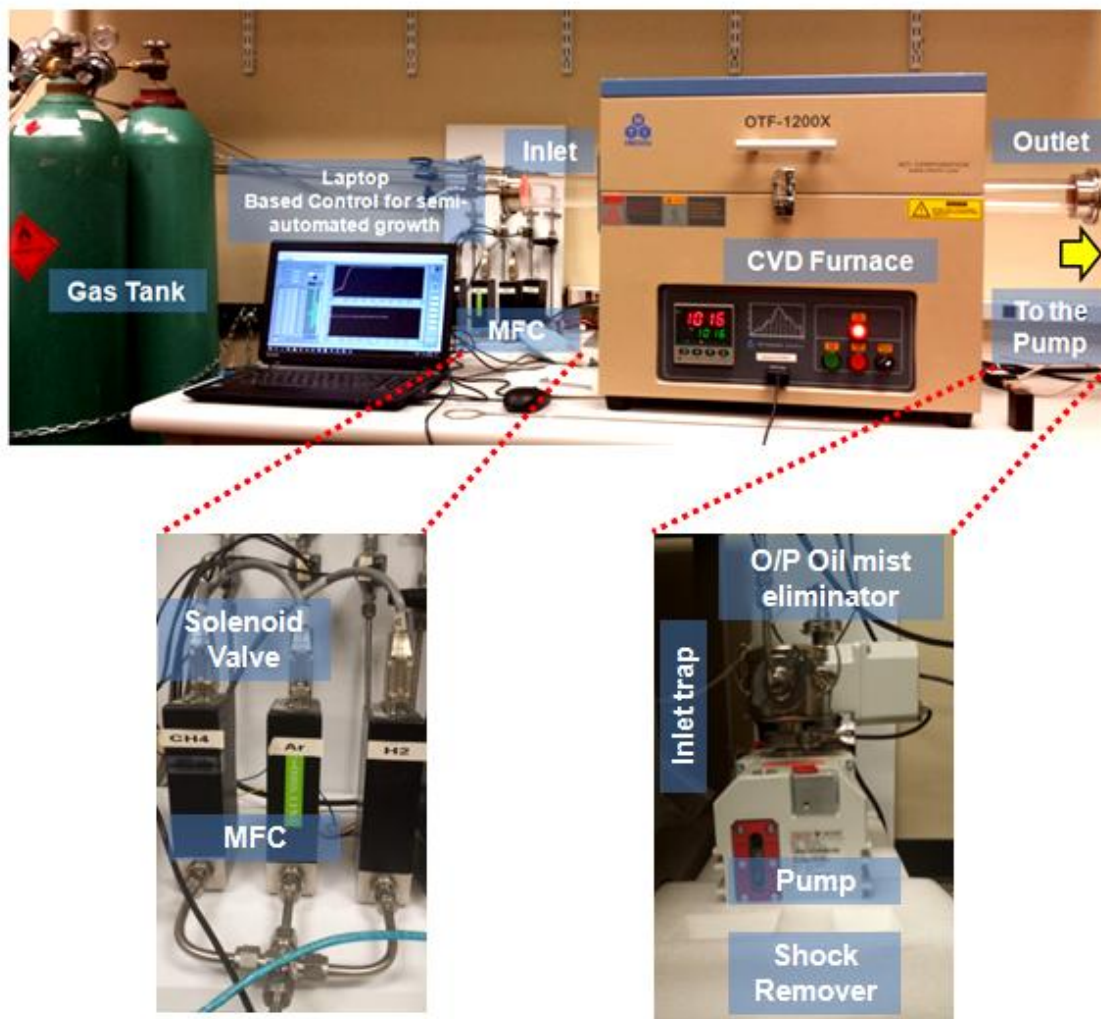


Figure 3.6. (a) CVD system (b) Mass Flow Controller for different gas (c) Pump with inlet and outlet filters

Split furnace was chosen to have a faster cooling rate to cut-down process time and it has also effect in re-crystallization of graphene of copper substrate and to suppress the precipitated carbon. Figure 3.6 shows the picture of this MTI graphene CVD system.

In summary we set up a CVD reactor to perform graphene grown on transition metal substrates like Copper. The reactor was built by assembling different components e.g. quartz tube chamber, horizontal split furnace, mechanical pump, MFCs, pressure gauges, control boxes for the automation etc.. The optimized process parameter was obtained by understanding growth mechanism and by performing series of growth under different growth conditions. The quality of growth was assessed by Raman spectroscopy on as-grown samples and also on Si/SiO<sub>2</sub> substrates after transferring. The device fabrication of CVD graphene would require the development of a reliable graphene transfer process on any desirable substrate and also of device processing techniques.

#### **3.2.4 Graphene transfer**

Since the graphene is grown on the copper substrate it must be transferred on different desired substrates for characterization and fabricating devices. Normally graphene is deposited on both sides among which the bottom layer is not of very good quality. Thus the first step is to remove this part by putting it upside down in the Reactive Ion Etching (RIE) chamber where O<sub>2</sub> plasma is used to oxidize and remove graphene layer. The copper is spin coated with PMMA at 3000 rpm for 1 minute at two steps. Then the copper is baked at 150<sup>0</sup>C for glass transition of PMMA. Then after cutting the copper sample with PMMA into desired sizes, the sample stack is kept floating (Graphene/PMMA on top) in the copper etchant solution (NH<sub>4</sub>)<sub>2</sub>S<sub>2</sub>O<sub>8</sub> (ammonium per sulfate) overnight for complete etching. Then the etchant solution becomes bluish due to Cu (II) ions. To deionize the solution, we use DI Water (Deionized water) several times

to ensure minimum amount of ions remaining in the solution. After rinsing for 5-6 times, the solution is taken away by pipette and IPA is inserted. Then the desired substrate is slid (in our case Si/SiO<sub>2</sub>, WO<sub>3</sub> etc.). After drying for long enough time, it is baked at 220°C (above the glass transition temperature of PMMA) for 5 minutes for reflowing the graphene and reducing the amount of wrinkles. Then the stack is dipped into acetone for 3-4 hours for PMMA removal. Then cleaning the acetone residue with IPA, it is dried in air.

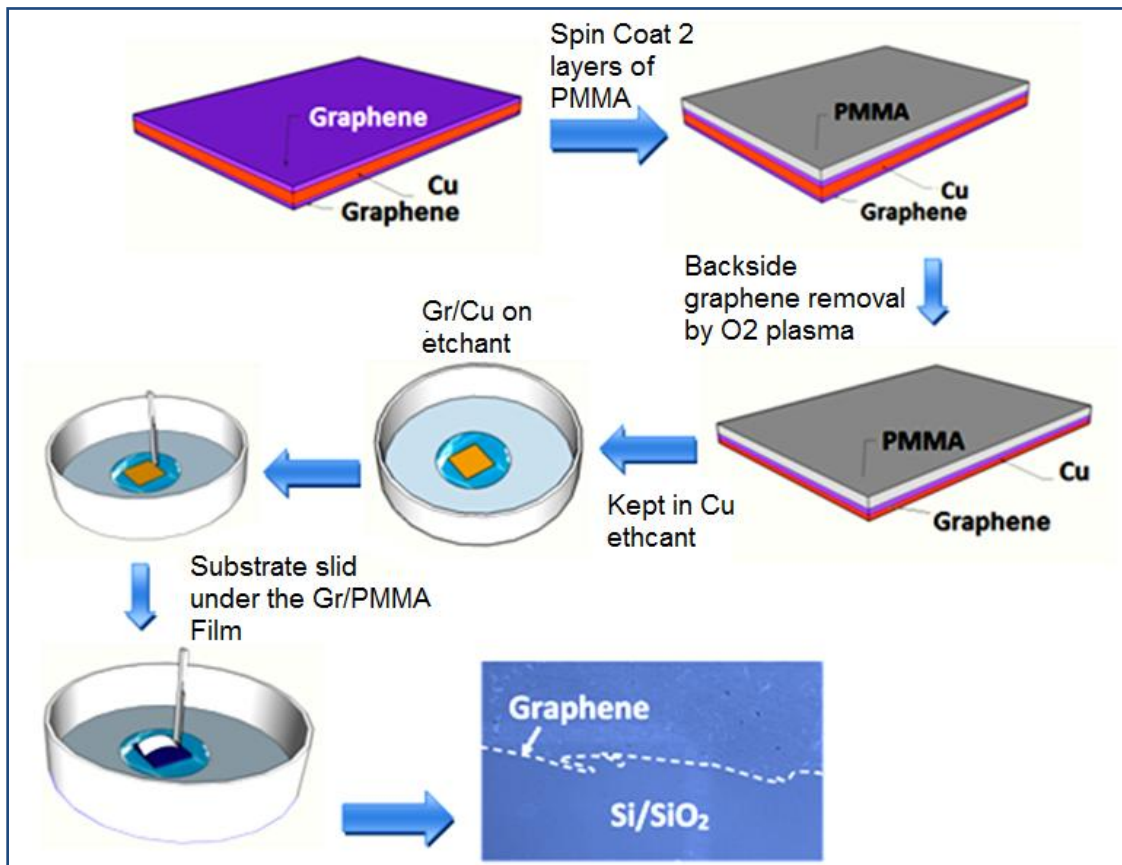


Figure 3.7. Graphene transfer steps on SiO<sub>2</sub>/Si Substrate

### **3.3. Preparation of Transition Metal oxide film**

#### **3.3.1 Film deposition**

The  $\text{In}_2\text{O}_3$ ,  $\text{WO}_3$ ,  $\text{ZnO}$  thin films were coated on  $\text{Al}_2\text{O}_3$  ceramic substrate. The films were of nominal thickness  $1\mu\text{m}$  and they were obtained commercially from Thinfilms, Inc. The films were reactively sputtered using a Material Research Corporation System, at a base pressure of  $5 \times 10^{-7}$  Torr using a transition metal target and  $\text{O}_2$  as precursor. (Nomani et al., 2012)

#### **3.3.2 Electrode deposition**

Two electrodes Ti/Ni (30 nm/150 nm) were deposited by electron beam evaporation.

### **3.4 Graphene Characterization**

There are several characterization techniques we adopted in our experiment e.g. Raman spectroscopy, atomic force microscopy (AFM), optical imaging, Hall measurement, Id-Vg characteristics of graphene FET to check the quality, thickness, electrical characteristics, surface topography, type etc.

#### **3.4.1 Optical image**

The surface and structural properties of the monolayer graphene on Cu was investigated using optical microscopy (Micromanipulator Corp. MODEL No. 6000)

### 3.4.2 Raman Spectroscopy

The quality, no of thickness and level of defects of Graphene/SiO<sub>2</sub> were characterized by Raman spectroscopy (CrystaLaser CL-2000).

### 3.4.3 Atomic Force Microscopy

Digital Instruments Dimension 3100 Atomic force microscopy was used for AFM imaging, surface roughness, and micro cracks analysis.

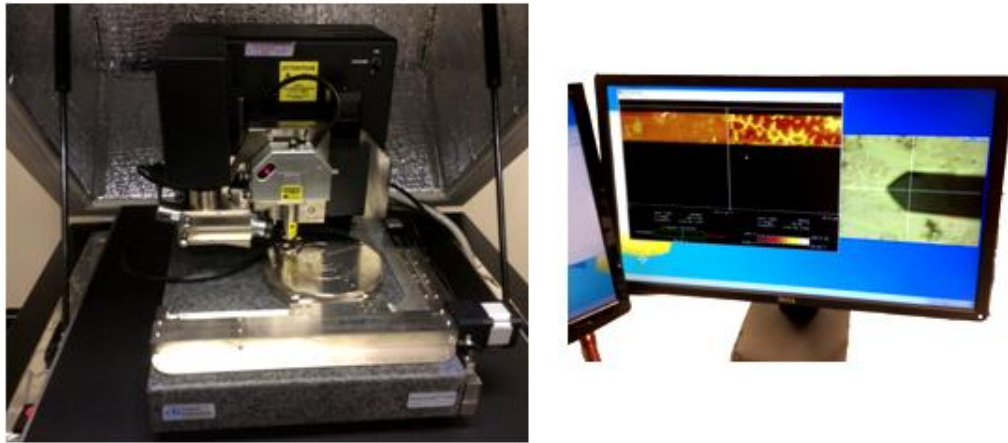


Figure 3.8. (a) Dimension 3100 Atomic force microscopy, (b) Scanning going on

### 3.4.4 Electrical Characterization

The electrical properties of graphene were measured by Hall-effect measurement Unit (Ecopia HMS3000). It uses the Van der Pauw 4-contact Hall measurement method. The magnet uses has the flux density of 0.55T. For I-V characteristics the Keysight (Formerly Agilent) B2900A Series Precision Source / Measure Units (SMU) was used.

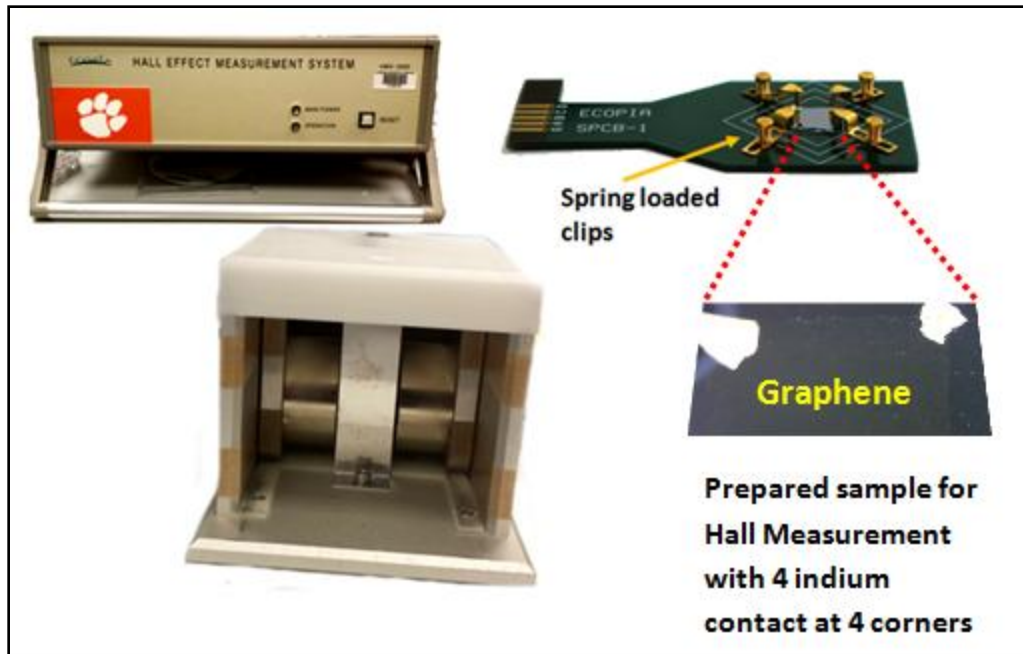


Figure 3.9. (a) Hall measurement Unit (b) PCB for sample mounting (c) Permanent Magnet (0.5 T)

### 3.5. Sensing

#### 3.5.1 Data Acquisition

We have utilized data acquisition (Agilent 34970A) which was connected with a computer for processing. Agilent 34901A 20-Channel Multiplexer was used for measuring Resistance, current, temperature etc.



Figure 3.10. (a) Agilent 34970A Data Acquisition (b) B2902A Precision Source/Measure Unit (SMU)

### 3.5.2 Mass Flow Controller (MFC)

We used GE50A General Purpose Multi-gas, Multi-range, Elastomeric-sealed Mass Flow Controller (MFC) which can be controlled by MKS MFC Web Browser, run time flow can be seen and set, and gas can also be specified.

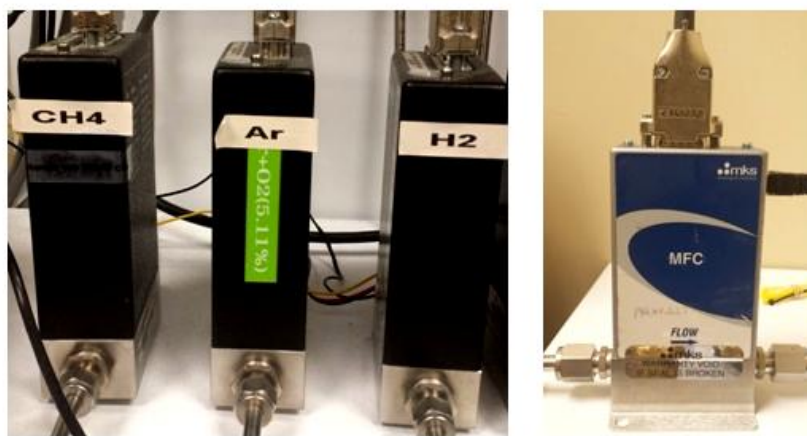


Figure 3.11. (a) MKS Instruments 1179A Analog MFC (b) GE-50A series web controlled Digital MFC



### 3.5.3 Experimental set up for sensing

We connected the gas tanks ( $\text{NO}_2$  and  $\text{NH}_3$ ) to the sample via a Mass Flow Controller (MFC) to control the flow rate of the gases. The MFC was website controlled for runtime flow set up, it was powered by MKS type 247 4-channels Readout. The Source Measure Unit (SMU) was connected to a PC for taking the sensing measurements which is controlled by Quick I-V software. The sample was biased from the SMU which could be varied arbitrarily for plotting I-V characteristics and we used to plot the resistance as a function of time while sensing. Figure 3.12 is showing the schematic of experimental set up for sensing.

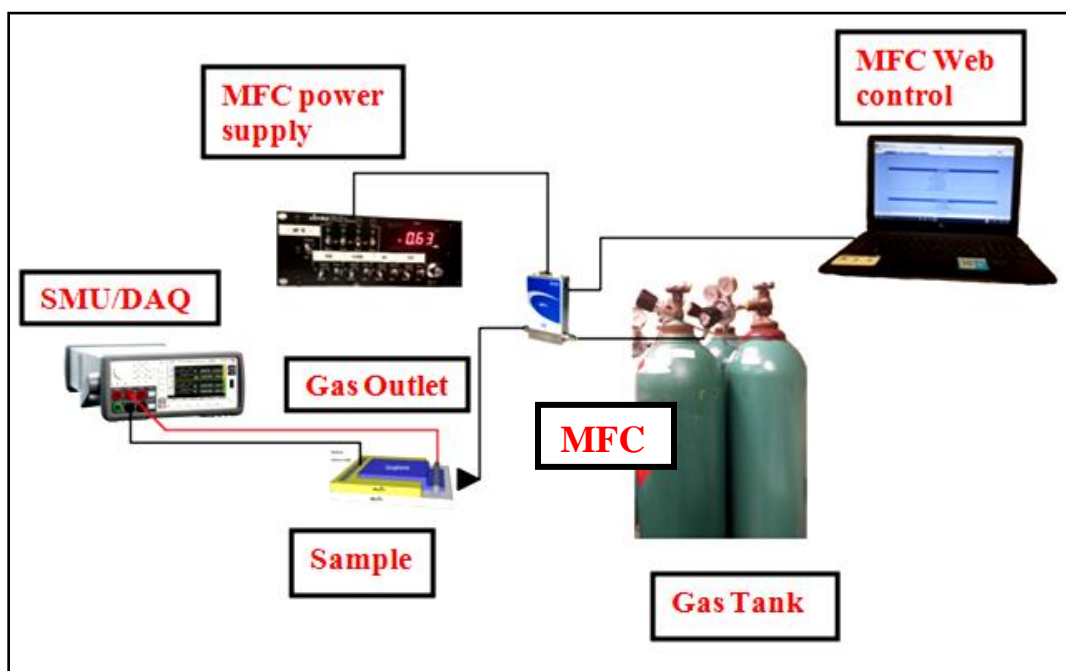


Figure 3.12. Experimental set up for gas sensing



## CHAPTER FOUR

### RESULTS AND DISCUSSION

#### **4.1 Characterization of as-grown graphene**

Graphene can be characterized by many techniques e.g. transmission electron microscopy (TEM), atomic force microscopy (AFM) and Raman spectroscopy. AFM can be used to determine the surface roughness profile and number of the layers of the graphene, and TEM images can show the structure and morphology of the graphene. However, Raman spectroscopy is a very important tool for the characterization of graphene. It is a simple tool that requires little sample preparation. Furthermore, Raman spectroscopy can not only be used to determine the number of layers, but also can identify if there are defects, and if functionalization is successful.

##### **4.1.1 Optical imaging of Graphene**

Figure 4.1a shows the optical images of the copper foil at room temperature. There are some rough groove-like features but unlike this there are some domain-like regions after being annealed (fig. 4.1b). In the last optical image the graphene flakes of annealed copper surface are shown.

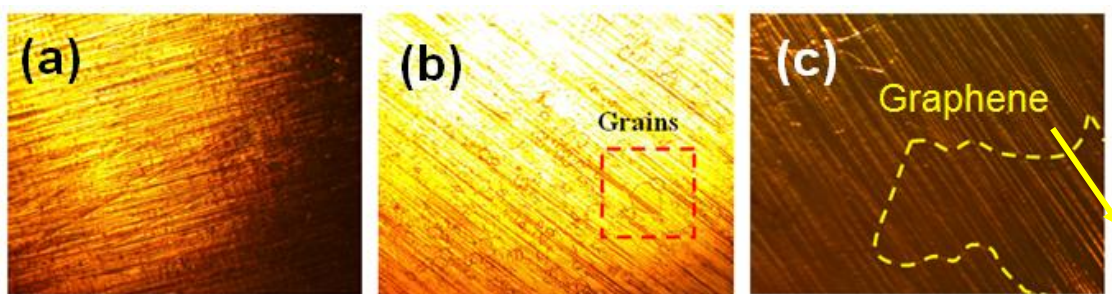


Figure 4.1. Optical images of (a) pure copper foil (b) Annealed copper at 1000°C (c) Graphene on Copper, dashed line shows the graphene boundary

The graphene/copper is on top of a quartz plate, and then the spin coater is used for coating it with PMMA. (4000 rpm for 1 minute , two layers of PMMA). Then it is baked in 150°C for 1 minute. The oxygen plasma is used for etching the back side of graphene which is normally inferior quality. It is then kept floating on Cu etchant (ammonium per sulfate solution) overnight. After 5 times rinsing with De-ionized Water (DI Water), the desired substrate is slid underneath after pouring some IPA. Then after drying for 10-15 minutes, it is baked at 220°C for 5 minutes. After that it is dipped into the acetone to remove PMMA. Figure 4.2 shows the steps for transferring as grown graphene to SiO<sub>2</sub>/Si substrate while Figure 4.3a. shows the optical image of graphene transferred on SiO<sub>2</sub>/Si (300 nm) and fig. 4.3b is an optical microscopic image.

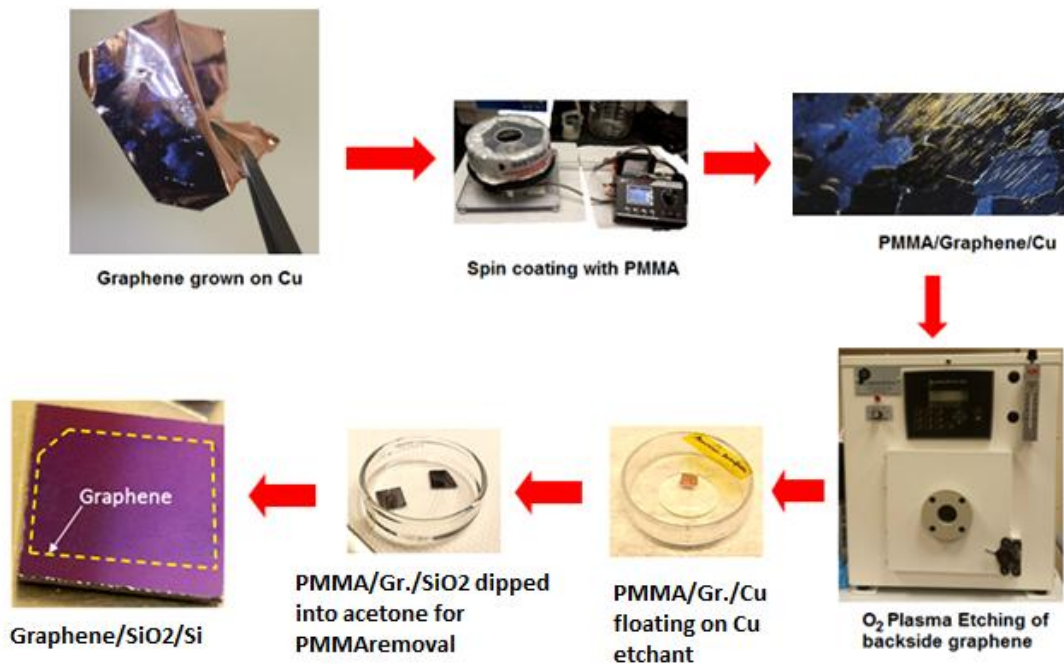


Figure 4.2. Steps growing the transferring of as grown graphene on copper to SiO<sub>2</sub>/Si substrate

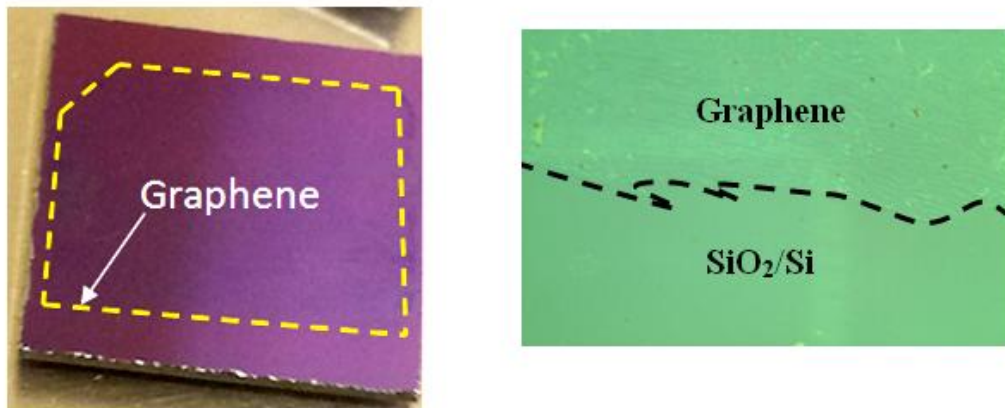


Figure 4.3. (a,b) Optical images of Graphene transferred on SiO<sub>2</sub>/Si Hall mobility, the dashed line shows the boundary of graphene.

#### 4.1.2. Hall Measurement

It is a method of determining transport properties of a material such as resistivity ( $\rho$ ), carrier density ( $N_b$ ), sheet resistance ( $R_S$ ), hall coefficient ( $R_H$ ) and mobility ( $\mu$ ). It is based upon Hall Effect in which a magnetic field is applied perpendicular to a slab of material which carries a current across it.

Table 4.1 shows the Hall measurement of graphene transferred on SiO<sub>2</sub>/Si. HMS-3000 Hall Measurement system was used for measuring the resistivity, carrier concentration, mobility of graphene on SiO<sub>2</sub>/Si substrate. From the table below, the measured Hall mobility is reasonably high which is also an indicator for good quality and less defective graphene film.

Table 4.1 Hall measurement of graphene transferred on SiO<sub>2</sub>/Si

$N_b$ (cm <sup>-3</sup> )	$\mu$ (cm <sup>2</sup> /v-s)	$\rho$ ( $\Omega$ -cm)	$R_H$ (m <sup>2</sup> /C)	$N_S$ (/cm <sup>2</sup> )	$R_S$ ( $\Omega$ )
1.82 $\times 10^{16}$	3126	1.18 $\times 10^{-1}$	3.43 $\times 10^2$	9.09 $\times 10^{11}$	2.36 $\times 10^3$

Table 4.2 shows the statistical data (e.g. mean, median, standard deviation etc.) of the measured Hall mobility of the same sample at various locations. Figure 4.4 shows that each of them is different because of varying layer thickness (size and shape) and disorder. It could be due to the non uniform growth of graphene on copper or could also be attributed to the transfer of the film. There are always some wrinkles and folds which may contribute to the mobility change at different locations. The orientation of

the copper substrate along the gas flow also plays important factor with regards to uniformity

Table 4.2 Statistical data of hall mobility of different samples at different locations

No	Mean	Median	Min	Max	Std	RMS
7	1608.01	1892	580.8	2844	994.717	1853.06
18	923.713	938	381	1222	196.946	943.106

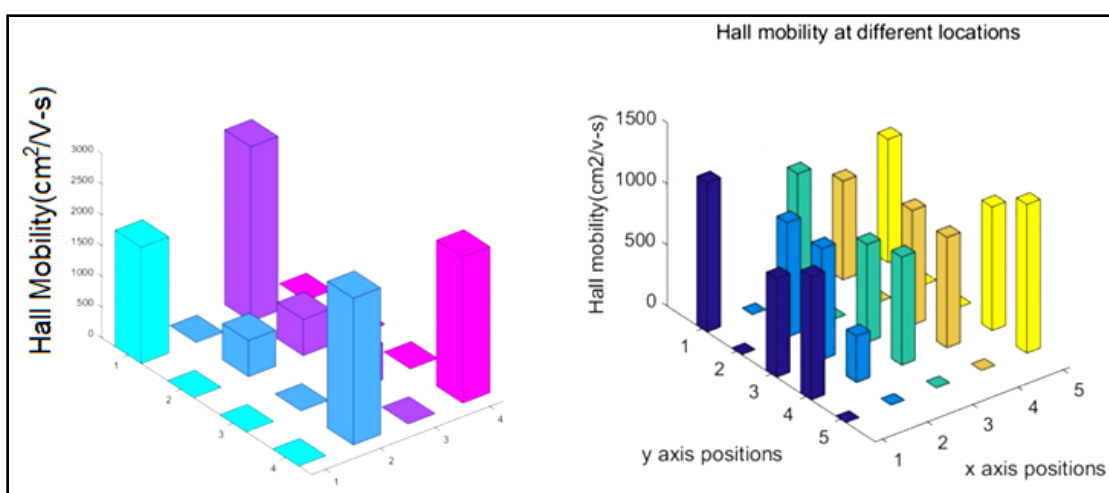


Figure 4.4. Hall mobility of different location of same sample (a) sample # 190 (b) sample # 191

Figure 4.5 suggests hall mobility numbers for our few grown samples. The best mobility is approximately  $4301 \text{ cm}^2\text{V}^{-1}\text{s}^{-1}$ . The variation could be due to the degradation of the growth condition like carbon absorption in the quartz tube, vaporization of copper for a long while, degradation of the thermocouple giving rise to

lack of tuning the optimum temperature, leak of the vacuum system, copper surface quality, pressure variation etc. We noticed that after the tube cleaning the mobility improves which indicates the correlation of the copper vapor pressure and improper dehydrogenation of  $\text{CH}_4$  in the growth mechanism.

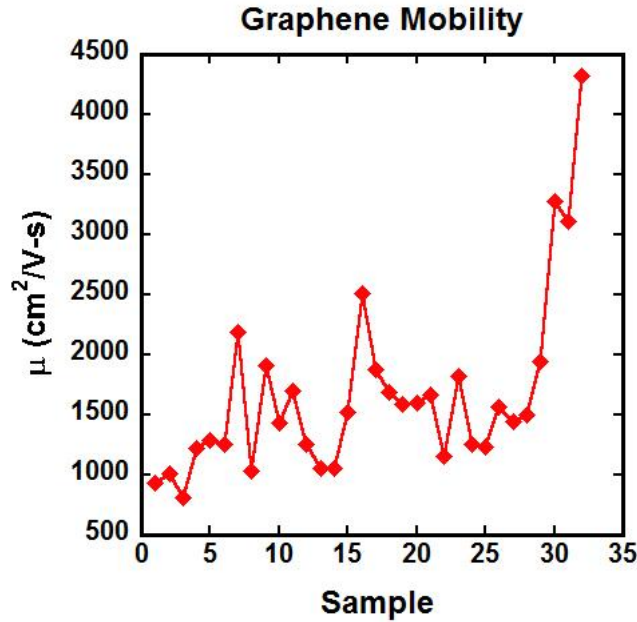


Figure 4.5. Hall data from different growth

#### 4.1.3 Atomic Force Microscopy (AFM) images

AFM shows several parameters: Amplitude, Statistical and Spatial parameters to describe the surface topography. Even by line profile, 3D and 2D image profile and Histogram analysis, we can explain sizes and counting rate of the domains of the materials and surface morphology. Depth profile of the multilayer films can also be measured by AFM technique. Amplitude image takes best height image for better

topography. Amplitude image shows how the tip deflected as it encountered sample surface. Images are similar to topography showing the map of the slope of the sample. Using other words, amplitude image is the image of error signal of AFM. Phase Imaging give possibility to find region of different properties: e.g. giving opportunity to clearly visualize grains and boundaries

Figure 4.6a shows the height profile while fig. 4.6b shows the phase imaging of a graphene sample on  $\text{SiO}_2/\text{Si}$  substrate. As seen from the plots; the phase plot clearly shows the boundaries. Figure 4.6c shows the height profile along a designated line which is limited to 3 nm.

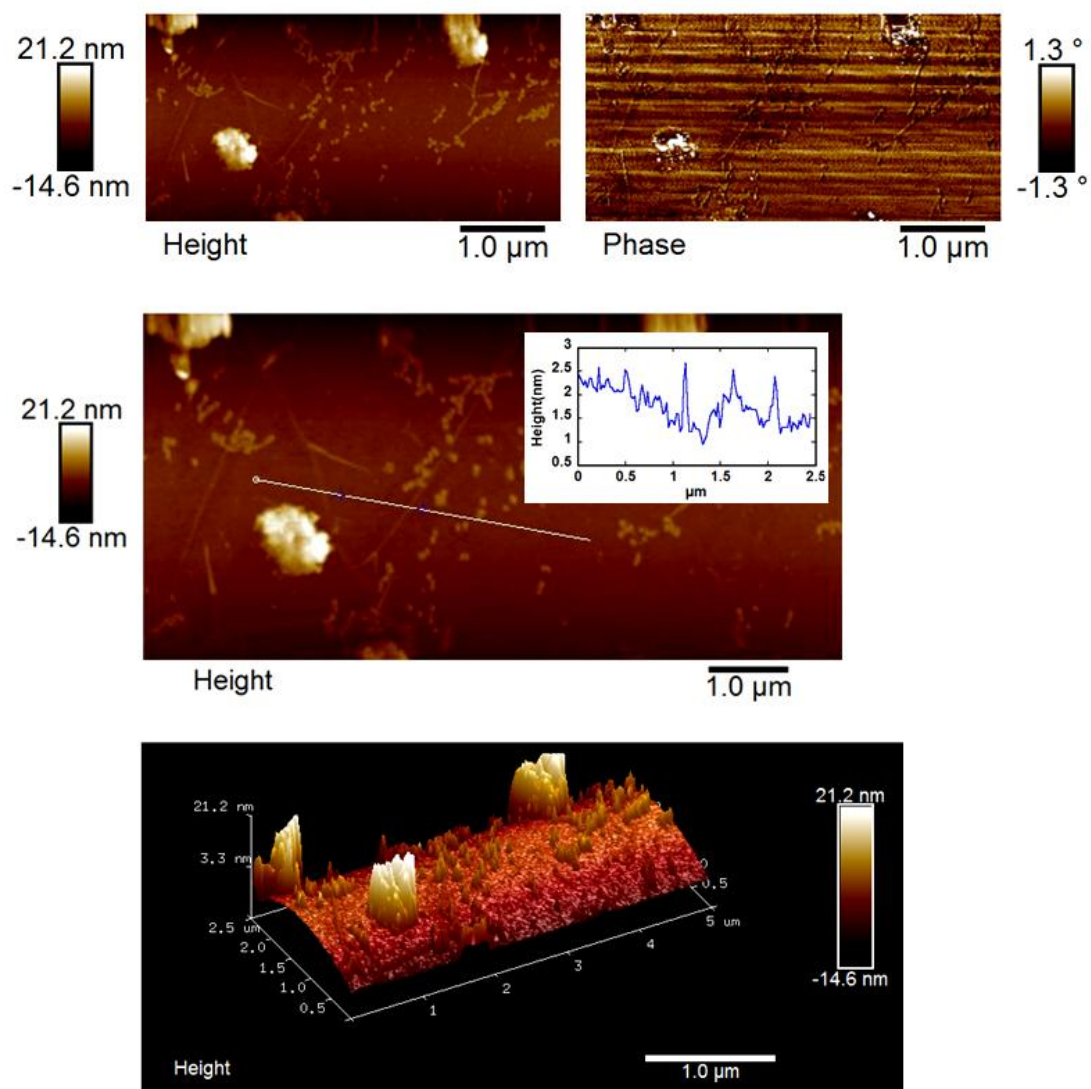


Figure 4.6. (top left) Height profile (top right) Phase imaging (middle) Cross-section along the line indicated of graphene transferred on SiO<sub>2</sub>/Si (bottom) 3D topography of graphene on SiO<sub>2</sub>/Si showing possible acetone residue and wrinkles.

#### 4.1.3 Raman Spectroscopy



Figure 4.7a shows the Raman spectrum of graphene transferred on SiO<sub>2</sub>/Si. As indicated by I<sub>D</sub>/I<sub>G</sub> value of 0.13, the sample has lower defect density. The I<sub>2D</sub>/I<sub>G</sub> value of 2.1 along with 2D FWHM of 26.4 cm<sup>-1</sup> indicates the presence of SLG. The Raman spectra of WO<sub>3</sub> exhibited vibrations in three region at 900–600, 400–200, and below 200 cm<sup>-1</sup>, which correspond to the stretching, deformation and lattice modes, respectively. The Raman bands observed for as-grown WO<sub>3</sub> sample at 270, 327, 427, 701, 807 and 950 cm<sup>-1</sup> (Fig. 4.27b) were identified as the four strongest modes of monoclinic tungsten oxide. The Raman bands at 270 and 327 cm<sup>-1</sup> correspond to O–W–O bending modes of the bridging oxygen and bands at 715 and 807 cm<sup>-1</sup> are due to the stretching modes.

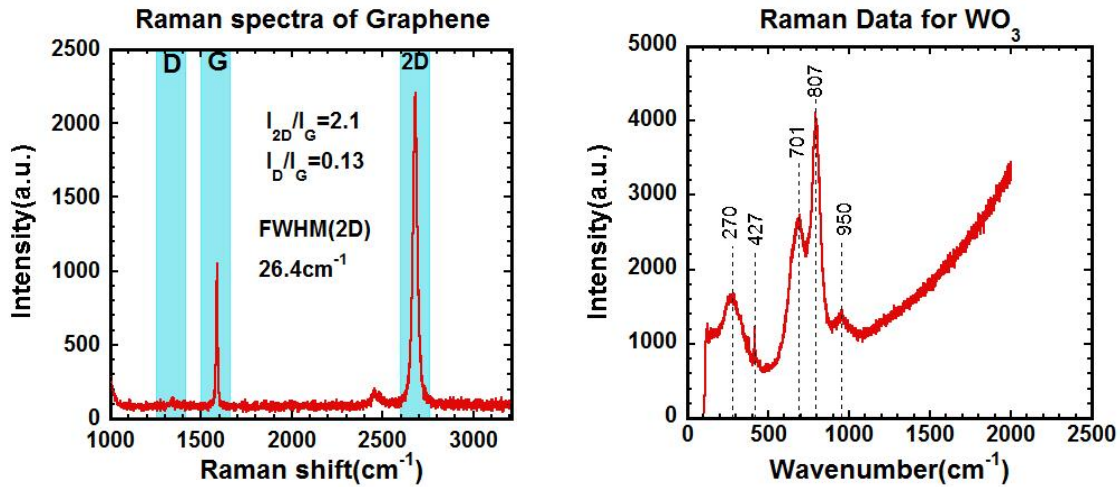


Figure 4.7. Raman spectra of (a) graphene transferred on SiO<sub>2</sub>/Si substrate (b) WO<sub>3</sub> on Al<sub>2</sub>O<sub>3</sub> ceramic substrate

Figure 4.7 shows Raman data from different sample which shows some defects along with FLG present in them because of the  $\frac{I_D}{I_G}$  and  $\frac{I_{2D}}{I_G}$  ratio. D peak is also much more visible than before indicating presence of defects.

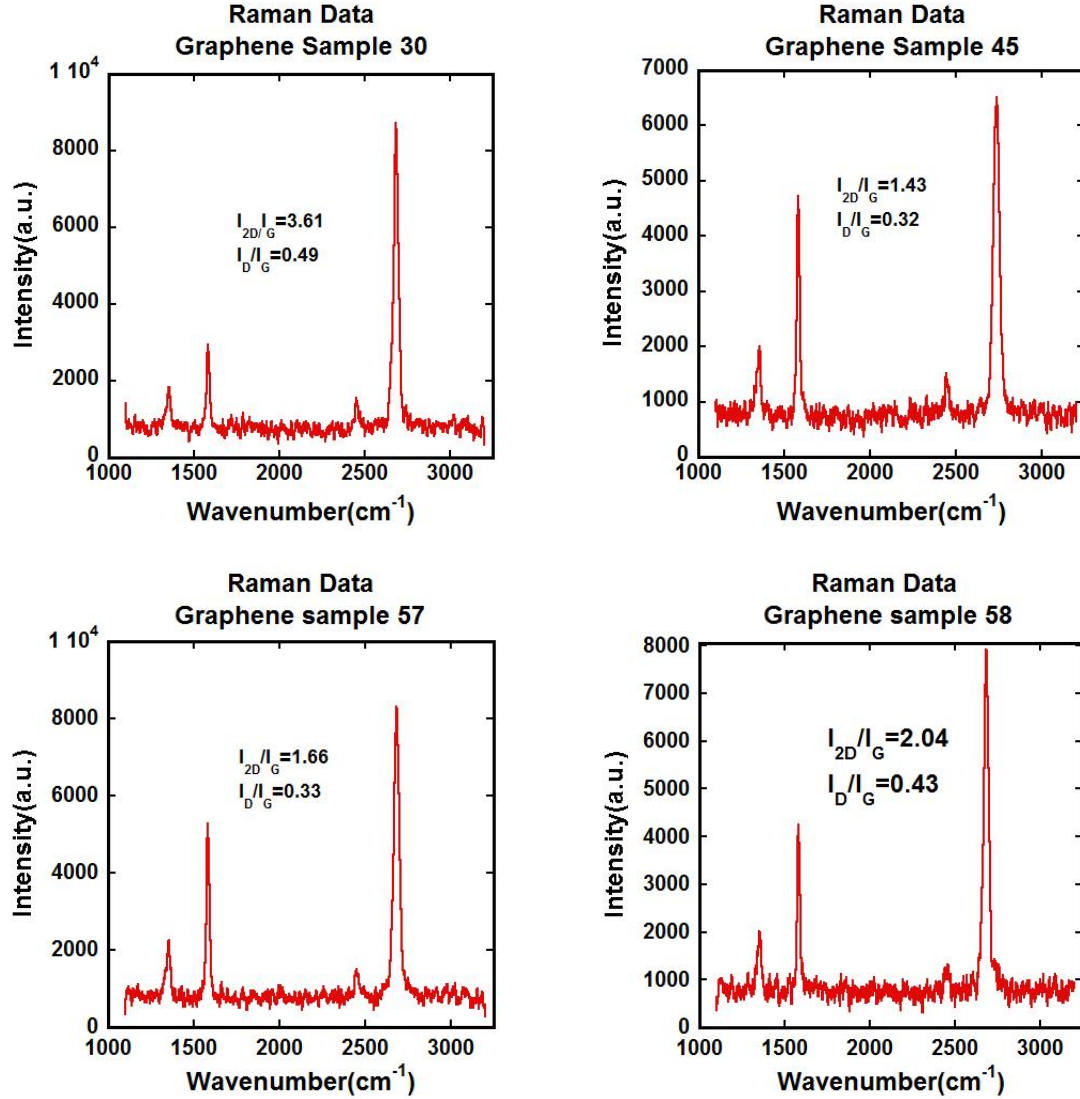


Figure 4.8. Raman Spectroscopy of different samples

There are mainly two different methods for calculating number of layers. The second method uses the following formula according to which the number of layers is slightly more than 2 (given G-band position is 1584):

$$\omega_G = 1581.6 + \frac{11}{1 + n^{1.6}} \quad (4.6)$$

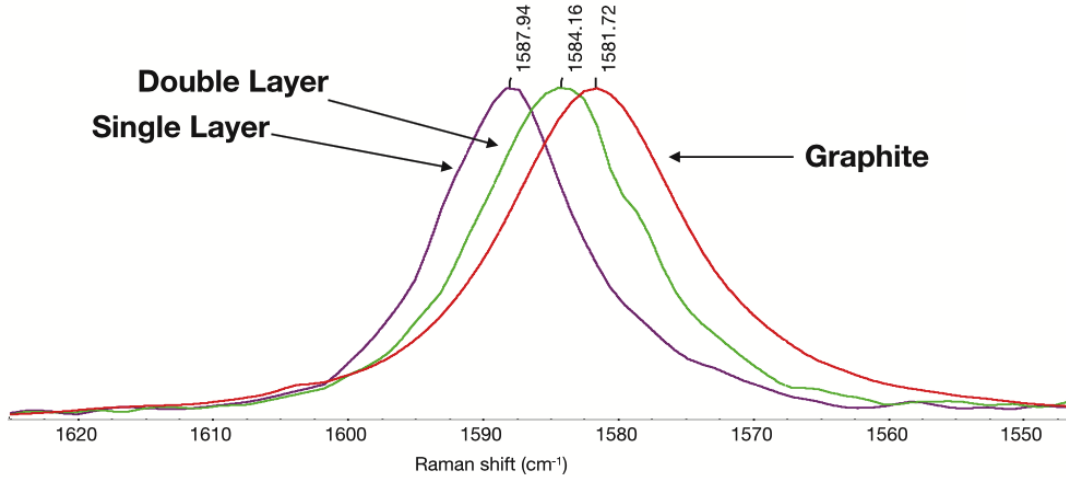


Figure 4.9. G-band position indicating number of layers.

## 4.2 Graphene Semiconductor Schottky Junctions

### 4.2.1 Schottky Junction Overview

The studies of the past few years have demonstrated that graphene can form junctions with semiconducting materials. It has rectifying characteristics and behaves as excellent Schottky diodes. The main originality of these devices is the tunable Schottky barrier height, a feature which makes the graphene/semiconductor junction a great platform for the study of interface transport mechanisms as well as for

applications in photo-detection, high-speed communications, solar cells, chemical and biological sensing, etc. The contact between metal and semiconductor can result in two types of contact-one is called Ohmic contact (follows Ohm's law) and other is called Schottky junction (rectifying behavior like diode) (Di Bartolomeo, 2016) . Ohmic junctions are normally formed in heavily doped semiconductors while Schottky contact is formed with lightly doped semiconductors. For ideal Ohmic contact the current (I) varies linearly with applied voltage (V):

$$\frac{V}{I} = R_c + R_s \quad (4.2)$$

Where  $R_s$  is the lumped resistance between metal and semiconductor and  $R_c$  is the contact resistance. The lower the contact resistance the better Ohmic contact it is. To the contrary the ideal Schottky junction follows the diode behavior (i.e. low resistance in the forward voltage and high resistance in the reverse portion). Schottky junctions are normally formed in lightly doped semiconductors. In this section we will go through some of the key concepts of Schottky junction which will be later for Graphene Schottky Junction.

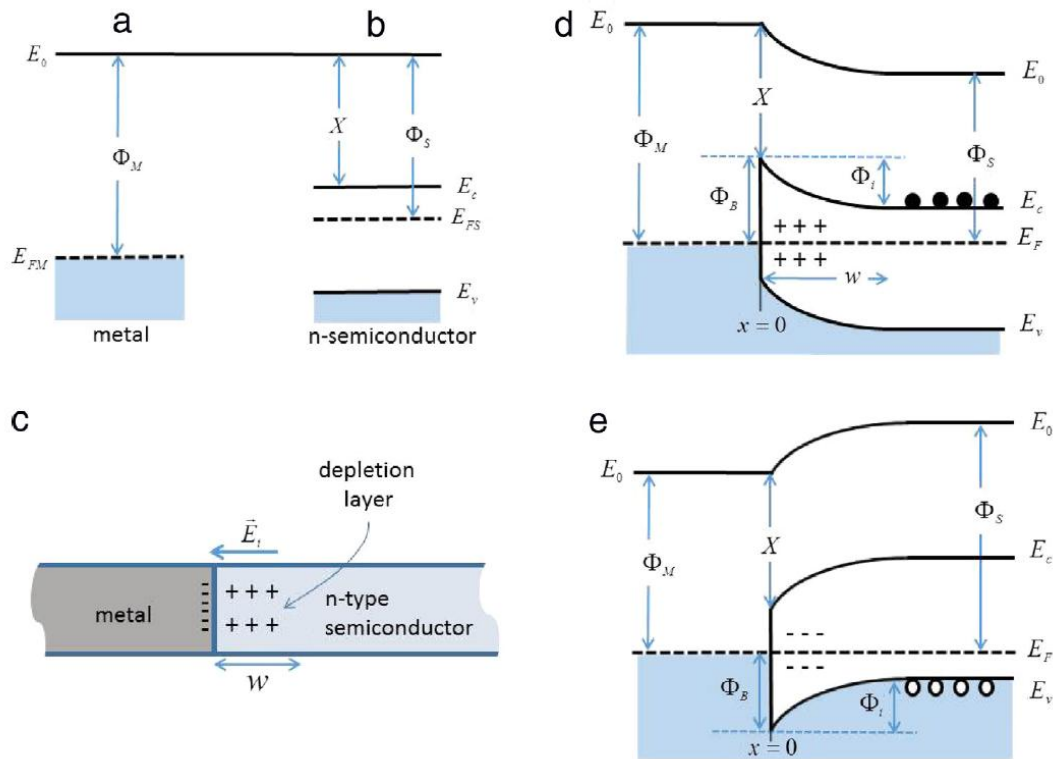


Figure 4.10. Metal Semiconductor Schottky junction formation (a,b) energy band diagram before contact (c) schematic showing depletion region after charge transferring taking place (d,e) Schottky junction formation in n and p-type semiconductor (Di Bartolomeo, 2016)

The difference between the vacuum level  $E_0$  and Fermi level  $E_F$  is called the work function  $\phi$ ,

$$\phi = E_0 - E_F \quad (4.3)$$

As the  $E_F$  varies due to doping concentration and temperature, the parameter to define semiconductor is called electron affinity  $\chi$  which is the difference between conduction band edge,  $E_c$  and Vacuum level  $E_o$ .

$$\chi = E_o - E_c \quad (4.4)$$

When a pair of metal semiconductor comes close together charge transfer takes place until  $E_F$  reaches the equilibrium. This charge transfer gives rise to formation of space charge called depletion layer in the semiconductor side. The contact between a metal and a n-type semiconductor with  $\phi_M < \phi_S$  should result in electron injection from the metal to the semiconductor. No depletion layer will be formed in this case, since the metal can be considered an infinite electron reservoir, and the junction would be Ohmic. When a depletion region is formed, there is opposite thin layer of mirror charge in metal side which acts as a parallel plate capacitor and thus created an Electric field and a built-in potential  $\phi_i$  which prevents electron from going to the metal from semiconductor.

$$\phi_i = \phi_M - \phi_S \quad (4.5)$$

The most important parameter is Schottky barrier height. There is a discontinuity after the  $E_F$  reaches equilibrium which is not bias dependent unlike the built-in potential which can be altered by applying bias. Schottky barrier height  $\phi_B$  can be related to the metal work-function and to the semiconductor affinity of electron by the following equation:

$$\phi_B = |\phi_M - \chi| \quad (4.6)$$

The barrier height cannot be changed by biasing or doping as both the parameters are material's intrinsic property. So it can be altered by the choice of materials. The larger the barrier height, the better diode characteristics it has. (Donoval et al., 1991)

### **Thermionic emission and I-V characteristics**

The current mechanism of a Schottky barrier is not like typical p-n junction. It is basically due to the majority carrier. When the semiconductors are moderately doped, the thermally excited electrons jump over the built in potential from semiconductor to metal which is the dominant transport mechanism in Schottky junction. There are other conduction mechanisms which involve the tunneling through barrier called the Thermionic Field emission (TFE) and Field Emission (FE). Generation and recombination in the depletion region, injection of holes from metal side into the semiconductor, edge leakage current, interface current due to traps are also few other mechanism of conduction in Schottky barrier junction. How much one conduction mechanism will contribute is a function of doping concentration and temperature by the following equation: (Kwak et al., 2014)

$$E_{00} = \frac{eh}{4\pi} \sqrt{\frac{N}{\epsilon_s m^*}} \quad (4.7)$$

If the following inequality is satisfied the dominant mechanisms will be categorized as TE, TFE or FE respectively.

$$\frac{E_{00}}{kT} \leq 0.2$$

$$0.2 < \frac{E_{00}}{kT} \leq 5$$

$$\frac{E_{00}}{kT} > 5$$

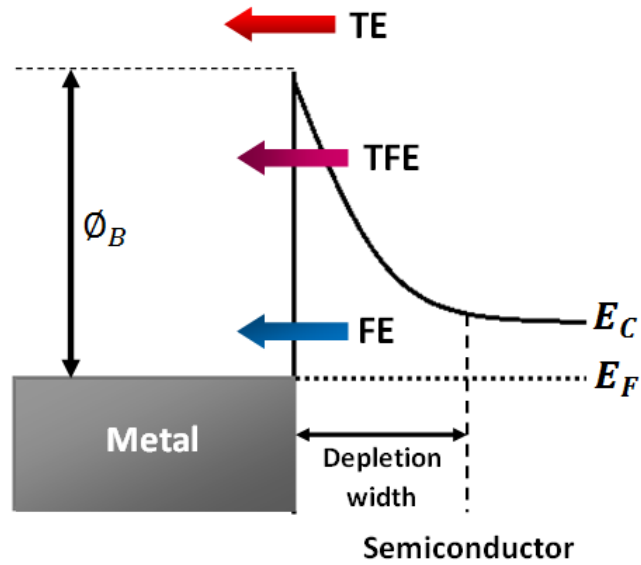


Figure 4.11. Principal transport processes across an M/S Schottky junction: TE = thermionic emission, TFE = thermionic field emission, FE = field emission

The current  $I(S \rightarrow M)$  due to electrons flowing from the semiconductor to the metal is obtained by the following equation:



$$I_{S \rightarrow M} = A \frac{4\pi e m^* k^2}{h^3} T^2 e^{-\frac{\phi_B - eV}{kT}} \quad (4.8)$$

From the relation it can be clearly seen that this current is exponentially dependent on the applied voltage and also on SBH.

At zero voltage, there should be no current at all. So we can write

$$I_{S \rightarrow M} + I_{M \rightarrow S} = 0 \quad (4.9)$$

$$\begin{aligned} I_{S \rightarrow M} &= -I_{M \rightarrow S} = A \frac{4\pi e m^* k^2}{h^3} T^2 e^{-\frac{\phi_B}{kT}} \\ &= AA^* T^2 e^{-\frac{\phi_B}{kT}} \end{aligned} \quad (4.10)$$

$$A^* = \frac{4\pi e m^* k^2}{h^3} \quad (4.11)$$

$A^*$  is known as the Richardson constant. It is dependent of the semiconductor, metal, and inhomogeneity of SBH, interfacial layers, and quantum tunneling of carriers (Cheung and Cheung, 1986).

The bias voltage cannot alter the Fermi level of the metal, so  $\phi_B$  is constant even under the application of bias voltage. So the total current after applying bias voltage is,

$$I = I_{S \rightarrow M} + I_{M \rightarrow S} = I_0 (e^{\frac{eV}{kT}} - 1) \quad (7)$$

Where

$$I_0 = AA^*T^2 e^{-\frac{\phi_B}{kT}} \quad (4.13)$$

$I_0$  is the reverse saturation current. The lower  $I_0$  the better Schottky diode is. It is strongly dependent on the temperature and specially SBH change.

These discussions are showing the ideal behaviors. Sometimes we see some non-ideal effects. So an ideality factor,  $n$  is inserted in the exponential term along with a series resistance which is the lump resistance of metal, semiconductor and the contact. Including all of these, the equation becomes the following:

$$I = I_0 \left[ e^{\frac{e(V-R_S I)}{nkT}} - 1 \right] \quad (4.14)$$

Because the effective voltage is lowered due to the series resistance,  $R_S$  (Norde, 1979)

$$V_{eff} = V - R_S I \quad (4.15)$$

The ideality factor is a measure of deviation from the thermionic emission and shows the contribution of defects and other non-thermionic effects that alters the ideal behavior. It was mentioned earlier that non thermionic effects include thermionic field emission, field emission, generation/recombination, image-force barrier lowering, Schottky barrier in-homogeneity, bias dependence of SBH, edge leakage and so on.

#### 4.2.2 Measurements of ideality factor, Schottky barrier and series resistance

When the current  $I$  is plotted in semi-logarithm scale, the  $I$ - $V$  characteristic in forward bias (and for  $V > kT/e$  and  $V \gg R_s I$ ) corresponds to the straight line,

$$\ln I = \ln I_0 + \frac{e}{nkT} V \quad (4.16)$$

For  $V \rightarrow 0$  the linearity of the semi log plot is lost. However according to the equation involving  $R_s$  gives a straight line all the way to  $V=0$  by plotting  $1/(a \exp(-eV/kT))$  vs.  $V$

$$\ln \frac{I}{1 - e^{-\frac{eV}{kT}}} = \ln I_0 + \frac{e}{nkT} V \quad (4.17)$$

In both cases the y axis intercept and slope gives  $I_0$  and  $n$  respectively.

There is another plot called Richardson Plot ( $\ln (I_0/T^2)$  vs.  $a/T$ ) whose slope and y axis intercept allows the determination of gives  $\phi_B$  and  $A^*$

$$\ln \frac{I_0}{T^2} = \ln(AA^*) - \frac{\phi_B}{k} \frac{1}{T} \quad (4.18)$$

Even the series resistance can be evaluated from the following equation:  
(Cheung and Cheung, 1986)

$$\frac{dV}{d(\ln I)} = \frac{nkT}{e} + R_s I \quad (4.19)$$

Series resistance  $R_s$  is an important parameter that influences the electrical characteristics of Schottky diodes so we used Cheung method as an efficient method to evaluate  $n$ , and  $R_s$ . The forward bias current-voltage characteristics due to thermionic emission of a Schottky barrier diode with series resistance can be expressed as Cheung's functions:

$$H(I) = V + n \frac{kT}{q} \ln \left( \frac{I}{AA^* T^2} \right) \quad (4.20)$$

$$H(I) = n\phi_b + IR_s \quad (4.21)$$

### 4.3 Determination of Electrical Parameters in $\text{In}_2\text{O}_3$ /Graphene heterojunction

The  $\text{In}_2\text{O}_3$  film is deposited on  $\text{Al}_2\text{O}_3$  ceramic substrate. After etching one part the graphene is transferred on top of the structure (Fig. 4.12a). Closer to the step, the heterojunction exists. Then after the e-beam metal electrode deposition, the bias is applied from Source/Measure Unit (SMU) and I-V characteristic curve is plotted. Electrical characterization of the graphene/ $\text{In}_2\text{O}_3$  heterojunction showed Schottky type current-voltage (I-V) characteristics. A voltage bias was applied to the  $\text{In}_2\text{O}_3$  contact and the graphene contact was kept as ground. Representative I-V characteristics for

graphene/ $\text{In}_2\text{O}_3$  heterojunction Schottky diodes are shown in Fig. 4.13b. The diode current increases exponentially with voltage initially, before being dominated by series resistance indicating that graphene forms Schottky contact with n-type  $\text{In}_2\text{O}_3$ .

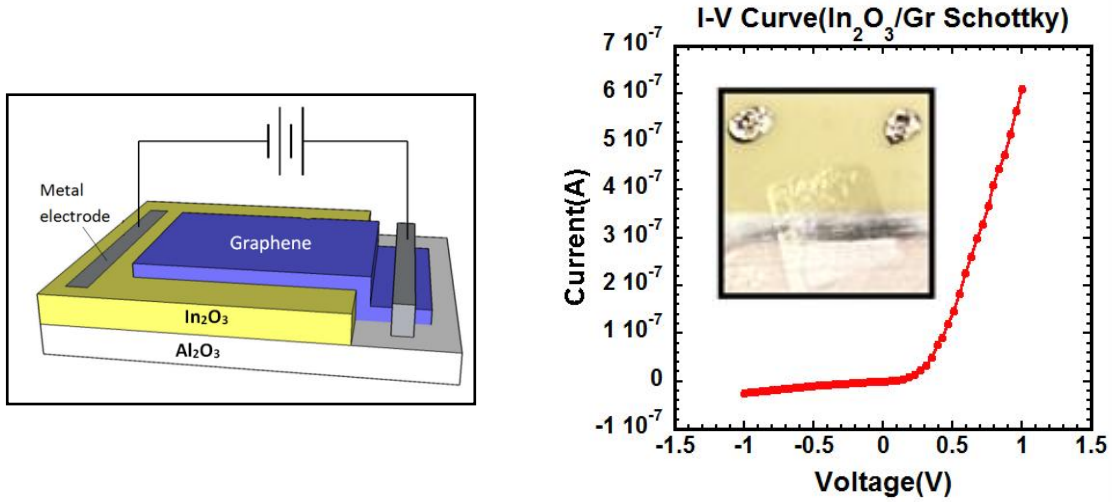


Figure 4.12. (a) Device structure of  $\text{In}_2\text{O}_3$ /Graphene Heterojunction diode (b) I-V characteristics of Graphene/ $\text{In}_2\text{O}_3$  Schottky junction at the temperature of 301K (Inset shows the optical image of fabricated device)

#### 4.3.1 Schottky Formation Mechanism in $\text{In}_2\text{O}_3$ (and $\text{WO}_3$ ) / Graphene Junction

As we can see from fig. 4.13 the work function of the semiconductor is greater than graphene which is usually not the condition for Schottky junction formation. But there are interfacial trap centers readily forming in the interface. As a result electrons are transferred from graphene to the metal oxide and the Fermi level of graphene and metal oxide are going down and upwards respectively until the equilibrium takes place between graphene and metal oxide Fermi level. After that electrons flow from the metal oxide conduction band to the newly formed Fermi level of graphene and gets

depleted of electrons. As a result the energy band bends up and forms Schottky. This argument is true for both  $\text{WO}_3$  and  $\text{In}_2\text{O}_3$ /Graphene Schottky Junction.

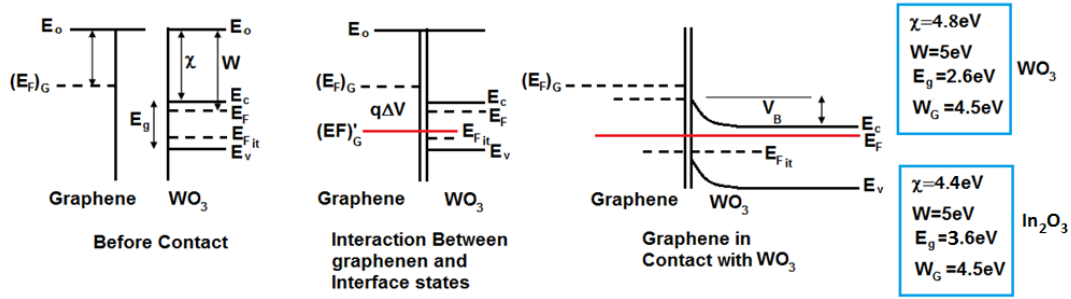


Figure 4.13. Schematic of Schottky formation mechanism in  $\text{In}_2\text{O}_3$  (and  $\text{WO}_3$ )/Graphene Junction

#### 4.3.2 Method-1: Ideal Thermionic Emission Model

For a Schottky barrier diode with assumption that the current is due to thermionic emission, the electrical parameters can be determined from equation (18-21) Fig. 4.14 shows the experimental I-V (semi log) and  $\ln(I)$ -V characteristics of our Graphene/ $\text{In}_2\text{O}_3$  diode at the temperature of 301K. Since the current curve in forward bias quickly becomes dominated by series resistance and deviates from linearity we used the low forward bias part of I-V characteristics to measure  $n$ ,  $\phi_B$ .

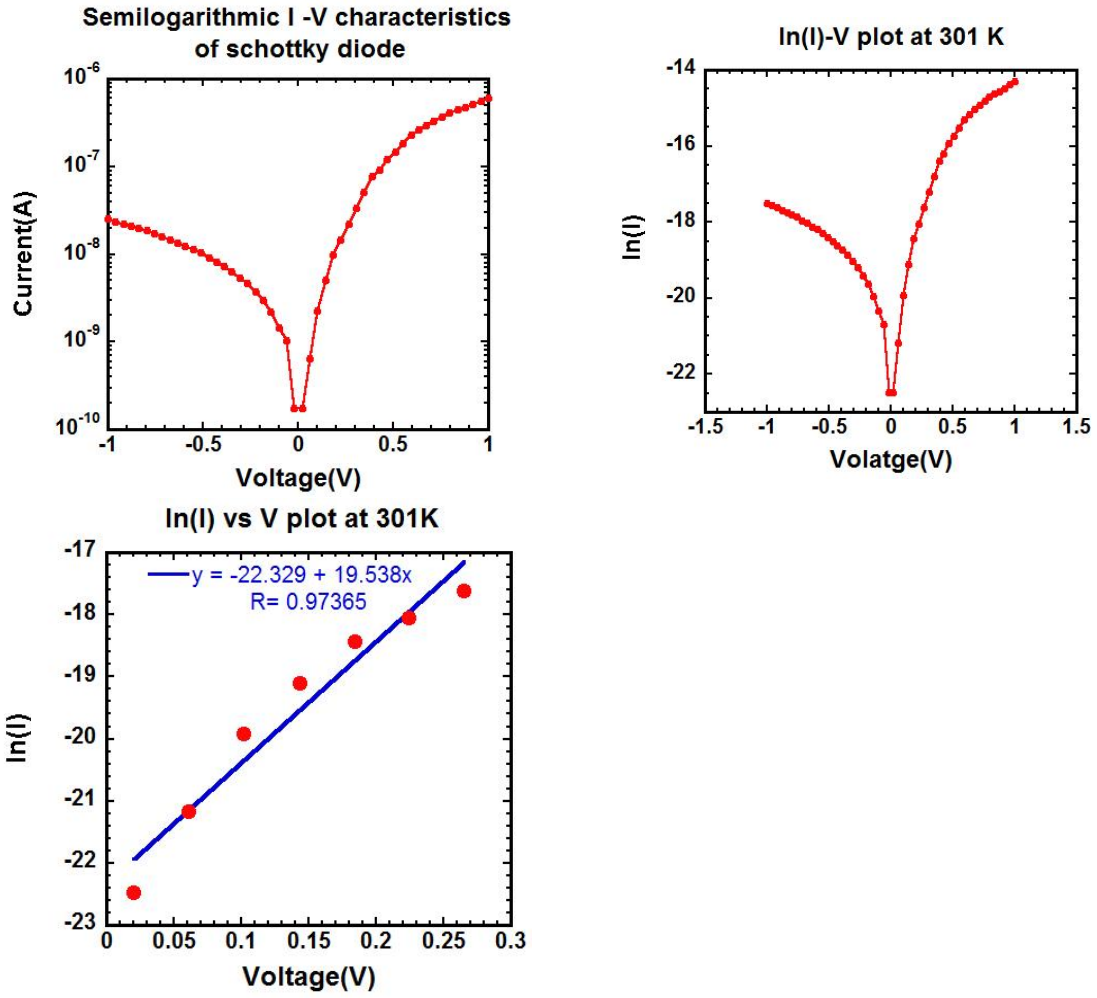


Figure 4.14. (a) I-V characteristics (semi log scale) (b) lnI-V plot (c) Linear Curve Fit of Graphene/In<sub>2</sub>O<sub>3</sub> Schottky junction at the temperature of 301K

According to equation (20) after performing least square fitting on the lnI-V plot in the linear region of experimental data as in Fig. 4.16, we determined the value of  $n$ ,  $I_0$  from the slope and the y axis intercept of the fitted straight line.

Table 4.3 Ideality factor, reverse saturation current and SBH

Electrical parameters
$n = 1.9733$ $I_0 = 2.0074 \times 10^{-10} A$ $\phi_B = 0.9321 eV$

#### 4.3.3 Calculation of Richardson constant from Arrhenius Plot

Figure 4.15 shows the Arrhenius plot ( $\log [I_0/T^2]$  vs.  $1000/T$ ) for the barrier height estimate. A small reverse bias was applied to minimize the image force barrier lowering effect. The barrier heights  $\phi_B$  (the slopes of the plot) are extracted for each junction. They are given in table 4.4

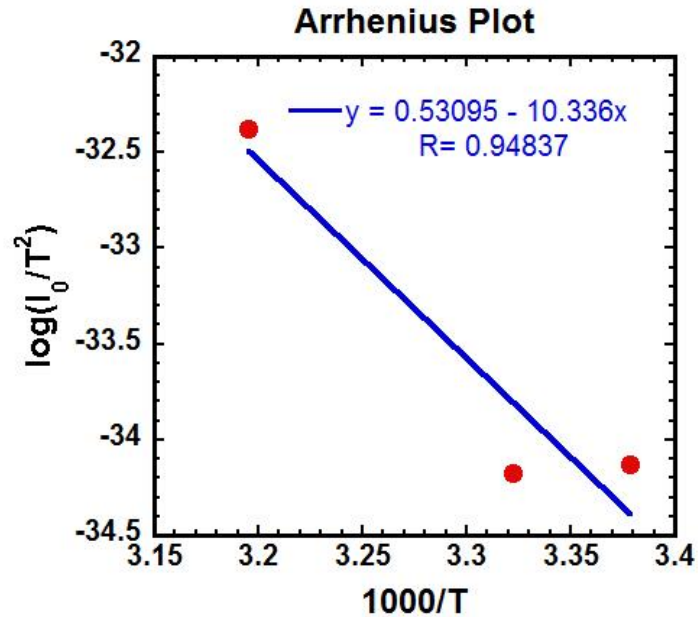


Figure 4.15.  $\log(I_0/T^2)$  vs  $1000/T$  plot to extract Richardson constant



Table 4.4 Ideality factor, reverse saturation current and SBH from Arrhenius plot

Electrical parameters
$\phi_B = 0.8907 \text{ eV}$ $A^* = 34.0109 \text{ Acm}^{-2}\text{K}^{-2}$ $m^* = m_e \times 0.2829$ $V_R = 49.114 \times 10^3 \text{ mS}^{-1}$

#### 4.3.4 Method-2: Modified Norde's Method

Equation 4.22 defines Norde's Function. If we use this function at 2 different temperatures (28°C and 41°C), Schottky barrier height, ideality factor, and series resistance can be determined using equations 4.23-4.25

$$F(V) = \frac{V}{2} - \frac{kT}{q} \ln \left( \frac{I}{AA^*T^2} \right) \quad (4.22)$$

$$\beta = \frac{kT}{q} \quad (4.23)$$

$$R_s = \frac{2 - n}{\beta I_{min}} \quad (4.24)$$

$$F(V_{min}) = \left(\frac{1}{2} - \frac{1}{n}\right) V_0 + \phi_B + \frac{\frac{2}{n} - 1}{\beta} \quad (4.25)$$

#### 4.3.5 Method-3 Cheung method

Experimental  $dV/d(\ln I)$  vs.  $I$  plot of our  $\text{In}_2\text{O}_3/\text{Graphene}$  Schottky diode at the temperature of 300 K is presented in Fig. 4.16 (a) After fitting the curve to a straight line and using equation 23,  $n$  and  $R_s$  can be determined from the intercept and the slope of the line. The value of  $n$  and the data of  $I$ - $V$  characteristics are used to define  $H(I)$  from equation (4.20). Plotting  $H(I)$  vs.  $I$  should give a straight-line as shown in Fig. 4.16 (b). Its slope and y-axis intercept will give a second determination of  $R_s$  and  $n\phi_B$ ; having two values of  $R_s$  we can check the consistency of Cheung's method. The values of  $R_s$  obtained from  $dV/d(\ln I)$  vs  $I$  and  $H(I)$  vs.  $I$  plots which are  $824 \text{ K}\Omega$  and  $827.7 \text{ K}\Omega$  respectively are in good agreement with each other. This case shows the consistency of Cheung's approach. The average  $R_s$  value for the diode was obtained to be  $825.85 \text{ K}\Omega$ .

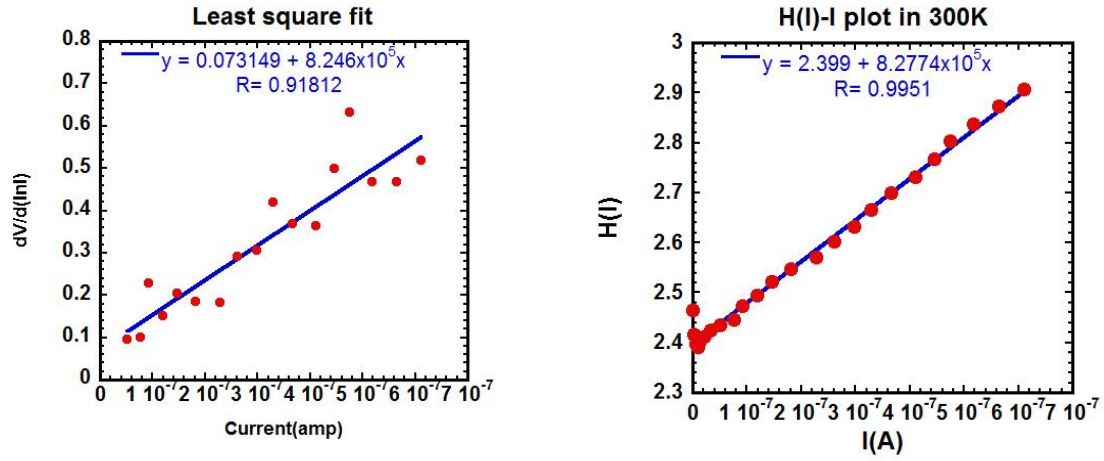


Figure 4.16. (a)  $dV/d(\ln I)$  vs.  $I$  and (b) Cheung's functions,  $H(I)$  vs.  $I$  plot of our  $\text{In}_2\text{O}_3/\text{Graphene}$  Schottky diode at the temperature of 301 K

Table 4.5 Comparisons of different methods

Thermionic Emission	$\frac{dV}{d(\ln I)}$ vs $I$ plot	$H(I)$ vs $I$ plot
$n = 1.9733$ $I_0 = 2.0074 \times 10^{-10} A$ $\phi_B = 0.9321 eV$	$n = 2.8$ $R_S = 824 k\Omega$	$R_S = 827.7 k\Omega$ $\phi_B = 0.9 eV$

#### 4.3.6 Method-4 least square solution

The I-V relation can be written as follows including the series Resistance as follows:

$$V = \frac{nkT}{q} \ln \left( \frac{I}{AA^*T^2} \right) + n\phi_b + IR_S \quad (4.26)$$

Clearly, equation (4.26) is over-determined (i.e. more equations than unknowns). So we cannot expect the exact solution of  $n, \phi_B, R_s$  which will simultaneously satisfy the equation. We can hence follow the least square error (LSE) solution method to increase the accuracy of the solution by using more I, V data. The latter two methods give more consistent data because they consider the series resistance which cannot be neglected in our case.

Table 4.6 Parameter extraction from LSE method

Electrical parameters
$n = 2$ $\phi_B = 0.83 \text{ eV}$ $R_s = 800 \text{ k}\Omega$ Minimum Error = $10^{-14}$

#### 4.3.7 Method-5 Field emission model:

At low temperature most of the current contribution is from the tunneling from the bottom of conduction band if the barrier width is thin enough. In the intermediate temperature range, electrons above a certain energy level conduct due to both field emission and thermionic emission. The thermionic field emission follows the following formula (Kwak et al., 2014)

$$I_s = \frac{AA^*(\pi E_{00})^{1/2}}{kT} \left[ -E + \frac{E_B}{\cosh^2\left(\frac{E_{00}}{kT}\right)} \right]^{1/2} \times \exp\left(-\frac{E_B}{E_0}\right) \quad (4.27)$$

Where  $E_0 = E_{00} \coth(E_{00}/kT)$ ,  $A^*$  is Richardson constant,  $A$  is effective area,  $k$  is Boltzmann constant,  $T$  is absolute temperature,  $h$  is Planck's constant,  $m^*$  is the effective mass and  $\epsilon$  is the permittivity of semiconductor,  $E$  is potential associated with an applied bias,  $E_B$  is the SBH,  $N_D$  is the impurity concentration. By constructing the plot in fig. 4.21 (a) the barrier height is determined. The bias has been varied to take the average SBH in fig. 4.21b

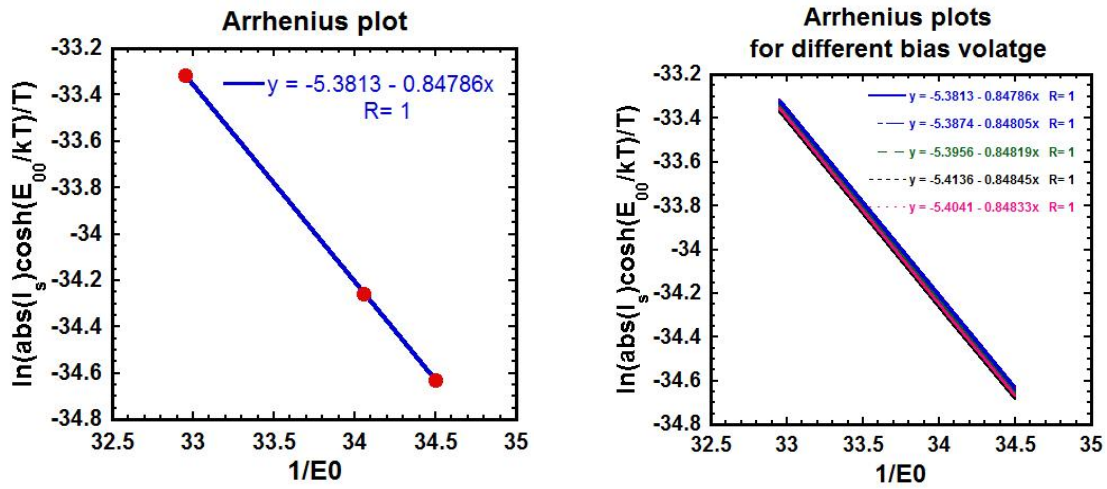


Figure 4.17. The Arrhenius plots for the barrier height extractions using TFE method (a) The barrier height of graphene/ $\text{In}_2\text{O}_3$  junction is 847 meV. (b) The average barrier height of graphene/ $\text{In}_2\text{O}_3$  junction is 848 meV by sweeping the applied bias.

#### 4.3.8 Comparison of all five models

A comparison among all the five models is stated in the following table 4.7 which shows quite comparable results.

Table 4.7 Comparison of the electrical parameters for all five methods

<b>Method</b>	<b><math>n</math></b>	<b><math>\phi_B(eV)</math></b>	<b><math>R_S(k\Omega)</math></b>
Thermionic Emission	1.9733	0.9321	-
Modified Norde	1.9	0.88	587
Cheung	2.8	0.9	825.85
LSE	2	0.83	800
Thermionic Field Emission	2.8	0.847	827.7

#### 4.4 Variation of $n$ , $\phi_B$ with Temperature

It was seen that values of  $n$ ,  $\phi_B$  and  $R_S$  are strong functions of operating temperature. With increasing temperature, barrier height decreases while ideality factor increases. Fig.4.22 indicates a decrease of  $n$  with increasing temperature. This can be attributed to the change in the current transport process from generation recombination and other mechanisms at very low temperatures, only generation recombination at the intermediate temperatures and thermionic emission from there on. The full trend is not seen because we could not vary the temperature over a large range keeping the Schottky diode behavior unaltered. As we can see, the Schottky Barrier Height

increases with temperature which is in agreement with the negative temperature coefficient of semiconductor materials. The coefficient of temperature from the fit is:

$$\alpha = -3.7 \text{ meV/oC}$$

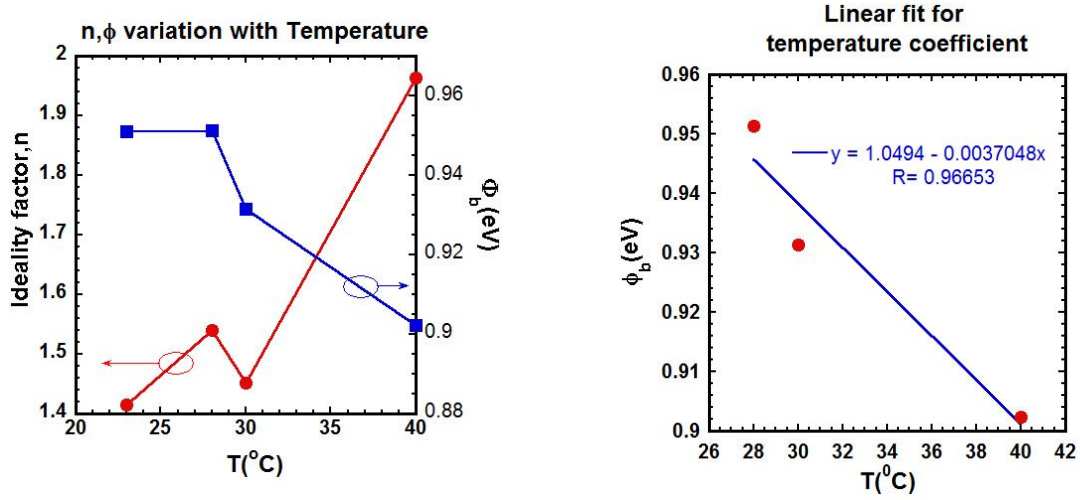


Figure 4.18. (a) Variation of  $n$ ,  $\phi_B$  with Temperature (b) Linear fit for temperature coefficient

#### 4.5 Determination of SBH in WO<sub>3</sub>/Graphene heterojunction:

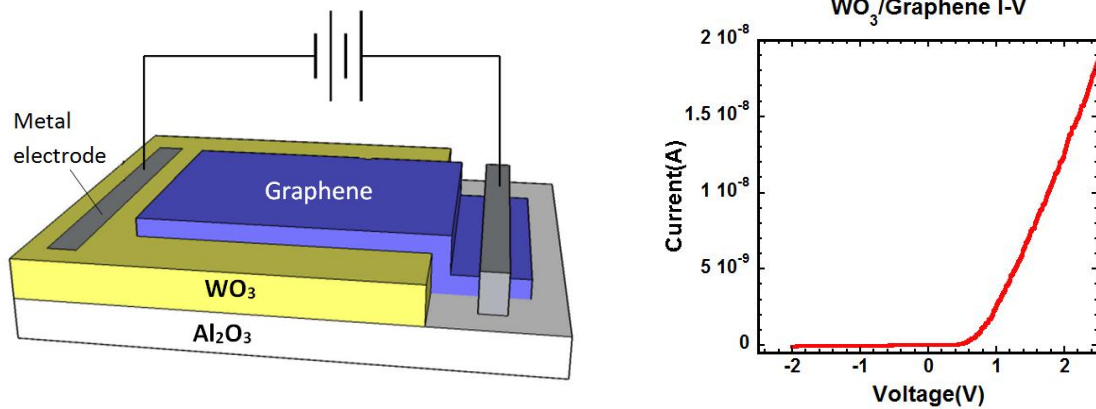


Figure 4.19 (a) Device structure of WO<sub>3</sub>/Graphene Schottky diode (b) I-V characteristics of Graphene/WO<sub>3</sub> Schottky junction at the temperature of 301K

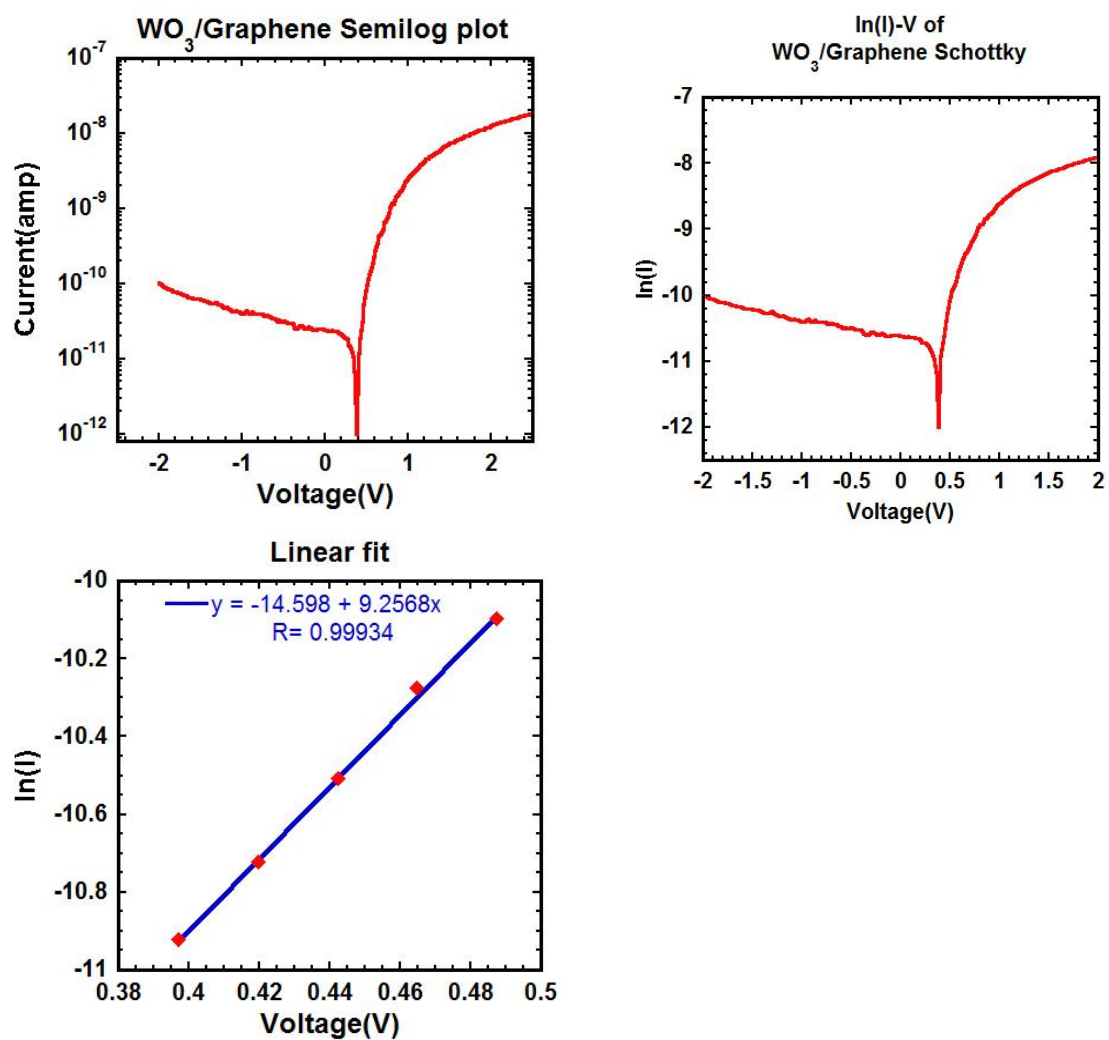


Figure 4.20. (a) I-V (semi log) characteristics (b)  $\ln I$ -V plot (c) Linear curve fit of the Graphene/ $\text{WO}_3$  Schottky junction at the temperature of 301K

The calculated parameters from the thermionic emission model are given in Table 4.8. Average velocity with which the electrons at the interface approach the barrier which velocity is referred to as the Richardson velocity given by:



$$V_R = \sqrt{\frac{kT}{2\pi m^*}} \quad (4.28)$$

Table 4.8 Parameter extraction for graphene/WO<sub>3</sub> Schottky junction at the temperature of 300K

Calculation of ideality factor, reverse saturation current and SBH
$n = 2.62$ $I_0 = 3.73 \times 10^{-8} A$ $\phi_B = 0.694 eV$ $m^* = m_e \times 0.0303$ $V_R = 155.313 \times 10^3 ms^{-1}$

The values determined from Cheung's method and LSE are given in table 4.9

Table 4.9 Comparison of Thermionic emission, Cheung's and Least square error method

Thermionic Emission	$\frac{dV}{d(\ln I)}$ vs I plot	LSE
$n = 2.62$ $\phi_B = 0.694 eV$	$n = 2.7$ $R_S = 87 M\Omega$	$R_S = 86 M\Omega$ $\phi_B \approx 1 eV$ $n = 2.83$

## 4.6 Sensing responses of In<sub>2</sub>O<sub>3</sub> and WO<sub>3</sub> to NO<sub>2</sub> and NH<sub>3</sub> with and without Graphene

### 4.6.1 Motivation

Conduction in WO<sub>3</sub> and In<sub>2</sub>O<sub>3</sub> is affected by the Schottky barrier at grain boundaries. NO<sub>2</sub> or NH<sub>3</sub> changes the SBH which ultimately causes a change in the

resistance of the films. It is observed that the graphene–WO<sub>3</sub> stack has a higher NO<sub>2</sub> sensor response than pure WO<sub>3</sub> films. This may result from two factors:

- (i) Enhancement in the gas–surface reaction due to the higher surface area and
- (ii) Modification of the potential barrier at the graphene–WO<sub>3</sub> interfaces. And the response current is exponentially dependent on the SBH since in diode structures the transport across the Schottky barrier junction is governed by thermionic emission model given by equation 4.12

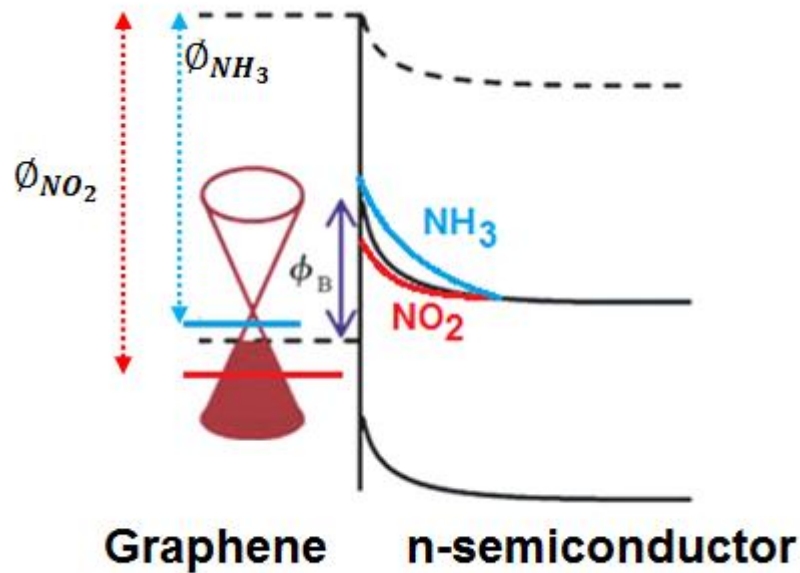


Figure 4.21. Carrier transport through the graphene-semiconductor Schottky barrier

If we make a Schottky diode by use of graphene-semiconductor heterostructure SBH will be determined by the difference of graphene's Fermi level and

semiconductor's electron affinity as illustrated in Figure 4.21 with the help of graphene/n-Semiconductor equilibrium band diagram. The exposure of analytes on graphene surface will move its Fermi level up or down depending upon the type of doping. The current in reverse bias will respond exponentially to number of adsorbed molecule in graphene semiconductor. Even if it is in the forward bias zone, as the current changes exponentially because of diode characteristics, the response is much better than the normal resistor.

WO<sub>3</sub>, In<sub>2</sub>O<sub>3</sub>, ZnO these transition metal oxide senses based on chemiresistivity i.e. the change of resistance on the exposure of different gases. The gas molecules are either electron donor or acceptor. Depending on the type of the semiconductor (p or n-type), the resistance changes. Usually in ambient condition oxidizing gases increases the resistance (n-type) of the semiconductor and converse for p-type. The chemiresistance property can be attributed to the depletion boundary created around the grains due to the charge transfer of the gas in semiconductor surface. That's why grain size and interconnection between them play a vital role in sensing mechanism. The width of the grain acts as a potential barrier between grains, where the Fermi level changes due to the interaction of the gas molecules across those boundaries as depicted in fig. 4.22. The band bends up if an oxidizing gas takes electron away from the n-type semiconductor's conduction band and converse is true for p-type.

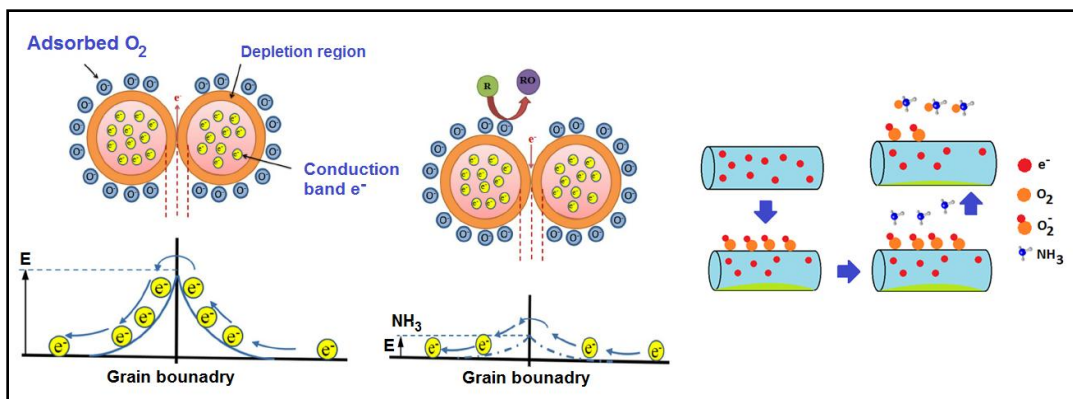


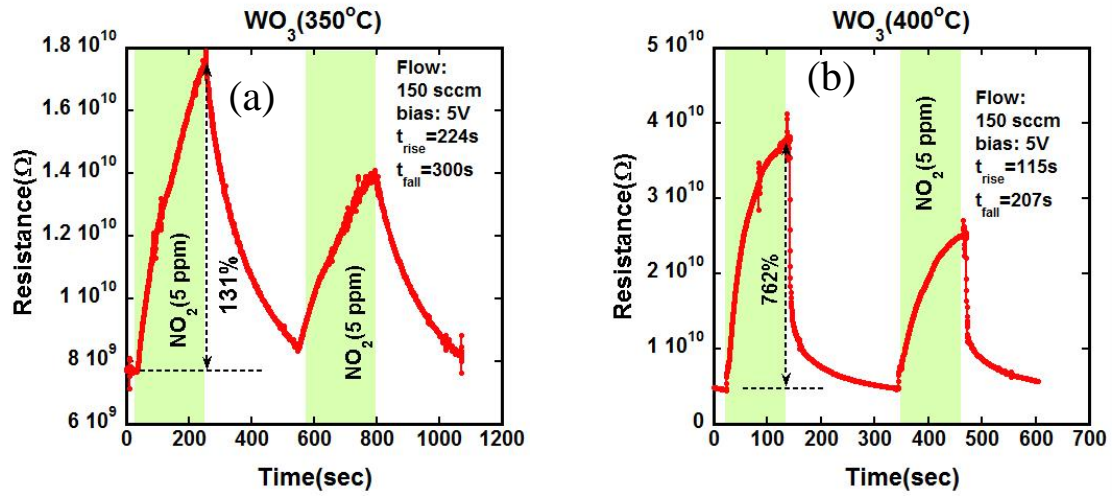
Figure 4.22 Sensing mechanisms in transition metal oxide

$\text{WO}_3$  is a well-known n-type semiconductor material and CVD grown graphene as a p-type semiconductor. This results in hetero-junctions at the interface of n- $\text{WO}_3$  and p-graphene in the heterostructure. Therefore, the change in the adsorbed oxygen concentration in the presence of oxidizing gas takes place at two types of interface; at the n- $\text{WO}_3$ /p-graphene interface and at the grain boundaries of  $\text{WO}_3$  particles. These two factors change the SBH. Therefore, an improvement in the sensor response in the case of graphene- $\text{WO}_3$  (and  $\text{In}_2\text{O}_3$ ) films is expected.

#### 4.6.2 Gas sensing response of $\text{WO}_3$ to $\text{NO}_2$ (Room Temperature)

Although the actual mechanism of the charge exchange between graphene and adsorbed molecules is not so obvious, a clear sign of chemisorptions causes the resistance of  $\text{WO}_3$  changes upon exposure of  $\text{NO}_2$  or  $\text{NH}_3$  molecules. This changes current and resistance which is recoded as a function of time. It can be mentioned here that that all the measurements are taken under ambient conditions to assess the possibility of making practical sensors using graphene and  $\text{WO}_3$ . In fig. 4.23 a it can be

observed that the transient sensor response of  $\text{WO}_3$  to  $\text{NO}_2$  (5 ppm) as the flow is turned on and then off, the ON time is shaded in green. The flow rate was 150 sccm. The bias voltage was 5V. It can also be seen that the sensing response changes with the annealing temperature and the response and recovery time also varies as well.



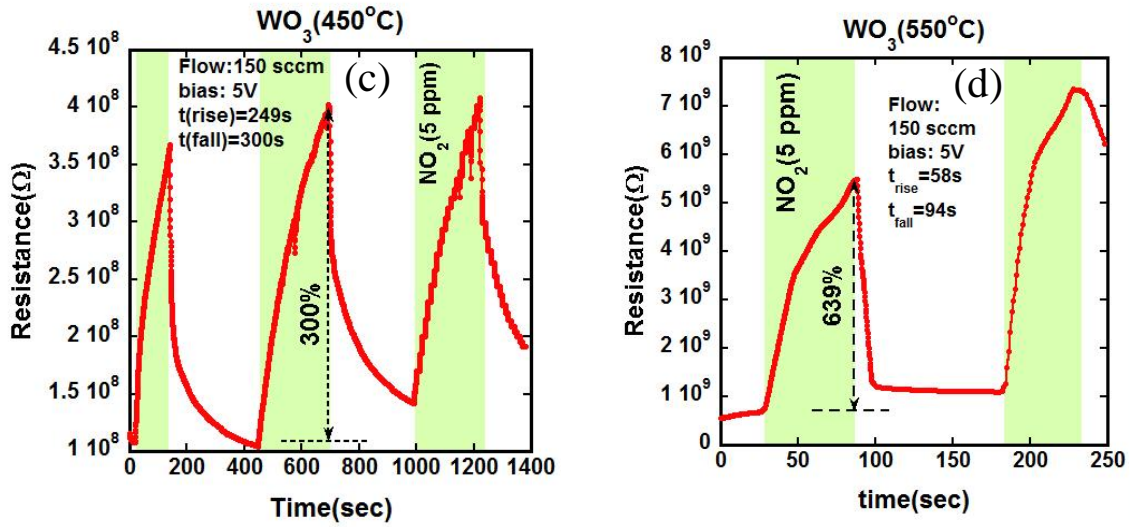


Figure 4.23 (a) transient response of  $\text{WO}_3$  annealed at (a) 350°C, (b) 400°C, (c) 450°C and (d) 550°C to  $\text{NO}_2$  (5 ppm)

Sensitivity is defined as percentage resistance change caused by the flow of the gas, and calculated as  $100 \times (R_g - R_0)/R_0$ , where  $R_0$  is the base resistance in absence of the test gas, and  $R_g$  is the resistance in presence of the gas at the given exposure time. As can be observed from the fig. 4.23, the resistance increases at the exposure of the gas which is expected. When the  $\text{WO}_3$  sensor is kept open in air, the  $\text{O}_2$  molecules are adsorbed in the surface and after taking electron they become ionized species and capturing electron, they leave the surface more depleted which is even aided more by  $\text{NO}_2$  molecules which is an electron acceptor. Consequently it takes away more free carriers from the conduction band and also interacts with the ionic species increasing the resistance even further.

The crystal structure of  $\text{WO}_3 \cdot 2\text{H}_2\text{O}$  transforms to  $\text{WO}_3$  at 200 °C where short-range order shows up. Low annealing temperature is not enough for rearranging lattice and formation of sequential crystal structure. At 400 °C monoclinic  $\text{WO}_3$  appears. Annealing at 600 °C leads to further improvement in the crystalline properties of the film. The re-crystallization therefore affects many electrical parameters due to crystal orientation and reducing defects. The transient response has been fitted with exponential curve with MATLAB for finding the time constant for both rise and fall time which is plotted in fig. 4.24 (Appendix A). The inverse of parameter b and d of table 4.9 is time constant for the graphs in fig. 4.24.

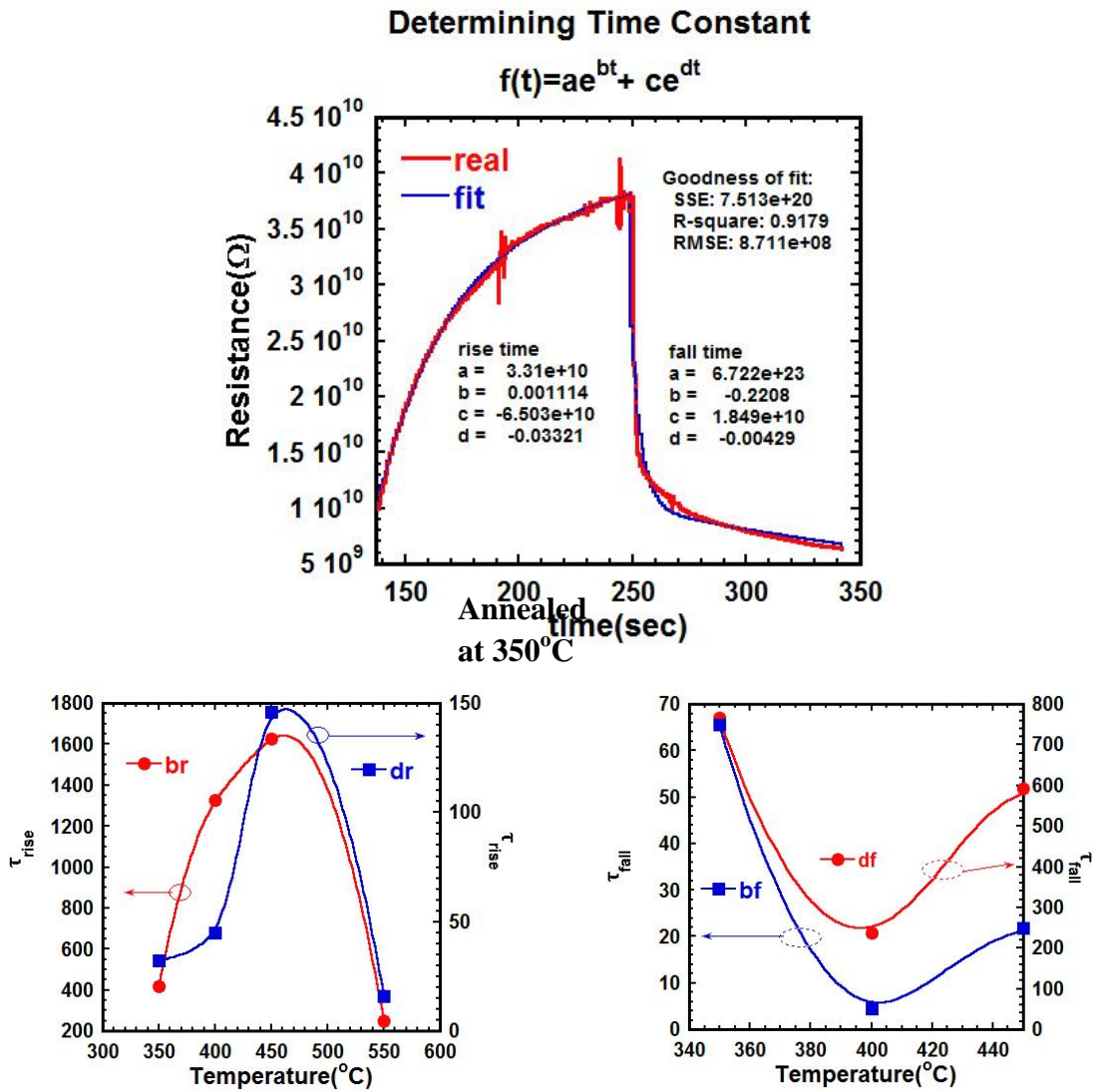


Figure 4.24 (Top) MATLAB fitting for the sensing response at 350°C annealing temperature, fitted time constant (bottom left) rise (bottom right) fall varies with annealing temperature due to re-crystallization



Table 4.10 Time constant variation with annealing temperature for WO<sub>3</sub>

Temp(°C)		Exponential fitting coefficients				R <sup>2</sup>
		a	b	c	d	
350	rise	1.11E+10	0.002378	2.63E+09	0.03121	0.9976
	Fall	2.45E+11	-0.01526	1.71E+10	0.001305	0.9997
400	Rise	4.50E+10	0.0007547	-.44E+10	0.02239	0.9964
	Fall	1.23E+24	-0.2241	1.81E+10	0.00421	0.9485
450	Rise	2.95E+08	0.0006142	6.04E+09	0.006853	0.9992
	Fall	1.01E+22	-0.04608	7.31E+08	0.001691	0.9616
550	rise	3.79E+09	0.003987	2.32E+10	-0.0625	0.951
	fall	4.41E+06	-4.043	1.44E+09	0.09534	0.9986

It is observed from fig.4.25 that mobility, resistivity, carrier concentration, response time are dependent on annealing temperature of WO<sub>3</sub>. The mobility shows an increasing mobility which is mainly due to the modification of crystalline structure of WO<sub>3</sub>. The mobility increases because of the defect sites gets reduced. The number of grain boundaries also decreases because of the aforesaid re-crystallization. Normally the initial crystal can possess some oxygen vacancies. These vacancies trap the carriers. The trapped carriers don't take part in the Hall mobility experiment, but they scatter the free carriers which in turn decreases mobility and carrier concentrations. So with higher annealing temperature the vacant sites decrease because of the availability of the O<sub>2</sub> surroundings. Additionally the response time also improves significantly because the more trap sites mean more carriers get trapped, the slower the response should be. Reducing traps make the transients faster as observed in fig. 4.25d.

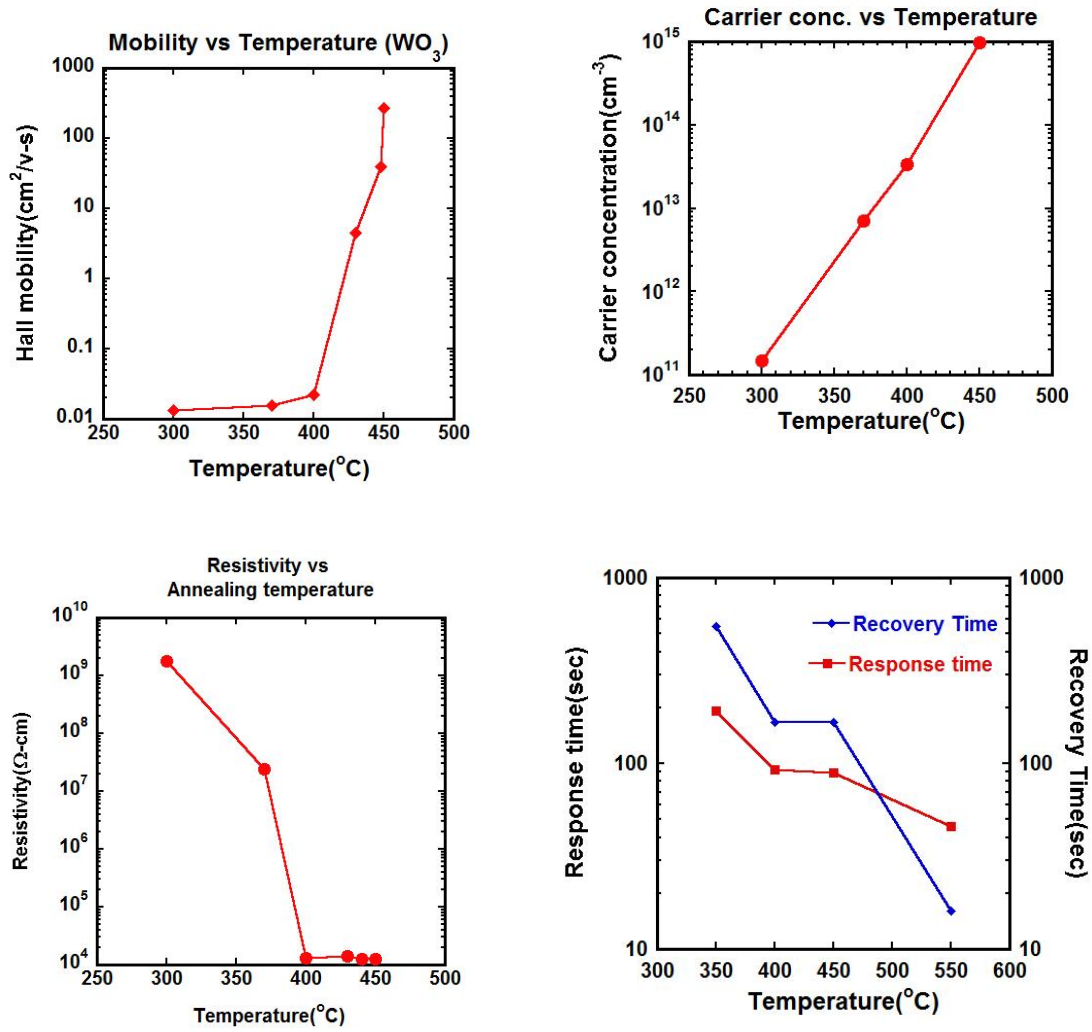


Figure 4.25 Annealing temperature dependence of (a) Hall mobility (b) Carrier concentration (c) Resistivity and (d) Response and recovery time

#### 4.6.3 Comparison of different metal oxide semiconductors' $\text{NO}_2$ response time

We had three transition metal oxides viz.  $\text{ZnO}$ ,  $\text{WO}_3$  and  $\text{In}_2\text{O}_3$ . We measured Hall mobility ( $\mu$ ), bulk concentration ( $N_b$ ), resistivity ( $\rho$ ) and a comparison is shown in fig. 4.27. We carried out the sensing experiment for all of them. Their transient

response to 5ppm NO<sub>2</sub> at a flow rate of 150 sccm. ZnO and WO<sub>3</sub> had to be annealed to conduct and measure the sensitivity.

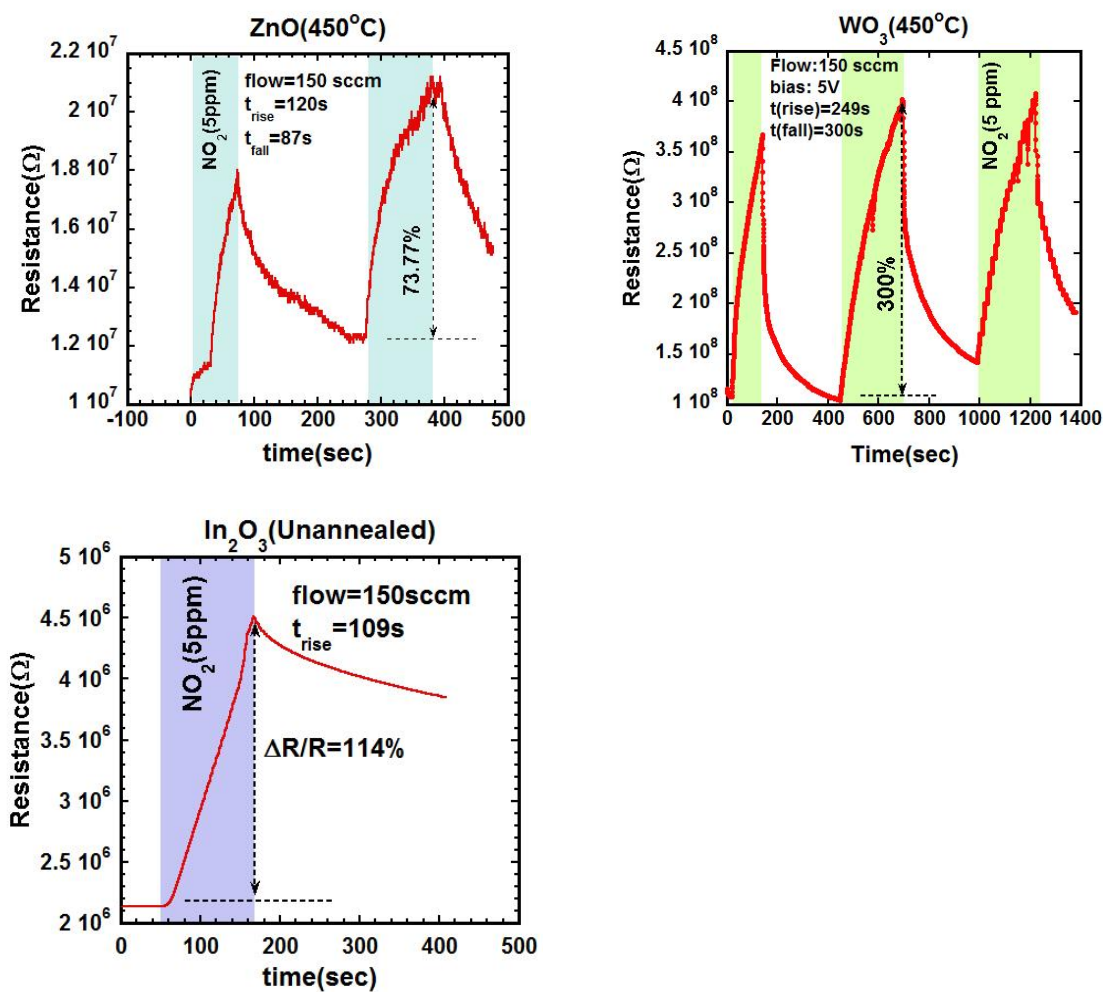


Figure 4.26. Transient response of different metal oxide semiconductor without graphene (a) ZnO (b)WO<sub>3</sub> (c) In<sub>2</sub>O<sub>3</sub> to 5ppm, 150 sccm of NO<sub>2</sub>

Table 4.11 Comparison of different metal oxide properties

Material	Carrier Conc. (cm <sup>-3</sup> )	Mobility (cm <sup>2</sup> V <sup>-1</sup> s <sup>-1</sup> )	Resistivity (ohm-cm)
ZnO	1.30E+13	2.27	3.55E+03
In <sub>2</sub> O <sub>3</sub>	1.81E+17	0.116	3.83
WO <sub>3</sub>	1.37E+12	0.373	4.68

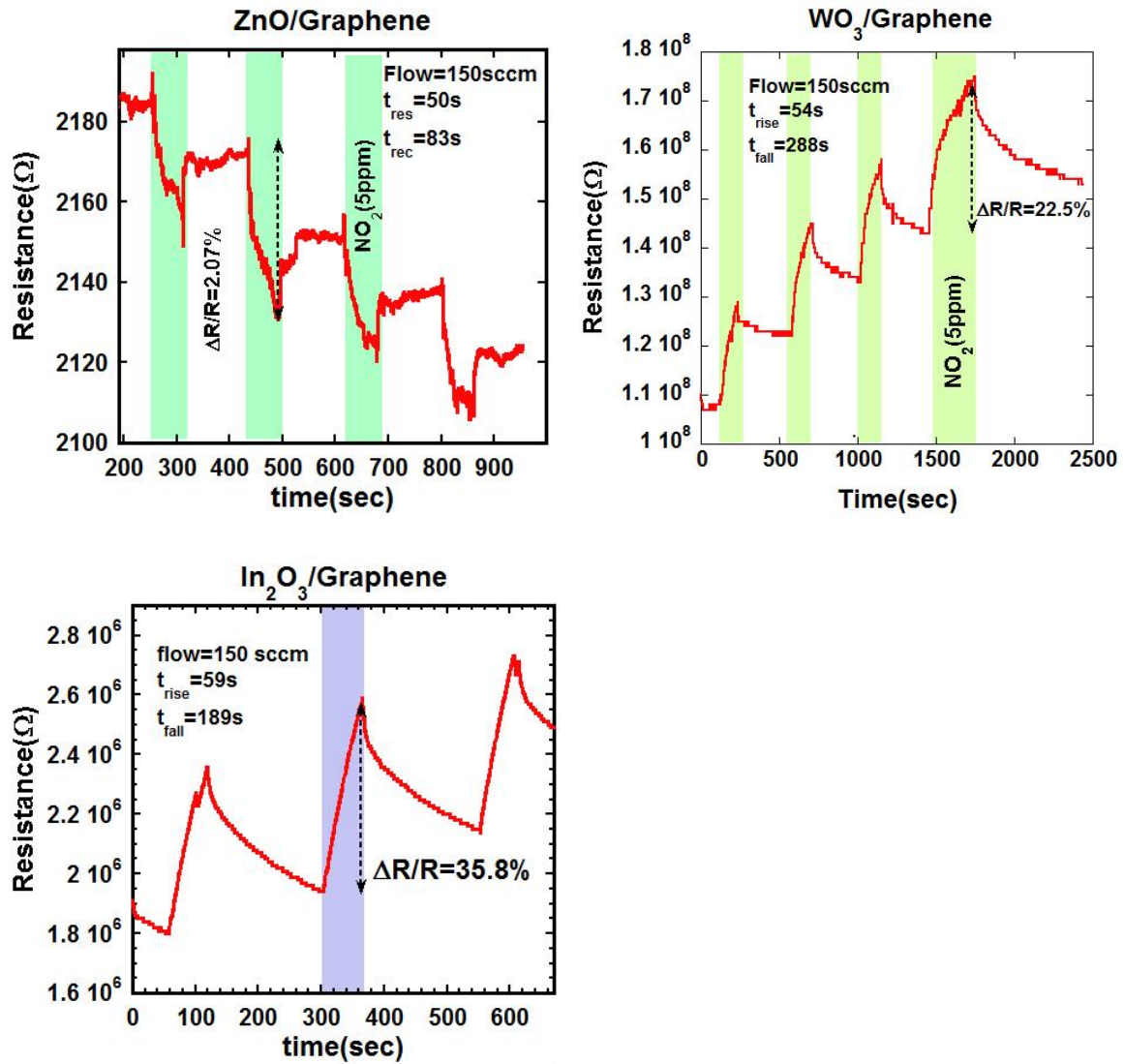


Figure 4.27. Sensing response of different metal oxide semiconductor with graphene

(a) ZnO (b) WO<sub>3</sub> (c) In<sub>2</sub>O<sub>3</sub> in exposure of 5ppm 150 sccm NO<sub>2</sub>

Table 4.12 NO<sub>2</sub> Response time with and without Graphene for different samples (WO<sub>3</sub>, In<sub>2</sub>O<sub>3</sub>, ZnO)

Material	Response time		Recovery time	
	Without graphene	With Graphene	Without graphene	With Graphene
ZnO	106	53	580	101
WO <sub>3</sub>	89	54	550	288
In <sub>2</sub> O <sub>3</sub>	68.83	59	600	189

#### 4.6.4 Sensitivity improvement

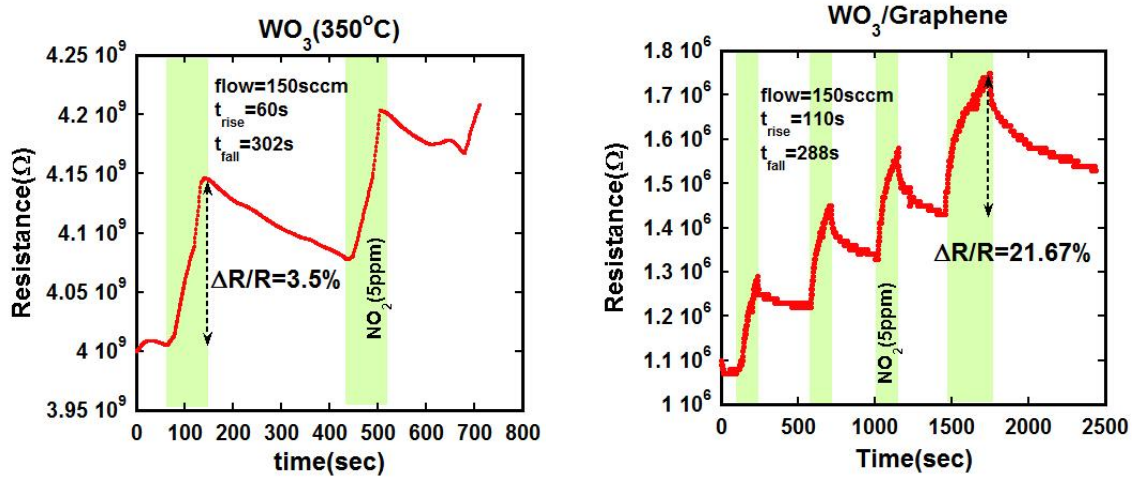


Figure 4.28 Sensitivity of WO<sub>3</sub> (a) without graphene (b) with graphene to NO<sub>2</sub>  
exposure (150sccm, 5 ppm)

#### 4.6.5 Response time comparison of different metal oxides (NH<sub>3</sub> exposure)

Figure 4.29 shows the room-temperature response for graphene for NH<sub>3</sub>. It is clear from figure that graphene behaves as a p-type semiconductor, since its resistance increases in the presence of a reducing species. The NH<sub>3</sub> concentration was 437 ppm.

In the presence of  $\text{NH}_3$ -  $\text{WO}_3$ , as well as  $\text{In}_2\text{O}_3$  behave as an n-type semiconductor. The response was noise affected, as they show a high resistance at room temperature.

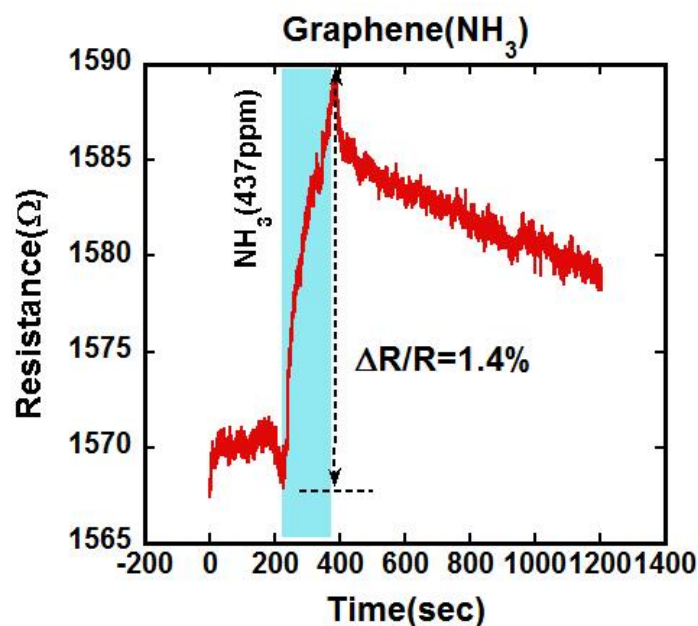
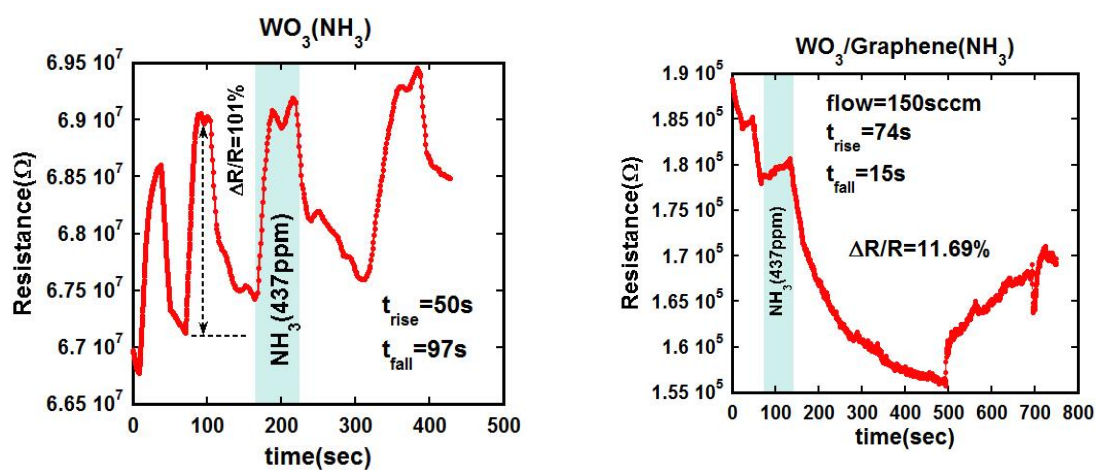


Figure 4.29. The response for graphene on  $\text{SiO}_2/\text{Si}$  for  $\text{NH}_3$  indicating p-type graphene



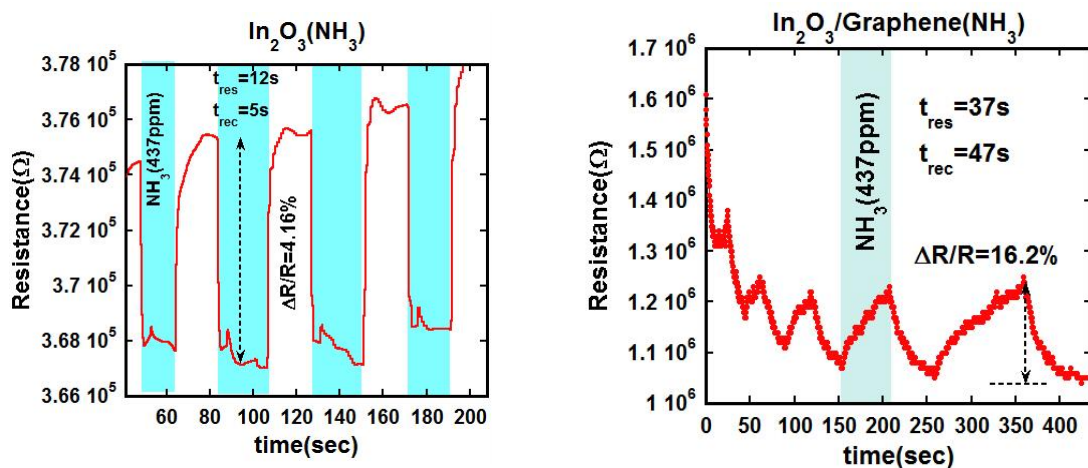


Figure 4.30. Sensing response of different metal oxide semiconductor with graphene

(a)  $\text{ZnO}$  (b)  $\text{WO}_3$  (c)  $\text{In}_2\text{O}_3$  in exposure of 5ppm 150 sccm  $\text{NO}_2$

The sensor based on  $\text{WO}_3$ –graphene showed a better response to  $\text{NO}_2$  while sensor based on  $\text{In}_2\text{O}_3$ –graphene showed a better response to  $\text{NH}_3$  than that of the semiconductor itself. The value of response for the graphene sensor for 437 ppm of  $\text{NH}_3$  gas was 1.41%. Similarly, the value of sensitivity for the  $\text{In}_2\text{O}_3$  sensor was 4.16% and with graphene it was 16.20%. To the contrary, the value of sensitivity for the  $\text{WO}_3$  sensor to 5ppm  $\text{NO}_2$  was 3.5% and with graphene it was 21.67%. The earlier reports also shows improvement for  $\text{CNT-WO}_3$  and  $\text{Graphene-WO}_3$  nanocomposites (Srivastava et al., 2012) but our case it is much simpler device structure, no complex fabrication involved. The comparison of the sensitivity and response time are shown in table 4.12 and table 4.13 respectively.

Table 4.13 Sensitivity comparison with and without graphene

Material	Without graphene	With Graphene	Gas
WO <sub>3</sub>	3.50%	21.67%	NO <sub>2</sub>
In <sub>2</sub> O <sub>3</sub>	4.16%	16.20%	NH <sub>3</sub>

Table 4.14 NH<sub>3</sub> Response time with and without Graphene for different samples (WO<sub>3</sub>, In<sub>2</sub>O<sub>3</sub>)

	Response time		Recovery time	
Material	Without graphene	With Graphene	Without graphene	With Graphene
WO <sub>3</sub>	50	74	97	15
In <sub>2</sub> O <sub>3</sub>	12	37	5	47

#### 4.6.5 Effect of temperature of sensitivity and response time

The gas sensing experiments were also carried out for ZnO at operating temperatures 28°C and 200°C for 5 ppm NO<sub>2</sub>. Figure 4.31 shows the effect of the operating temperature on the sensor sensitivity, response and recovery time. It can be clearly observed that the response and recovery time gets better as well as the sensitivity gets higher. When temperature increase the surface carrier concentration goes higher which implies NO<sub>2</sub> will absorb the carrier faster than before to reach saturation. Therefore the response time gets better. In fact this explains the improvement of the sensitivity too since more carriers will be exchanges due to the elevated temperature, so the response is also expected to be better. Furthermore with



the excess temperature the adsorbed molecule will go away faster which in turn mean faster recovery. The sensitivity and response time comparison is given in Table 4.15.

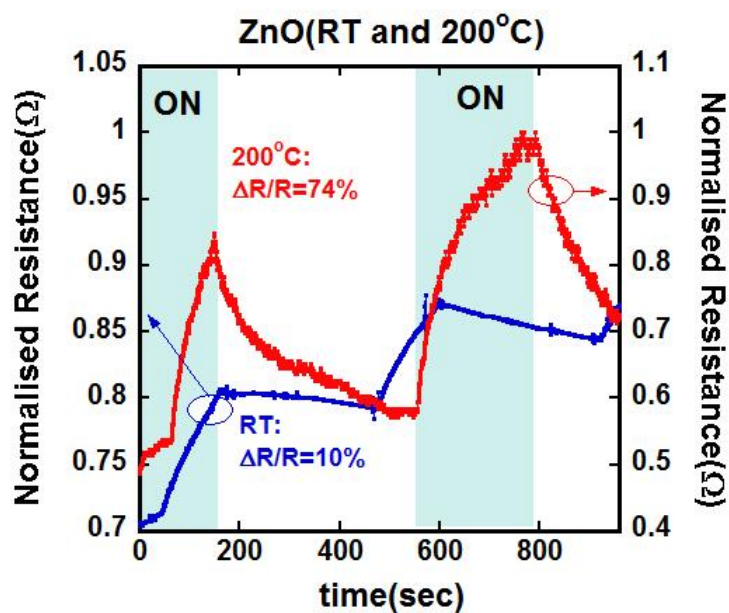


Figure 4.31. Effect of operating temperature on NO<sub>2</sub> response of ZnO sensors at 5 ppm of NO<sub>2</sub> gas.

Table 4.15 Effect of temperature of sensitivity and response time

Material	Temperature	Sensitivity	Response Time	Recovery Time
ZnO	28°C	10%	105	339
	200°C	74%	43	173

## CHAPTER 5

### CONCLUSIONS

#### 4.1 Summary

The I-V characteristics of  $\text{In}_2\text{O}_3$ , (and  $\text{WO}_3$ ) and graphene Schottky Junction have been measured and various electrical parameters have been extracted in 5 different methods and they showed consistent values. It was seen that the calculated parameters e.g. ideality factor, Schottky barrier height, has dependence on operating temperature. From the sensing plots, time constant, rise time, fall time, sensitivity were also compared for  $\text{In}_2\text{O}_3$ ,  $\text{WO}_3$  and ZnO for different annealing temperatures with and without graphene. Sensitivity, sensing and recovery time were improved with graphene. The response and recovery time also improved with operating temperature.

#### 4.2. Challenges and Recommendation for Future Research

Lower adhesion of graphene on the metal oxide semiconductor due to surface roughness was a vital challenge which made it really difficult to remove the PMMA from the top of graphene which in effect affected the sensing and diode behavior to some extent. Consequently the devices were hard to reproduce on a regular basis. Different solvents apart from acetone (e.g. 1, 2-Dichloroethane, dichloromethane and so on) can be used to check the feasibility of removal of PMMA from this rough surface. Any transferring mechanism which deals with rough feature of surface can also do much improvement.

The recovery time was little delayed because of the lack of removal of exposed gas immediately. It can be made better by using venting with a pump.

C-V characteristics can be utilized to further look into the parameters like barrier height, carrier concentration, oxide charge, contamination from mobile ions and improve the sensitivity and response time. As in case of I-V characteristics, the leakage current is a potential source of noise which C-V measurement doesn't have. It is more accurate and allows us more insight into the junction characteristics.

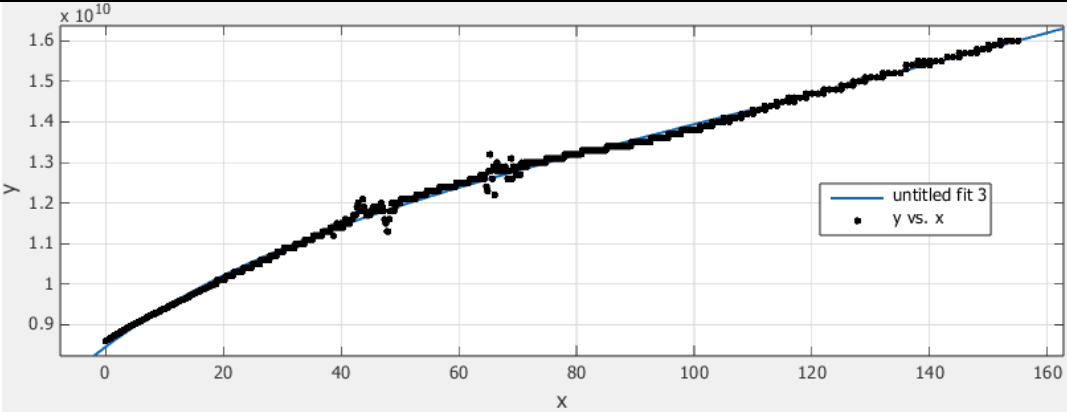
All sensing were focused on the room temperature. Elevating temperature showed some better performance which can also be utilized in future with some micro heater element integrated with the device.

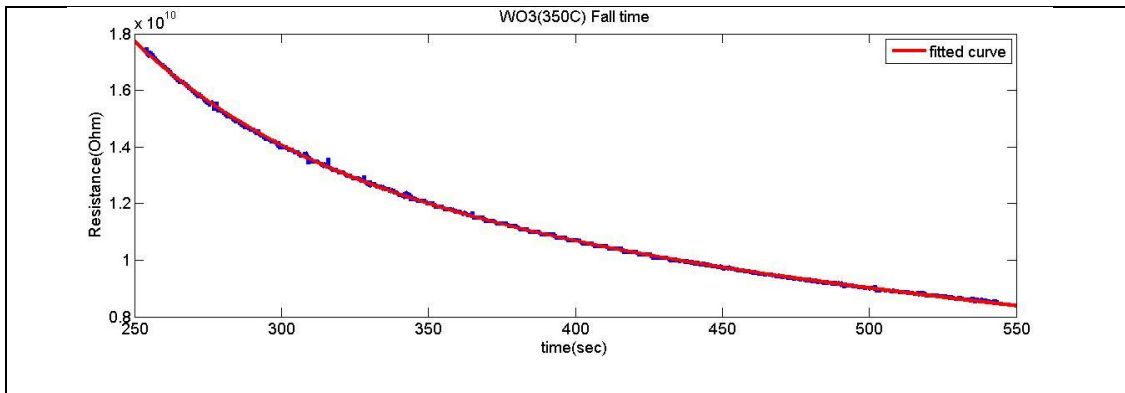
In our case, series resistance was really dominant as also revealed from our earlier discussion. So different device structure, graphene area, contact distance was proposed for a better. The designs are given in appendix B

## APPENDICES

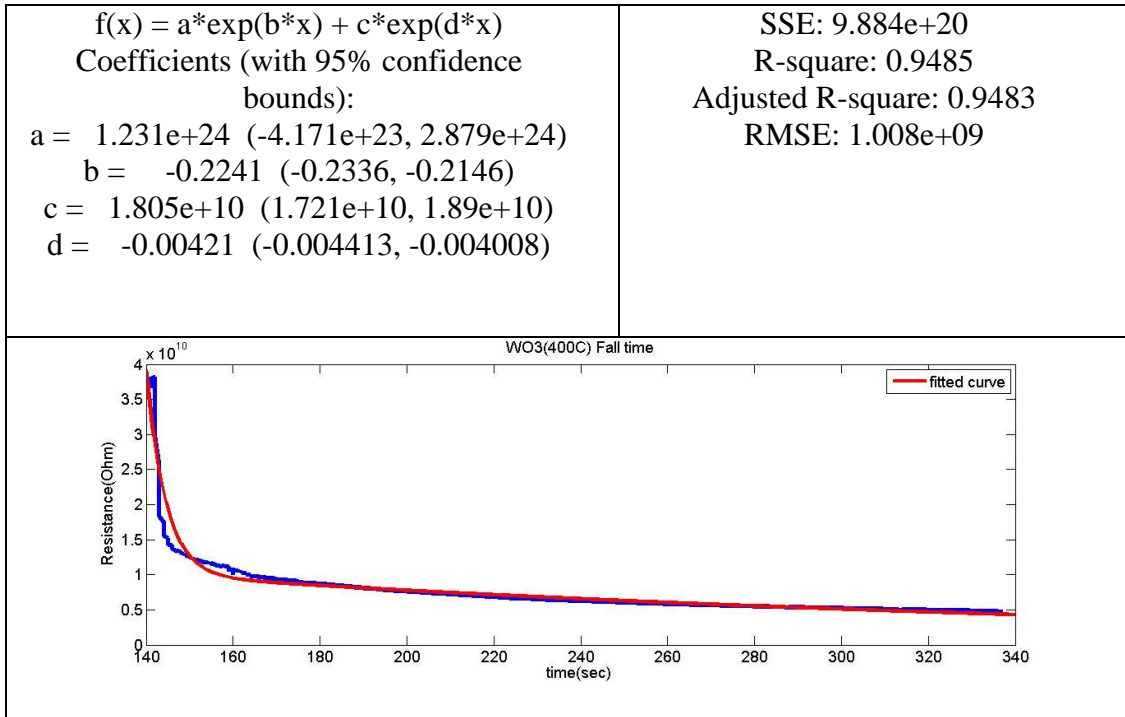
Appendix A  
MATLAB Codes

Fitting the rise and fall time with MATLAB

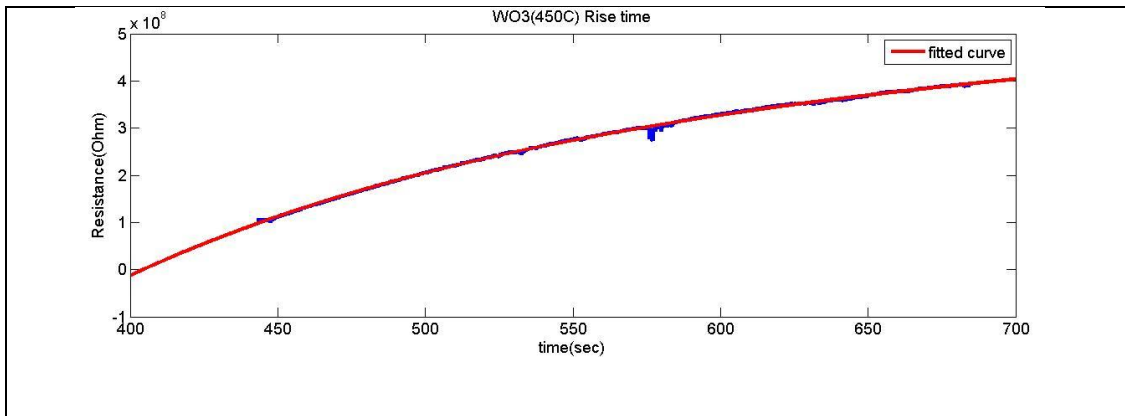
WO <sub>3</sub> (350°C)	
rise time	
<p>General model Exp2:  <math>f(x) = a \cdot \exp(b \cdot x) + c \cdot \exp(d \cdot x)</math>  Coefficients (with 95% confidence bounds):  a = 1.108e+10 (1.1e+10, 1.116e+10)  b = 0.002378 (0.002328, 0.002429)  c = -2.63e+09 (-2.699e+09, -2.561e+09)  d = -0.03121 (-0.03296, -0.02946)</p>	<p>Goodness of fit:  SSE: 7.5e+18  R-square: 0.9976  Adjusted R-square: 0.9976  RMSE: 9.895e+07</p>
	
Fall time	
<p>General model Exp2:  <math>f(x) = a \cdot \exp(b \cdot x) + c \cdot \exp(d \cdot x)</math>  Coefficients (with 95% confidence bounds):  a = 2.447e+11 (2.347e+11, 2.546e+11)  b = -0.01526 (-0.01545, -0.01506)  c = 1.708e+10 (1.693e+10, 1.723e+10)  d = -0.001305 (-0.001321, -0.001288)</p>	<p>Goodness of fit:  SSE: 2.244e+18  R-square: 0.9997  Adjusted R-square: 0.9997  RMSE: 3.953e+07</p>



WO <sub>3</sub> (400 °C)	
rise time	
<p>General model Exp2:  <math>f(x) = a \cdot \exp(b \cdot x) + c \cdot \exp(d \cdot x)</math></p> <p>Coefficients (with 95% confidence bounds):</p> <p><math>a = 4.499\text{e}+10</math> (4.118e+10, 4.88e+10)</p> <p><math>b = -0.0007547</math> (-0.001253, -0.0002564)</p> <p><math>c = -6.436\text{e}+10</math> (-6.74e+10, -6.132e+10)</p> <p><math>d = -0.02239</math> (-0.02399, -0.02079)</p>	<p>Goodness of fit:</p> <p>SSE: 2.094e+20</p> <p>R-square: 0.9964</p> <p>Adjusted R-square: 0.9964</p> <p>RMSE: 5.988e+08</p>
Fall time	
General model Exp2:	Goodness of fit:



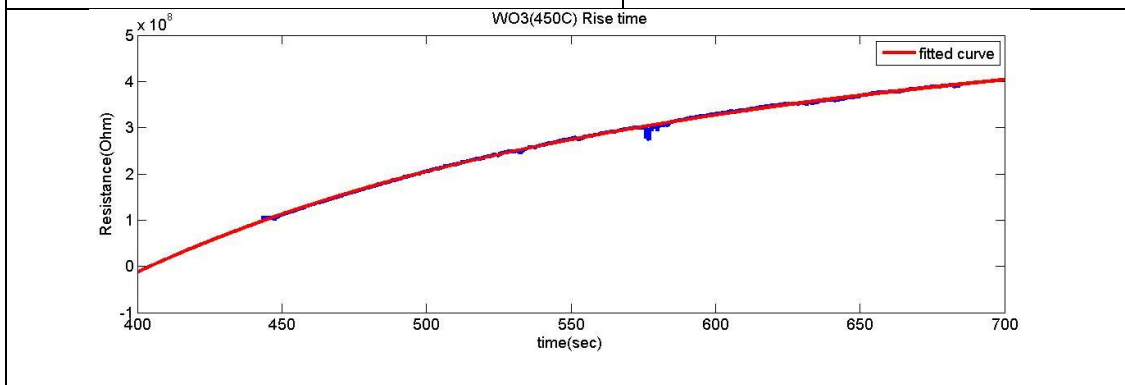
WO <sub>3</sub> (450 °C)	
rise time	
<p>General model Exp2:</p> $f(x) = a \cdot \exp(b \cdot x) + c \cdot \exp(d \cdot x)$ <p>Coefficients (with 95% confidence bounds):</p> <p><math>a = 2.951\text{e}+08</math> (2.62e+08, 3.281e+08)</p> <p><math>b = 0.0006142</math> (0.0004798, 0.0007486)</p> <p><math>c = -6.042\text{e}+09</math> (-6.746e+09, -5.337e+09)</p> <p><math>d = -0.006853</math> (-0.00727, -0.006436)</p>	<p>Goodness of fit:</p> <p>SSE: 6.697e+15</p> <p>R-square: 0.9992</p> <p>Adjusted R-square: 0.9992</p> <p>RMSE: 2.371e+06</p>



Fall time

General model Exp2:  
 $f(x) = a \cdot \exp(b \cdot x) + c \cdot \exp(d \cdot x)$   
 Coefficients (with 95% confidence bounds):  
 $a = 1.014e+22$  (-9.238e+21, 2.951e+22)  
 $b = -0.04608$  (-0.04883, -0.04334)  
 $c = 7.309e+08$  (6.956e+08, 7.662e+08)  
 $d = -0.001691$  (-0.001747, -0.001636)

Goodness of fit:  
 SSE: 1.031e+17  
 R-square: 0.9616  
 Adjusted R-square: 0.9615  
 RMSE: 8.524e+06



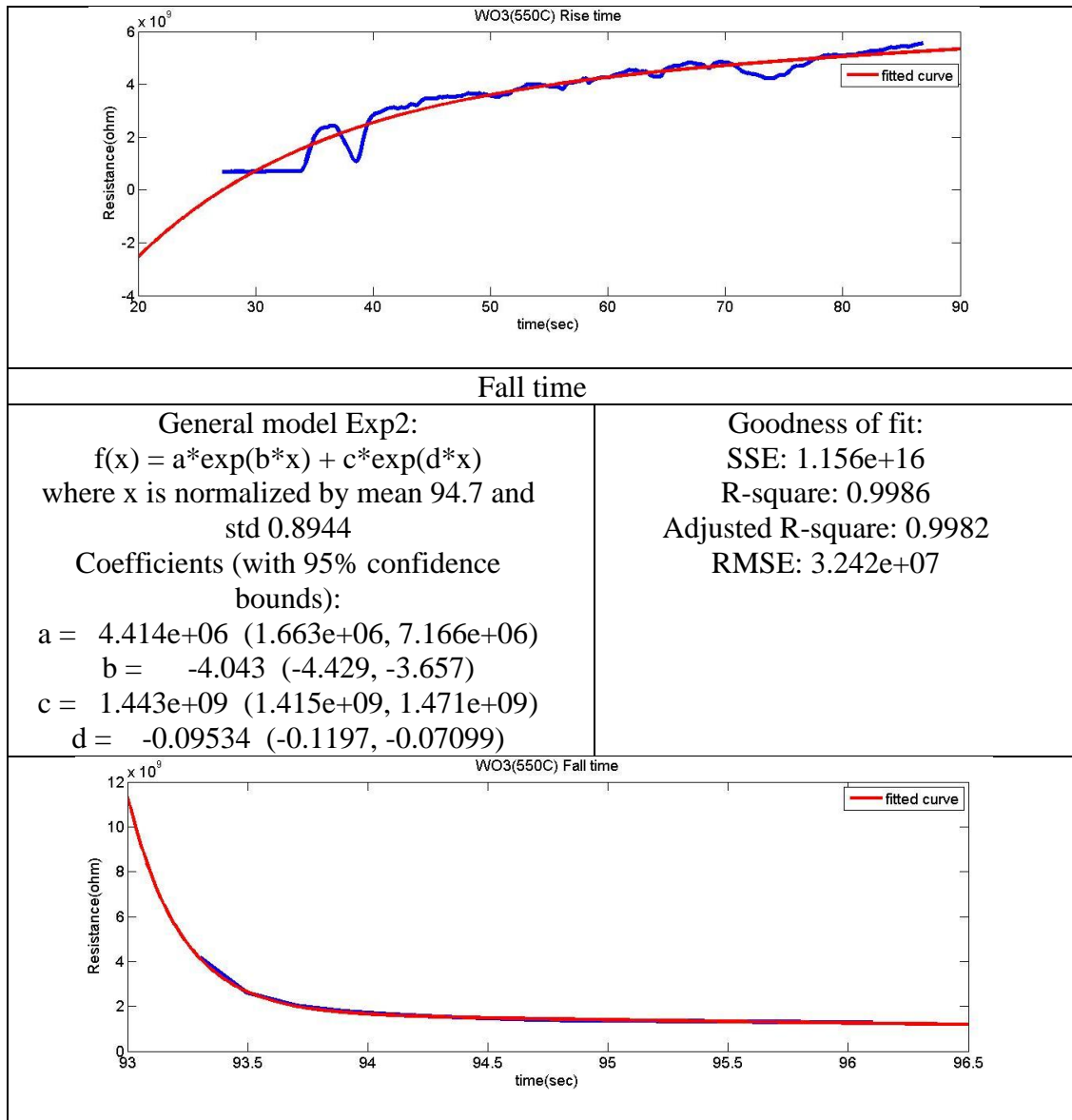
WO<sub>3</sub>(550 °C)

Rise time

General model Exp2:  
 $f(x) = a \cdot \exp(b \cdot x) + c \cdot \exp(d \cdot x)$   
 Coefficients (with 95% confidence bounds):  
 $a = 3.789e+09$  (2.798e+09, 4.78e+09)  
 $b = 0.003987$  (0.001014, 0.006959)  
 $c = -2.316e+10$  (-3.003e+10, -1.63e+10)  
 $d = -0.0625$  (-0.07846, -0.04653)

Goodness of fit:  
 SSE: 2.959e+19  
 R-square: 0.951  
 Adjusted R-square: 0.9505  
 RMSE: 3.178e+08





#### MATLAB code for finding SBH

```

clc
clear all
close all

% Constants
vt=0.0259;
R=36;      % richardson for In2O3
T=300;
A=0.25;    % cm-2

```

```

excel read
filename = 'IV_40.csv';
sheet = 1;
VRange = 'D2:D51';
IRange = 'E2:E51';
V= xlsread(filename,sheet,VRange);
I= xlsread(filename,sheet,IRange);

figure(1)
I-V curve
plot(V,I)

figure(2)
%semilog scale(I-V)
semilogy(abs(I))

logI=log(abs(I));

log(I)-V curve
figure(3)
plot(V,logI)

calculating I0(from Kaleidagraph)

% temp=23
intercept=-22.752;
slope=26.344;

% temp=28
intercept=-22.759;
slope=24.837;

% temp 30
intercept=-22;
slope=20;

% temp=40
intercept=-20.886;
slope=19.48;
% temp=41
intercept=-22.607;
slope=26.359;
%

n=(1/vt)*(1./slope)
I0=exp(intercept)
phiB=vt*log(A*R*T^2/I0)

```

```

%% second method
series resistance included
dV=diff(V);
dlogI=diff(logI);
ddV=dV./dlogI;
TF=isinf(ddV);
ddV_new=ddV(~isinf(ddV));
figure(4)
I=I(2:end);
I(find(TF'))=[];
I;

plot(I,ddV_new)

```

#### MATLAB code for ARRHENIUS plot

```

clc
close all
clear all

% richardson constant
A=.05; % cm-2
T=[23 28 40 ]+273; % K
k=8.617e-5; % eV/K
I0=[1.315 1.3058 8.4982].*1e-10;
y=log(I0./T.^2)
x=1000./T
plot(x,y)

intercept=0.53095;
slope=-10.336;

R=exp(intercept)/A
phiB=-slope*k*1000

```

#### MATLAB code for LSE

```

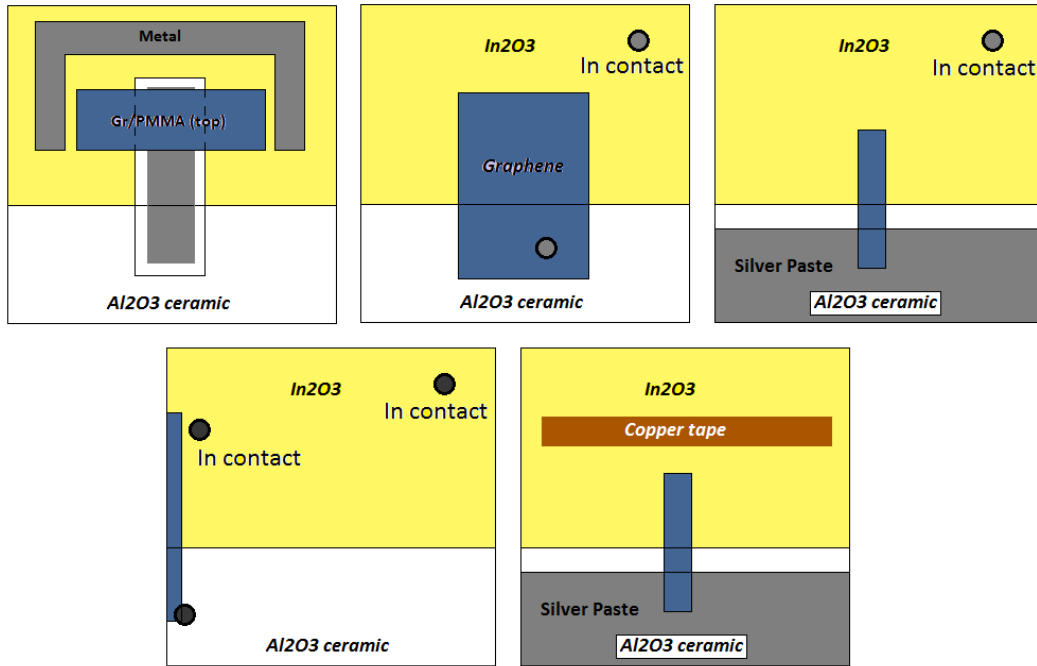
clc
close all
clear all

T=273+(28);
kTq=1.38064852e-23/(1.6e-19)*T ;
A=0.05; % cm2
Aeff=36;
aaT2=A*Aeff*T^2;
V= xlsread(filename,sheet,VRange);

```

```
I= xlsread(filename, sheet, IRange);  
Y=V;  
X=I/aaT2;  
A=[log(abs(X')) ones(length(X'),1) X' ];  
theta=inv(A'*A)*A'*Y';  
n=theta(1)/kTq  
phib=theta(2)/n  
Rs=theta(3)/aaT2/1e3
```

APPENDIX B  
Different design schemes for the device



Different design proposed for reducing the series resistance effect and the capacitance etc. by reducing graphene area and distance between the electrodes.

## REFERENCES

- Berger, C., Song, Z., Li, T., Li, X., Ogbazghi, A.Y., Feng, R., Dai, Z., Marchenkov, A.N., Conrad, E.H., First, P.N., others, 2004. Ultrathin epitaxial graphite: 2D electron gas properties and a route toward graphene-based nanoelectronics. *The Journal of Physical Chemistry B* 108, 19912–19916.
- Bolotin, K.I., Sikes, K.J., Hone, J., Stormer, H.L., Kim, P., 2008. Temperature-dependent transport in suspended graphene. *Physical review letters* 101, 096802.
- Bonaccorso, F., Sun, Z., Hasan, T., Ferrari, A.C., 2010. Graphene photonics and optoelectronics. *Nature photonics* 4, 611–622.
- Cançado, L.G., Jorio, A., Ferreira, E.M., Stavale, F., Achete, C.A., Capaz, R.B., Moutinho, M.V.O., Lombardo, A., Kulmala, T.S., Ferrari, A.C., 2011. Quantifying defects in graphene via Raman spectroscopy at different excitation energies. *Nano letters* 11, 3190–3196.
- Cheung, S.K., Cheung, N.W., 1986. Extraction of Schottky diode parameters from forward current-voltage characteristics. *Applied Physics Letters* 49, 85–87.
- Ciesielski, A., Samorì, P., 2014. Graphene via sonication assisted liquid-phase exfoliation. *Chemical Society Reviews* 43, 381–398.
- Compton, O.C., Nguyen, S.T., 2010. Graphene oxide, highly reduced graphene oxide, and graphene: versatile building blocks for carbon-based materials. *small* 6, 711–723.
- De Heer, W.A., Berger, C., Ruan, M., Sprinkle, M., Li, X., Hu, Y., Zhang, B., Hankinson, J., Conrad, E., 2011. Large area and structured epitaxial graphene produced by confinement controlled sublimation of silicon carbide. *Proceedings of the National Academy of Sciences* 108, 16900–16905.
- Di Bartolomeo, A., 2016. Graphene Schottky diodes: An experimental review of the rectifying graphene/semiconductor heterojunction. *Physics Reports* 606, 1–58.
- Donoval, D., Barus, M., Zdimal, M., 1991. Analysis of I–V measurements on PtSi-Si Schottky structures in a wide temperature range. *Solid-state electronics* 34, 1365–1373.
- Dresselhaus, M.S., Jorio, A., Hofmann, M., Dresselhaus, G., Saito, R., 2010. Perspectives on carbon nanotubes and graphene Raman spectroscopy. *Nano letters* 10, 751–758.

- Ferrari, A.C., Basko, D.M., 2013. Raman spectroscopy as a versatile tool for studying the properties of graphene. *Nature nanotechnology* 8, 235–246.
- Gao, M., Pan, Y., Huang, L., Hu, H., Zhang, L.Z., Guo, H.M., Du, S.X., Gao, H.-J., 2011. Epitaxial growth and structural property of graphene on Pt (111). *Applied Physics Letters* 98, 033101.
- Hass, J., De Heer, W.A., Conrad, E.H., 2008. The growth and morphology of epitaxial multilayer graphene. *Journal of Physics: Condensed Matter* 20, 323202.
- Hernandez, Y., Nicolosi, V., Lotya, M., Blighe, F.M., Sun, Z., De, S., McGovern, I.T., Holland, B., Byrne, M., Gun'Ko, Y.K., others, 2008. High-yield production of graphene by liquid-phase exfoliation of graphite. *Nature nanotechnology* 3, 563–568.
- Hu, B., Ago, H., Ito, Y., Kawahara, K., Tsuji, M., Magome, E., Sumitani, K., Mizuta, N., Ikeda, K., Mizuno, S., 2012. Epitaxial growth of large-area single-layer graphene over Cu (111)/sapphire by atmospheric pressure CVD. *Carbon* 50, 57–65.
- Huang, K.-J., Niu, D.-J., Sun, J.-Y., Han, C.-H., Wu, Z.-W., Li, Y.-L., Xiong, X.-Q., 2011. Novel electrochemical sensor based on functionalized graphene for simultaneous determination of adenine and guanine in DNA. *Colloids and Surfaces B: Biointerfaces* 82, 543–549.
- Hwang, E.H., Sarma, S.D., 2008. Acoustic phonon scattering limited carrier mobility in two-dimensional extrinsic graphene. *Physical Review B* 77, 115449.
- Iyechika, Y., 2010. Application of graphene to high-speed transistors: expectations and challenges. NISTEP Science & Technology Foresight Center.
- Kwak, J.Y., Hwang, J., Calderon, B., Alsalman, H., Munoz, N., Schutter, B., Spencer, M.G., 2014. Electrical characteristics of multilayer MoS<sub>2</sub> FET's with MoS<sub>2</sub>/graphene heterojunction contacts. *Nano letters* 14, 4511–4516.
- Lee, J.-U., Yoon, D., Cheong, H., 2012. Estimation of Young's modulus of graphene by Raman spectroscopy. *Nano letters* 12, 4444–4448.
- Li, X., Cai, W., Colombo, L., Ruoff, R.S., 2009. Evolution of graphene growth on Ni and Cu by carbon isotope labeling. *Nano letters* 9, 4268–4272.
- Malard, L.M., Pimenta, M.A.A., Dresselhaus, G., Dresselhaus, M.S., 2009. Raman spectroscopy in graphene. *Physics Reports* 473, 51–87.
- Martinez, A., Fuse, K., Yamashita, S., 2011. Mechanical exfoliation of graphene for the passive mode-locking of fiber lasers. *Applied Physics Letters* 99, 121107.

- Muñoz, R., Gómez-Aleixandre, C., 2013. Review of CVD synthesis of graphene. *Chemical Vapor Deposition* 19, 297–322.
- Nomani, M.W., Shields, V., Tompa, G., Sbrokekey, N., Spencer, M.G., Webb, R.A., Koley, G., 2012. Correlated conductivity and work function changes in epitaxial graphene. *Applied Physics Letters* 100, 092113.
- Norde, H., 1979. A modified forward I-V plot for Schottky diodes with high series resistance. *Journal of Applied Physics* 50, 5052–5053.
- Novoselov, K.S., Geim, A.K., 2007. The rise of graphene. *Nat. Mater* 6, 183–191.
- Novoselov, K.S., Jiang, D., Schedin, F., Booth, T.J., Khotkevich, V.V., Morozov, S.V., Geim, A.K., 2005. Two-dimensional atomic crystals. *Proceedings of the National Academy of Sciences of the United States of America* 102, 10451–10453.
- Robinson, J.T., Perkins, F.K., Snow, E.S., Wei, Z., Sheehan, P.E., 2008. Reduced graphene oxide molecular sensors. *Nano letters* 8, 3137–3140.
- Rumyantsev, S., Liu, G., Stillman, W., Shur, M., Balandin, A.A., 2010. Electrical and noise characteristics of graphene field-effect transistors: ambient effects, noise sources and physical mechanisms. *Journal of Physics: Condensed Matter* 22, 395302.
- Schedin, F., Geim, A.K., Morozov, S.V., Hill, E.W., Blake, P., Katsnelson, M.I., Novoselov, K.S., 2007. Detection of individual gas molecules adsorbed on graphene. *Nature materials* 6, 652–655.
- Soldano, C., Mahmood, A., Dujardin, E., 2010. Production, properties and potential of graphene. *Carbon* 48, 2127–2150.
- Srivastava, S., Jain, K., Singh, V.N., Singh, S., Vijayan, N., Dilawar, N., Gupta, G., Senguttuvan, T.D., 2012. Faster response of NO<sub>2</sub> sensing in graphene–WO<sub>3</sub> nanocomposites. *Nanotechnology* 23, 205501.
- Suk, J.W., Kitt, A., Magnuson, C.W., Hao, Y., Ahmed, S., An, J., Swan, A.K., Goldberg, B.B., Ruoff, R.S., 2011. Transfer of CVD-grown monolayer graphene onto arbitrary substrates. *ACS nano* 5, 6916–6924.
- Wehling, T.O., Novoselov, K.S., Morozov, S.V., Vdovin, E.E., Katsnelson, M.I., Geim, A.K., Lichtenstein, A.I., 2008. Molecular doping of graphene. *Nano letters* 8, 173–177.



- Wu, Y.Q., Ye, P.D., Capano, M.A., Xuan, Y., Sui, Y., Qi, M., Cooper, J.A., Shen, T., Pandey, D., Prakash, G., others, 2008. Top-gated graphene field-effect-transistors formed by decomposition of SiC. *Applied Physics Letters* 92, 092102.
- Zhu, Y., Murali, S., Cai, W., Li, X., Suk, J.W., Potts, J.R., Ruoff, R.S., 2010. Graphene and graphene oxide: synthesis, properties, and applications. *Advanced materials* 22, 3906–3924.